Maize green area index retrieval from multistatic and multi-frequency SAR data

Jean Bouchat

September 2024

Université catholique de Louvain
Faculté des Bioingénieurs
Earth and Life Institute

Thesis submitted in partial fulfillment of the requirements for the degree of doctor in agronomy and bio-engineering

Thesis committee

Prof. Pierre Defourny, *supervisor*	UCLouvain, Belgium
Prof. Marnik Vanclooster, *chair*	UCLouvain, Belgium
Prof. Xavier Draye, *secretary*	UCLouvain, Belgium
Dr. Dominique Derauw	Liège Space Center, Belgium
Prof. Leila Guerriero	Tor Vergata University of Rome, Italy

Acknowledgments

First and foremost, I would like to express my deepest gratitude to my supervisor, Pierre Defourny, for giving me the opportunity to embark on this great adventure. His trust, positive outlook, and belief in my abilities gave me the confidence I needed to meet the many challenges I faced along the way.

I would also like to sincerely thank the jury for their helpful criticism and their graciousness during our exchanges, and in particular Leila Guerriero, who generously welcomed me into her laboratory during my research stay in Rome. Likewise, I would like to thank Jinlong Fan, Qiaomei Su, and their numerous collaborators for the wonderful welcome I received in China, as well as for the invaluable scientific and cultural exchanges that took place there. I am equally indebted to my project partners, and in particular Emma Tronquo, without whose collaboration I would undoubtedly have been lost along the way. I also wish to acknowledge the great pleasure I took in accompanying Thibaut Castin, Alexis Culot, Basile Boland, and Sébastien Saelens, as they completed their master's theses.

To my colleagues—Pierre H., Quentin, Adé, Maxime, Tom, Baptiste, Jasmine, Sabine, Benjamin, Thomas, Barbara, Thibauld, Boris, Céline L., Audric, Louise, Sacha, Julien, Thibault, Brigitte, Sophie, Thomas, Riana, Lauranne, Colin, Diane, Mathilde, Céline C., Juliette, Céline B., Willy, and all the others—thank you for your kindness and camaraderie. You are the reason I came into the office with a smile on my face every morning.

My heartfelt gratitude to my friends—Benoît, Léa, Sylvain, Ryan, Alexis, Charlotte, Eric, Arnaud, Corentin, Laurine, Nico, Loïc, Mazay, Jérôme, and so many others—who shared with me both the great adventures and the quiet moments of life. You made exploring nature, enjoying a beer at night, or renovating a house equally fun. Clotilde, thank you for walking a beautiful stretch of road with me; I wish you all the best as you continue on your own path. The moments of respite and joy you all provided were essential in helping me maintain balance and perspective.

None of my accomplishments would have been possible without my family, whose unfailing love, help and support have shaped me into the person I am today. You have been my bedrock, giving me the strength to persevere through the most challenging times. The sacrifices you have made and the patience you have shown are beyond words, and I am eternally grateful for everything you have done for me.

Finally, Gaia, thank you for brightening up my days leading to the completion of this manuscript. Your constant reassurance, encouragement, and love have been a source of immense comfort and made this daunting task seem almost effortless. I cannot wait to start a new chapter of my life in Rome with you.

Funding

The research presented in this thesis was conducted in the framework of three projects funded by the European Space Agency (ESA) and the Belgian Science Policy Office (BELSPO):

– the BELSAR-Science project titled "Soil and Crop Monitoring from Simultaneous Mono- and Bistatic Radar Observations" (2019-2022), jointly funded by the STEREO III program of BELSPO and the PRODEX program of ESA;

– the BELSAR-Publication project titled "Beyond BELSAR bistatic dataset exploitation" (2022-2023), funded by the STEREO III program of BELSPO; and

– the Dragon 5 project ID 58944 titled "Retrieving the crop growth information from multiple source satellite data to support sustainable agriculture" (2023-2024), funded by the ESA-MOST China Dragon 5 program.

Although these successive projects limited the undertaken investigations to that which could meet their own objectives, they also enabled close interactions between specialists in the science of synthetic aperture radar (SAR) remote sensing and its application to hydrology and agriculture from several partner institutions, thereby broadening the scope of the research that eventually led to the present manuscript. Accordingly, the results presented in the following pages sometimes go beyond the strict scope of this thesis.

Contents

List of acronyms and notations

AIEM	Advanced Integral Equation Model
AOI	area of interest
BELSPO	Belgian Science Policy Office
BiGRU	bidirectional gated recurrent unit
CCC	canopy chlorophyll content
CR	cross-ratio
DEM	digital elevation model
DHP	digital hemispherical picture
DLR	German Aerospace Center
dpRVI	dual-pol radar vegetation index
ECV	essential climate variable
EO	Earth observation
ESA	European Space Agency
fAPAR	fraction of absorbed photosynthetically active radiation
fCover	fraction of vegetation cover
GAI	green area index
GCOS	Global Climate Observing System
GNSS	global navigation satellite system
GNSS-R	global navigation satellite signal reflectometry
GPSDO	GPS-disciplined oscillator
GRU	gated recurrent unit
IEM	Integral Equation Model
INS	inertial navigation system
IO	iterative optimization
IRF	impulse response function

IW	interferometric wide
JECAM	Joint Experiment for Crop Assessment and Monitoring
LAI	leaf area index
LOOCV	leave-one-out cross-validation
LUT	look-up table
MAE	mean absolute error
MAJA	Maccs-Atcor Joint Algorithm
MLP	multilayer perceptron
NDVI	normalized difference vegetation index
NLP	natural language programming
OOB	out-of-bag
PRF	pulse repetition frequency
PSF	point spread function
RF	Random Forest
RMAE	relative MAE
RMS	root-mean-square
RMSE	RMS error
RNN	recursive neural network
RRMSE	relative RMSE
RT	radiative transfer
S1	Sentinel-1
S1TBX	S1 toolbox
S2	Sentinel-2
SAR	synthetic aperture radar
SLC	single-look complex
SNAP	Sentinel Application Platform
SRTM	Shuttle Radar Topography Mission
SVM	support vector machine
TDR	time domain refectometry
WCM	Water Cloud model

γ	interferometric coherence
R	correlation coefficient
R^2	coefficient of determination
σ_0	normalized scattering coefficient

List of Figures

List of Tables

Chapter 1

Introduction

1.1 Earth observation for agriculture

Agriculture is a vital sector that supports the food and economic needs of a rapidly growing world population that is projected to reach 9.7 billion by 2050 (UN DESA, 2022). Over the past 70 years, in many parts of the world, agriculture has evolved from a largely local activity into a global industry, catering for the increasingly meat-based and globalized diets of 8 billion people, as well as for the production of numerous industrial products, foremost among which are biofuels (OECD and FAO, 2023). This remarkable increase in agricultural production owes its existence to the intensification and expansion of cultivated land worldwide. However, this has led to considerable pressure on the environment and climate—including air (Davidson, 2009), surface and groundwater pollution (Craswell, 2021), soil degradation (Lal, 2015) and deforestation (Peng et al., 2021)—the consequences of which are now threatening the food security and health of populations in vast regions of the world, especially those who are already suffering from unfavorable economic conditions (WEF, 2020).

In this context, agricultural monitoring plays a critical role in observing and assessing the health, growth, and conditions of crops. By gathering rich, wide-ranging data, it seeks to provide near-real-time information on the state of agriculture from the smallest to the largest scale. This information helps to accurately assess the current agricultural production and forecast of future yields, in order to anticipate possible crises when supply is likely to be insufficient. Agricultural monitoring can therefore be a key source of data for balancing supply and demand of food and other agricultural products on a global market under increasing pressure, thus contributing to ensuring food security while identifying and reducing the negative impacts of the sector.

Traditional agricultural monitoring methods, such as manual field checks and surveys, are both time-consuming and expensive. Earth observation (EO) by satellite remote sensing, on the other hand, provides rapid coverage of large areas and delivers comprehensive data on crop condition in a timely and cost-effective manner. In addition, it allows frequent revisiting, enabling precise monitoring of crop and farmland dynamics throughout the year. Time series of these EO data can therefore offer continuous feedback to farmers in the field, and can provide precise prediction of future yields in the short and medium term through their integration into agronomic models. They also enable a better assessment of the damage suffered by crops after drought, snowpack, flooding, and unexpected extreme weather and climate events.

By providing information to the entire value chain, from farmers, traders and retailers to public authorities, satellite remote sensing is emerging as a central and indispensable tool in agricultural monitoring, playing a crucial part in informed decision-making for farm management and policy formulation in the areas of food security, resource management, environmental conservation, and adaptation to climate change. The social, economic, and strategic utility of agricultural monitoring has prompted many private, state, and transnational players around the world to invest massively in EO programs in recent decades (EARSC, 2023). One of the most ambitious of these programs is Copernicus. Funded by the European Commission and implemented by the European Space Agency (ESA), this program provides open access to a wealth of near-real-time remote sensing data worldwide. By facilitating access to high-quality data, it has contributed to the development and improvement of a large number of local and global crop monitoring systems (Fritz et al., 2019), both public and private, which are today at the root of numerous developments in the agricultural sector.

1.2 SAR remote sensing for crop monitoring

Traditionally, most large-scale, cost-effective crop monitoring systems have exploited optical remote sensing data (McNairn and Shang, 2016). Optical remote sensing measures the intensity of the electromagnetic spectrum from the visible to the near infrared and thermal infrared, by collecting solar radiation reflected from the observed surfaces. The interactions between vegetation and the short wavelengths captured by optical sensors are mainly driven by its chlorophyll content and to the internal structure of its leaves (Ustin et al., 2004). Although optical remote sensing offers a quasi-direct and intuitive relationship between sensor data and crop condition, it suffers from a major shortcoming: frequent cloud cover can block the view of sensors, making crop monitoring systems that depend entirely on them unreliable. This poses a major problem on a global scale—since about 70 % of the earth's surface is covered by clouds (King et al., 2013; Stubenrauch et al., 2013)—with important local variations. Indeed, while in many parts of the world cloud cover is sporadic throughout the year, it often coincides with vegetation growth. This problem is particularly acute in tropical regions, where information derived from EO plays an essential role in food security (Becker-Reshef et al., 2020), and where cloud cover can be almost continuous during the crop growing season. As a result, in these regions especially, the timely monitoring of vegetation required for a detailed understanding of crop dynamics cannot be ensured using optical systems alone (Whitcraft et al., 2015).

Synthetic aperture radars (SARs), meanwhile, operate in the microwave part of the electromagnetic spectrum. This enables them to penetrate through clouds, interacting with them only to a limited extent for most frequencies used in land remote sensing applications (Ulaby, 1982). Unlike optical sensors, they are therefore able to acquire data almost independently of cloud cover and adverse weather conditions. In crops, their longer wavelengths interact mainly with plant structure and water content. In some cases, if vegetation is sufficiently sparse, the instrument is also sensitive to the roughness and water content of the underlying soil (El Hajj et al., 2018; Karthikeyan et al., 2017). These sensors are therefore a reliable means of gathering data that can be used directly for crop monitoring, or to improve the spatial and temporal coverage of their optical counterparts. Despite these advantages, and its increased uptake in recent years thanks to advances in technology, techniques, and data access (Liu et al., 2019), SAR remote sensing is not yet used to its full potential for operational crop monitoring, not least because of the inherent challenge posed by the entanglement of the respective contributions of soil and vegetation in the returned signal, as well as the sub-factors influencing both of them (Bhogapurapu et al., 2022; Millard and Richardson, 2018; Balenzano et al., 2010).

1.2.1 SAR response to vegetation

SARs are active sensors, meaning they generate and transmit their own energy in the form of microwave signals, and then measure the returned signal after it has interacted with the target. Signal scattering by the target is mainly driven by its structural characteristics and dielectric properties (Ulaby et al., 1986). For natural targets such as crops, this means that signal scattering will be primarily a function of the water content of the plants and soil, as well as of the geometry of the plants and the roughness of the soil. Indeed, because water is a dipole, its dielectric constant is particularly high. Consequently, when microwave radiation interacts with the plants and soil, the free water molecules in them rotate and align themselves with the applied electric field with relative ease. This movement converts part of the energy transmitted by the microwaves into heat, which is called absorption, and the rest is released by scattering at the frequency of the incident beam in directions that depend on the structure of the target. In addition to these properties of the target, scattering will also depend on the sensor's acquisition parameters, i.e., its frequency band, the angle of incidence of the signal, and its polarization.

The incidence angle is the angle between the radar beam center and the normal to the local topography. However, the look angle, i.e., the angle between the direction towards which the antenna is pointing and the nadir, is often used instead as a simplifying assumption. Together with the wavelength, they are the two determining factors for the ability of the signal to penetrate vegetation and top soil. For the same incidence angle, the longer the wavelength, the deeper the penetration. In addition to affecting the penetration depth of the signal, the wavelength also has a major influence on the effect of the target on the signal, as microwaves are scattered by landscape elements whose size is similar to, or greater than, their transmitted wavelength, while smaller elements contribute to its attenuation. The frequency band in which SAR operates is therefore decisive for the choice of applications or crops for which it is suitable.

In agriculture, the most commonly used frequency bands are the X- (8–12 GHz), C- (4–8 GHz), L- (1–2 GHz) and, to a much lesser extent, S- (2–4 GHz) and P-band (0.3–1 GHz). The main frequency bands used for

Table 1.1: Main radar frequency bands used for crop monitoring.

Band	Frequency	Wavelength	Typical application
X	8–12 GHz	3.75–2.4 cm	High resolution SAR, little penetration into vegetation
C	4–8 GHz	7.5–3.75 cm	SAR all-rounder, moderate penetration into vegetation
S	2–4 GHz	15–7.5 cm	Expends C-band to higher density crops
L	1–2 GHz	30–15 cm	High-biomass crops and soil moisture monitoring
P	0.3–1 GHz	100–30 cm	Forest biomass estimation

crop monitoring are reported with their wavelength in Table 1.1. The energy transmitted by an X-band sensor is mainly returned by the top layer of vegetation. C- and S-bands allow deeper interactions in the vegetation volume without reaching the ground in well-developed crops, making them a good compromise for retrieval of biophysical crop variables. In L-band, most of the signal penetrates the canopy and interacts with both the vegetation and the underlying soil (El Hajj et al., 2018; Balenzano et al., 2010), overcoming the saturation effect impacting higher frequencies (X, C, and S-bands) in high-biomass crops such as maize (Bériaux et al., 2015). This makes it well suited for the monitoring of these crops, or for estimating soil water content under the canopy (McNairn et al., 2009). The very high penetration capacity of the P-band, on the other hand, is more useful for monitoring biomass in forests than for strictly agricultural applications. Since signal penetration in vegetation is correlated with crop biomass and vegetation structure, and as these evolve with crop growth, it is expected that the use of multi-frequency systems would enable better monitoring of their temporal evolution. Currently, however, there are no multi-frequency SAR systems in orbit offering the kind of global and systematic coverage that would be suitable for large scale operational crop monitoring. The forthcoming launch of ROSE-L, delivering freely-accessible L-band data and sharing the same orbit, swath, and acquisition geometry as Sentinel-1 (S1), a C-band SAR constellation, opens up many new perspectives on this topic.

The SAR antenna can be designed to send and receive electromagnetic waves with specific polarizations. These can be linear, either vertical and horizontal, or circular. Most SAR systems have linear polarizations. A single-polarization system transmits and receives a single polarization, usually in the same direction, either horizontal or vertical. These are usually designated as HH and VV—the first letter of these notations correspond to the direction of transmission and the second to the direction of reception, which in turn correspond to the direction of oscillation of the electric field of the electromagnetic wave. A dual-pol system transmits in one polarization and receives in two, usually producing data in HH and HV, or in VH and VV. Finally, a quad-pol system alternately transmits horizontal and vertical waves and receives signals in HH, HV, VH, and VV. Dual-pol and quad-pol SAR systems, because they provide images in different polarizations, reveal important and complementary information on target structural characteristics. Signal scattering by a target can be decomposed into three mechanisms: surface or single-bounce scattering, double-bounce, and volume scattering. Single-bounce scattering, which happens when the SAR signal interacts with a seedbed for example, or simply the soil in not yet developed crops, creates limited signal depolarization. Co-polarized backscatter, in HH and/or VV, will therefore be high, and cross-polarizations, HV and/or VH, will be low. Double-bounce and volume scattering, on the other hand, can depolarize the signal almost completely. The former is often the result of interactions between the signal, and the soil and vertical structures in the canopy such as stems, while the latter can be produced by a thick layer of vegetation whose structures have an almost random orientation. The sensor therefore registers high HV and/or VH signals, and relatively lower HH and VV. The increasing depolarization of the signal during the growing season of a crop is therefore generally a sign of vegetation development.

Finally, SAR systems can be composed of several sensors. The majority of SAR systems in use today are monostatic. This means that transmitter and receiver share the same position. In this case, the signal returned to the sensor is called backscatter. Several sensors can also be combined to provide additional information to that captured by monostatic SAR. Bistatic sensors are receivers located at a non-zero distance from the transmitter. Multistatic sensors, on the other hand, comprise several transmitters and/or receivers. These different configurations make it possible to measure signal scattering in different geometries, thus potentially enriching the information content gathered. Yet, despite this advantage, the potential of multistatic SAR for crop monitoring remains still relatively under-explored to date (Pierdicca et al., 2021).

1.2.2 Biophysical variable retrieval from SAR data

EO-based vegetation descriptors—such as the leaf area index (LAI), the fraction of absorbed photosynthetically active radiation (fAPAR), the fraction of vegetation cover (fCover), and the canopy chlorophyll content (CCC)—play an important role in the monitoring of several key processes, including photosynthesis, respiration, transpiration, rainfall interception, and surface energy balance. These biophysical variables, along with other canopy descriptors such as plant height, water content, and biomass, are crucial for assessing the development, health, and productivity of crops and, more broadly, vegetation.

Among all crop biophysical variables, the significance of LAI, in particular, has been widely recognized for the continuous monitoring and modeling of the Earth's surface (Fang et al., 2019). As such, it has been designated as an essential climate variable (ECV) by the Global Climate Observing System (GCOS) (WMO et al., 2022), and its estimation has been the subject of considerable effort by the land remote sensing community. For the retrieval of this canopy descriptor, methods based on the exploitation of optical data are generally preferred (McNairn and Shang, 2016), e.g., Amin et al. (2018), Delloye et al. (2018), Clevers et al. (2017), and Verrelst et al. (2015).This preference, however, can be potentially detrimental to efficient crop monitoring. Indeed, to properly assess the condition of crops and capture their growth dynamics throughout the growing season, with the ultimate aim of predicting their yield, frequent multi-temporal acquisitions are required. In this context, a recurrent or even continuous presence of clouds seriously undermines the reliability of optical monitoring systems. Because it can acquire data through clouds, SAR is likely to be able to provide the necessary information on crops when optical data are lacking. Despite its obvious advantage in areas of the world where cloud cover is common, however, relatively little effort has been put into retrieving the LAI from SAR data.

The sensitivity of SAR to variations of the LAI of crops during the growing season has been highlighted in numerous studies since the eighties (Ulaby et al., 1986). In one of the few multi-frequency studies, Jiao et al. (2010) analyzed the statistical relationship between LAI and L- (HH, HV), C- (quad-pol), and X-band (HV, VV) SAR backscatter from PALSAR, RADARSAT-2, and TerraSAR-X, respectively, in maize and soybean. They reported high correlations between the LAI in maize and L-band ($R^2 = 0.85$ in HH and $R^2 = 0.92$ in HV) and C-band ($R^2 = 0.80$ in HV) SAR, and only weak relationships for soybean. Meanwhile, X-band SAR was found to be relatively insensitive to both crops. In another multi-frequency study, Fieuzal and Baup (2016) reported coefficients of determination between 0.60 and 0.89 between SAR backscatter and LAI in sunflower, with the best results obtained using C- and L-band data, both in HH, while X-band data performed the poorest due to early signal saturation. However, it is worth noting that only HH was available in X- and L-band, while the C-band was in quad-pol. More recently, Vreugdenhil et al. (2018) assessed the sensitivity of dual-pol backscatter in C-band from S1 to vegetation dynamics in several crops. They demonstrated the suitability of the cross-ratio (CR), defined as VH/VV, for monitoring the dynamics of maize and winter wheat. This index had already been reported to be effective for monitoring maize in C-band, at least until signal saturation due to plant growth (Blaes et al., 2006). Veloso et al. (2017) even found the CR to be as sensitive to maize phenology as normalized difference vegetation index (NDVI), the most widely used optical vegetation index. Several other SAR indices have also been proposed for monitoring vegetation in the broad sense, in an approach similar to the one adopted for the use of NDVI in optical remote sensing. Kim and Van Zyl (2009) proposed the quad-pol radar vegetation index (RVI), defined as $\mathrm{RVI} = 8\mathrm{HV}/(\mathrm{HH} + 2\mathrm{HV} + \mathrm{VV})$, a simplified version of which has also been formulated for dual-pol SAR (Trudel et al., 2012). Nasirzadehdizaji et al. (2019) then adapted it to Sentinel-1, for which only the vertical co- and cross-polarizations (VV and VH) are available over land, resulting in the dual-pol radar vegetation index (dpRVI), $\mathrm{dpRVI} = 4\mathrm{VH}/(\mathrm{VV} + \mathrm{VH})$, which Pipia et al. (2019) found to be highly correlated to LAI over a large number of crops.

Alternative approaches to empirical relationships for the retrieval of LAI from SAR data involve the inversion of semi-empirical models (Liu et al., 2019), the most prominent of which is the Water Cloud model (WCM). Developed by Attema and Ulaby (1978) and then further simplified by Prévot et al. (1993), the WCM can be used to simulate the combined response of vegetation and soil to the SAR signal. Bériaux et al. (2015) used the WCM to retrieve maize LAI from quad-pol C-band SAR data simulated with a physics-based model, the so-called Tor Vergata model (Bracaglia et al., 1995). The best retrieval accuracies between retrieved and measured LAI were obtained by combining separate estimations from the VV and VH polarizations through a Bayesian fusion framework, with an R^2 of 0.67 and an root-mean-square error (RMSE) of 0.85. Hosseini et al. (2021) compared the performance of a modified WCM against a support vector machine (SVM) for the retrieval of the LAI in maize, soybean, and wheat crops with C-band data in VV and VH from RADARSAT-2 and S1. Both WCM and SVM performed well in maize, with coefficients of determination of 0.79 and 0.86 and RMSEs of 0.75 and 0.64, respectively. Similar results were obtained for soybean, while considerably less accurate estimations were found for wheat, with coefficients of determination of 0.43 and 0.75 for the WCM and SVM, respectively. In order to retrieve the LAI while avoiding the need to rely on *a priori* knowledge of soil moisture, Hosseini et al. (2015) used multi-polarized SAR data in C- and L-band for inverting the WCM. The inversion procedure involved calibrating the WCM for a pair of polarizations, then inverting the system comprising the two models by least-squares minimization. They found that the most accurate results were derived from C-band data in HH and HV for both maize and soybean, with coefficients of determination of 0.69 and 0.64, respectively. Extending this work, Mandal et al. (2019) investigated multiple inversion strategies for the retrieval of LAI in maize from dual-pol (VH, VV) C-band SAR data and found that a method based on support vector regression delivered the best results, with an R^2 of 0.86 and an RMSE of 0.68 between retrieved and measured LAI.

Arguably, these approaches, despite being relatively successful at demonstrating the capability of SAR remote sensing for crop monitoring, have not yet enabled it to emerge as a serious alternative to optical remote sensing (Shang et al., 2022). Major gaps, however, remain in the assessment of the potential of SAR for the retrieval of crop biophysical variables. Indeed, investigations into the retrieval of LAI from SAR data have predominantly relied on monostatic SAR data in C-band, which are more readily available for research thanks to the Copernicus program and the Canadian Space Agency's RADARSAT constellations (Parag et al., 2023). While the X-band has also been the subject of numerous studies, in light of the availability of satellite data through TerraSAR-X of the German Aerospace Center (DLR), its use for agricultural monitoring has so far been more limited due to the fact that a comprehensive and systematic coverage is still lacking. As far as L-band SAR is concerned, although in-orbit sensors such as PALSAR-2 and SAOCOM-1 are currently operating, restricted access to dense time series of acquisitions or prohibitive costs have hampered their use in both research and applications (Reisi-Gahrouei et al., 2019; Parag et al., 2023). The same issue has fated the application of multistatic SAR to agriculture to still be largely overlooked, despite the demonstration of its potential for crop biophysical variable retrieval through theoretical investigations, e.g., Guerriero et al. (2013), Pierdicca et al. (2021), and Zhang and Wu (2016). Finally, few efforts have been made towards the joint use of SAR and optical data for LAI retrieval in order to improve the reliability of existing crop monitoring systems in case of frequent cloud cover. In recent years, the dramatic increase in the availability of freely accessible EO imagery has led to the development of data-intensive SAR-optical fusion techniques aimed at improving optical imaging using SAR data. These methods predict missing optical reflectance values by mapping SAR to optical images, typically using deep learning techniques to model the relationship between the two data sources. The reconstructed data can in turn be used to derive the LAI, at the cost of potentially adding several modeling errors. However, to date, apart from the notable efforts of Mastro et al. (2023) and Pipia et al. (2019), there have been relatively few attempts to exploit systematic and dense SAR time series to directly fill past or present gaps in LAI time series derived from optical data, with most studies focusing instead on NDVI (Garioud et al., 2020; Li et al., 2022).

1.2.3 The green area index

The term LAI is ubiquitous in the scientific literature on land remote sensing. However, it is used to refer to different quantities, often without specifying what it actually measures. LAI is generally defined as half the total green leaf area per unit of horizontal ground surface area ($m^2\,m^{-2}$) (WMO et al., 2022). Although this is not apparent from its name, this definition refers only to green leaves. A more fitting name for this quantity would therefore be that of the green leaf area index (GLAI)—naturally giving way to the brown leaf area index (BLAI) of brown or senescent vegetation (Delegido et al., 2015). However, the term LAI remains largely preferred to GLAI by the remote sensing community.

In the context of optical remote sensing, when viewing a canopy from above, all the green organs of the plant (leaves, stems, etc.) influence the measurement in such a way that the contribution of the green leaves cannot be distinguished from the others. It is therefore more appropriate to refer to the biophysical variable that is measured in this way as green area index (GAI), rather than the more commonly used LAI (Duveiller et al., 2011; Weiss et al., 2020b). The GAI can be seen as an extension of the LAI that includes not only the green leaf area (Chen and Black, 1992), but all photosynthetically active elements of the canopy. Although LAI and GAI refer to different physical properties, they are often confused, perhaps, at least in part, because they are often very similar in some crops. For example, Liu et al. (2013) found the two variables to be strongly correlated by destructive measurement in green maize ($\mathrm{LAI} \in [0, 4]$), with $R^2 = 0.99$ and $\mathrm{RMSE} = 0.15$ for a sample of size $N = 35$.

Regarding the use of SAR remote sensing for the retrieval of the GAI, it is just as relevant as for the LAI. The main drivers of microwave scattering in plants are their water content and the orientation of the organs containing it. Since all green organs have a high water content at the cellular level, the SAR signal is bound to be sensitive to variations of the GAI of crops—just as it is to other biophysical variables that have a close relationship to plant water content and geometry—over at least part of the crop cycle, until eventual saturation of the signal by its absorption due to the presence of a large amount of biomass.

1.3 Scope and objectives

The main objective of this thesis is to *improve the retrieval of the GAI in maize crops by means of multistatic and multi-frequency SAR with a perspective towards near real-time, large-scale crop monitoring at the parcel level.*

The GAI is a key biophysical variable for crop monitoring, and knowledge of its variation throughout the growing season is crucial for crop growth modeling and yield estimation. Its monitoring in maize is particularly challenging. Maize is indeed a high-biomass row crop, in which the interactions between microwaves, plant, and soil are particularly complex, making it an excellent case for demonstrating the potential of any method aimed at monitoring GAI in crops.

This primary objective is addressed by attempting to answer three specific research questions.

(i) How sensitive is multistatic SAR in L-band to maize biophysical variables? Numerous studies have already established a link between SAR backscatter and soil and vegetation biogeophysical variables in practically all major crops. From an empirical point of view, however, most of this work has focused on monostatic C-band SAR, and to a lesser extent on X-band SAR (Parag et al., 2023). This discrepancy can be explained in part by the current abundance of data of this type from the TerraSAR-X, RADARSAT (-2 and Constellation), and especially S1 missions. L-band SAR, although potentially valuable given its greater capacity to penetrate vegetation than X- and C-bands (El Hajj et al., 2018), has received less attention in the context of agriculture monitoring than the latter, because, to a certain extent, of the lack of accessibility, or even availability, of dense time series of acquisitions. Other important SAR remote sensing techniques, such as bi- and multistatic SAR, have been largely neglected, beyond a few theoretical studies, due, at least in part, to a lack of empirical data (Pierdicca et al., 2021). To answer the question, we will explore the sensitivity of mono- and bistatic, i.e., multistatic, L-band SAR to a wide range of vegetation and soil biogeophysical variables measured *in situ* in maize crops.

(ii) Is SAR remote sensing alone sufficient to ensure reliable, timely, and accurate GAI monitoring in maize? The GAI is a crucial indicator of crop development and health. Most methods for its large-scale retrieval are based on optical remote sensing data (McNairn and Shang, 2016; Fang et al., 2019). However, these are not often reliable in regions where cloud cover is frequent. In this context, SAR has the advantage of producing data almost independently of the weather. Studies have shown that SAR, together with ancillary data on soil moisture, can be used to retrieve the GAI of crops through the use of semi-empirical ra-

diative transfer (RT)-based models, albeit less successfully than optical methods. The use of SAR data alone has, however, received less attention. Therefore, the aim will be to implement and evaluate a method that only uses SAR data for both GAI and soil moisture retrieval, and to assess the benefit of having information on the latter for retrieving the former.

(iii) How can SAR be combined with optical remote sensing to increase the temporal resolution of crop monitoring systems? Although optical remote sensing is generally considered to be more suitable than SAR for retrieving the GAI of crops, frequent cloud cover leads to sparse time series and unreliable monitoring. On the other hand, the ability of SAR to penetrate clouds enables the acquisition of dense time series in almost any weather conditions. Besides, nowadays, more and more high-quality, open and ready-to-analyze remote sensing data are available. S1 and Sentinel-2 (S2) in particular lead the way with their global coverage and systematic, freely-distributed acquisitions. Making the most of these large quantities of data requires the use of special techniques, such as deep-learning, and, to date, very few studies have made use of them for GAI retrieval. The challenge will thus lie in leveraging the large amount of remote sensing data available today to gap-fill sparse time series of GAI derived from optical images with dense time series of SAR data, in order to improve the observation frequency of crop monitoring systems.

1.4 Outline

The following chapters are organized around papers both published in and in preparation for submission to peer-reviewed journals.

Chapter 2 is devoted to addressing the first research question through empirical evidence by exploring the potential of mono- and bistatic L-band SAR for vegetation and soil monitoring in maize fields. The impact of maize row structure on the SAR signal, as well as its sensitivity to several biophysical variables, including the GAI, is assessed using the BELSAR dataset, an innovative collection of airborne SAR and field data acquired in Belgium.

Chapter 3 introduces several methods for the inversion of a relaxed version of the WCM, a semi-empirical RT-based model, using only C-or L-band SAR backscatter data to simultaneously retrieve the GAI and underlying surface soil moisture in maize crops. To more precisely inform the impact of using only SAR data, the results are then compared with those that can be obtained with ancillary data on one of the two variables, using *in situ* data from the BELSAR dataset. The findings of this chapter provide some answers to the second research question.

Chapter 4 extends the investigation initiated in the previous chapter and addresses third research question set out above. A novel empirical approach is introduced for estimating maize GAI from joint optical and C-band SAR backscatter data in the context of frequent cloud cover. The method relies on the assimilation of a substantial dataset through a deep-learning algorithm specifically designed for GAI retrieval from combined SAR and optical data. As in previous chapters, the BELSAR dataset is used again, more specifically for the external validation of the proposed method.

Finally, conclusions and perspectives for future works are presented in Chapter 5.

Chapter 2

Sensitivity assessment of multistatic SAR in L-band to crop and soil biogeophysical variables

This chapter is adapted from:

Jean Bouchat, Emma Tronquo, Anne Orban, Niko EC Verhoest, and Pierre Defourny (2022b). “Assessing the Potential of Fully Polarimetric Mono-and Bistatic SAR Acquisitions in L-band for Crop and Soil Monitoring”. In: *IEEE Journal of Selected Topics in Applied Earth Observations and Remote Sensing* 15, pp. 3168–3178. DOI: `10.1109/JSTARS.2022.3162911`

and

Jean Bouchat, Emma Tronquo, Anne Orban, Karlus A C de Macedo, Malcolm Davidson, Niko EC Verhoest, and Pierre Defourny (2024). “The BELSAR dataset: Mono-and bistatic full-pol L-band SAR for agriculture and hydrology”. In: *Scientific Data* 11.1, p. 513. DOI: `10.1038/s41597-024-03320-1`

—

Abstract

Theoretical studies have shown that the use of simultaneous mono- and bistatic synthetic aperture radar (SAR) data could be beneficial to agriculture and soil moisture monitoring. This study makes use of extensive ground-truth measurements and synchronous high-resolution fully polarimetric mono- and bistatic airborne SAR data in L-band to assess and compare the sensitivity of mono- and multistatic systems to the maize canopy row structure and

biophysical variables, as well as to soil moisture, and surface roughness in both vegetated and bare fields. The effect of the row structure of maize crops is assessed through the impact of the orientation of the planting rows relative to the sensor beam on microwave scattering measurements. The results of this analysis suggest that the row orientation of maize crops has a significant influence on both mono- and bistatic scattering measurements in both co-polarizations, and especially in HH, while the cross-polarizations are not affected. Furthermore, the study also demonstrates, through regression analysis, the capability of L-band SAR for maize monitoring, as well as suggests that bistatic data, even with a very small bistatic baseline, can provide valuable additional information for maize crop biophysical variable retrieval. The results are not as conclusive, however, with regard to the soil moisture retrieval.

2.1 Introduction

Agriculture and soil moisture monitoring are essential for sustainable food production, water resource management and mitigating the impact of climate change on crop yield and ecosystem health. Today, the best-established large-scale operational agricultural monitoring systems are mainly based on optical remote sensing (McNairn and Shang, 2016). However, they are often hampered by the presence of clouds (Whitcraft et al., 2015), which obscure the view of the sensors. In contrast, synthetic aperture radars are active sensors, largely independent of weather conditions, capable of interacting with and capturing valuable information about both vegetation canopies and underlying soils (El Hajj et al., 2018; Vreugdenhil et al., 2018). The European Space Agency (ESA)'s recent Sentinel-1 (S1) mission, providing systematic and global coverage of dense SAR time series, paved the way for the development of operational applications like the Copernicus Emergency Services and the open-source Sen4CAP system to implement the European Union's Common Agricultural Policy. The success of this operational mission triggered the intent to launch S1 companion satellite to enhance this all-weather earth-observation capacity in a bistatic mode.

Bistatic SARs are radar systems in which the transmitter (Tx) and receiver (Rx) are physically separated, unlike monostatic systems in which they share the same location. Multistatic systems, meanwhile, have several receivers for a common transmitter. The most simple multistatic systems comprise of both an active, monostatic sensor and a passive, bistatic one. These systems allow the acquisition of images using different geometries and configurations, thereby capturing multi-dimensional scattering effects that could not be recorded by monostatic systems alone. These flexible systems offer the advantage of helping to differentiate between the often intertwined relative contributions of vegetation and soil to the received signal, thus improving the retrieval performances of soil moisture and crop biophysical variables retrieval (Guerriero et al., 2013).

Despite its considerable potential, bi- or multistatic SAR applications for vegetation and soil monitoring have remained limited. It seems that this scarcity can mostly be attributed to a lack of comprehensive, well-documented experimental datasets combining mono- and bistatic SAR acquisitions and *in situ* measurements of vegetation and soil biogeophysical variables (Pierdicca et al., 2021). As a result, the potential of bistatic SAR for these applications has mainly been investigated via radiative transfer (RT) models, e.g., Pierdicca et al. (2021), Zhang and Wu (2016), Zeng et al. (2016), Guerriero et al. (2013), and Della Vecchia (2006).

Multiple theoretical investigations into the scattering behavior of microwaves in agricultural areas have demonstrated that certain bistatic sensor configurations could limit the contribution of the underlying soil to the recorded scattering, thus making it possible to better distinguish the signature of the vegetation in the scattered signal and improve the retrieval accuracy of vegetation biophysical variables (Della Vecchia et al., 2006b; Guerriero et al., 2013; Pierdicca et al., 2021). These RT model-based studies, aimed at identifying the optimal bistatic configuration for biophysical variables retrieval from L-band SAR data, have demonstrated that the passive sensor should ideally be in the plane that lies in azimuth angle orthogonal to the plane of incidence (Guerriero et al., 2013; Zhang and Wu, 2016) and with very large bistatic baselines (Pierdicca et al., 2021).

Regarding soil moisture retrieval, studies by Schmugge (1976) and Ulaby (1982) illustrated that in agricultural areas the scattered mi-

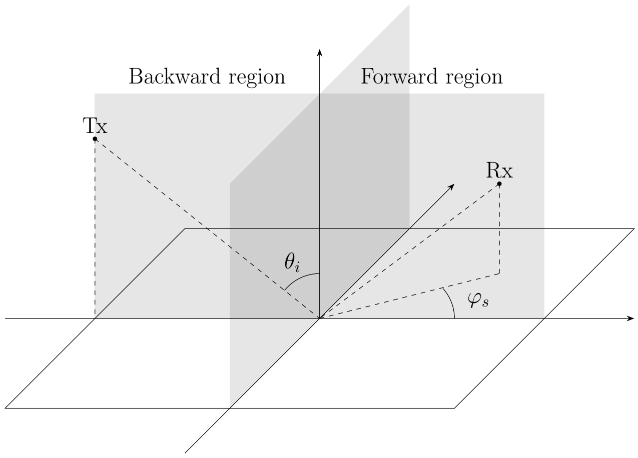

Figure 2.1: Geometry of bistatic scattering with a transmitter, Tx, a receiver, Rx, the incidence angle, θ_i, and the azimuth scattering angle, φ_s.

crowave signal is partially influenced by the dielectric properties of the soil, and thus the soil moisture content. Furthermore, since the radar signal is also highly sensitive to the geometric arrangements of scatterers on the ground surface, the radar measurements are not only sensitive to soil moisture, but also to soil surface roughness, which is commonly affected by tillage operations in agricultural fields (Rakotoarivony et al., 1996; Verhoest et al., 2008). As a result, it is difficult to differentiate between the contributions of soil moisture and surface roughness on radar backscatter when relying on measurements from monostatic SAR systems alone. This makes the retrieval of soil moisture with such systems challenging. Recent studies investigated the potential of combining radar and optical images, from S1 and Sentinel-2 (S2) respectively, for predicting soil moisture and crop biophysical variables (Allies et al., 2021; Efremova et al., 2022; Liu et al., 2020). The results of these studies show that combining the microwave and optical domains is a promising technique for finer crop and soil monitoring thanks to its increased temporal sampling and retrieval accuracy. Furthermore, the interest in bi- and multistatic SAR remote sensing has grown over recent years, whereby several studies reported an expected mitigation of the adverse impact of surface roughness on the retrieval of soil moisture with the simultaneous use of mono- and bistatic SAR scattering data, i.e., multistatic (Ferrazzoli et al., 2003; Pierdicca et al., 2008; Pierdicca et al., 2009; Brogioni et al., 2010; Johnson and Ouellette, 2013; Zeng and Chen, 2018). Global navigation satellite signal reflectometry (GNSS-R) is a bistatic remote sensing technique that has been studied intensively over recent years, by means of both theoretical modeling and experimental results (Egido et al., 2012; Zribi et al., 2018). One of the main drawbacks of these GNSS-R studies is the fact they are focused on bistatic scattering in the specular region. In order to evaluate various SAR geometries for soil moisture detection, only studies relying on theoretical model simulations are available to-date, e.g., Pierdicca et al. (2008) and Brogioni et al. (2010). In these studies it is hypothesized that the impact of surface roughness can be mitigated with the use of two simultaneous observations of the scene. The results of these works point to an improvement in soil moisture retrieval accuracy, especially for bistatic measurements performed in the forward region—a region, depicted in Figure 2.1, defined by azimuth scattering angles, φ_s, comprised between $-\frac{\pi}{2}$ and $\frac{\pi}{2}$—(Zeng et al., 2016; Pierdicca et al., 2008; Pierdicca et al., 2021).

In this context, where studies on the sensitivity of multistatic SAR are predominantly theoretical and the technique is still largely under-exploited, this study aims to fill a research gap by assessing its potential for agricultural and soil moisture monitoring applications using an empirical dataset, the so-called BELSAR dataset. This set comprises multi-temporal high-resolution fully polarimetric L-band SAR data acquired simultaneously in mono- and bistatic mode, as well as extensive *in situ* vegetation and soil measurements, the details of which are presented first. Then, the sensitivity of these SAR data to maize crop biophysical variables and canopy row structure, as well as to soil moisture and surface roughness in vegetated and bare agricultural fields, is assessed using linear regression analysis and a machine learning model. Finally, recommendations are formulated for future satellite SAR missions based on the gathered insights.

2.2 Data from BELSAR-Campaign

The BELSAR dataset is a unique collection of high-resolution airborne mono- and bistatic fully-polarimetric SAR data in L-band, alongside concurrent measurements of vegetation and soil biogeophysical variables measured in maize and winter wheat fields during the 2018 growing season in Belgium. The collection of this innovative dataset was funded by ESA to address the lack of publicly-accessible experimental datasets combining multistatic SAR and *in situ* measurements. A detailed description of the dataset, including the methods used to collect the data, can be found in Bouchat et al. (2024).

2.2.1 Site description

The BELSAR airborne and field campaign took place between May and September, 2018, in the BELAIR Hesbania test site, between Gembloux and Sint-Truiden, in the Hesbaye region of Belgium. This site belongs to the global Joint Experiment for Crop Assessment and Monitoring (JECAM) network. The location of the site and the fields in which *in situ* measurements were recorded is shown in Figure 2.2. The area corresponds to a typical landscape of intensive agriculture in Belgium. The fields are relatively large, flat, and homogeneous, with a uniform topsoil texture of silt loam. The major crops in the area are wheat, potatoes, beets, and maize.

2.2.2 Airborne SAR data

The radar data for this study was collected during a series of five flight missions with two airplanes carrying a multistatic SAR system. The flights took place approximately one month apart, between May 31 and September 10, 2018.

Mono- and bistatic airborne radar data were acquired simultaneously by two left-looking L-band SAR designed and operated by MetaSensing BV on-board two CESNA Gran Caravan specifically adapted for the mission. The radar systems and planes are shown on Figure 2.3.

MetaSensing BV's airborne L-band SAR system (Macedo et al., 2019) is a versatile compact sensor providing imaging with spatial resolution up to 1 m, equipped with two flat antennas: a squared one and a rectangular one, with a nominal antenna look-angle of 45°, and a beamwidth of 40° in elevation and respectively 40° and 20° in azimuth. The sensors were synchronized through special techniques based on a dedicated high-accuracy GPS-disciplined oscillator (GPSDO) system. Addition-

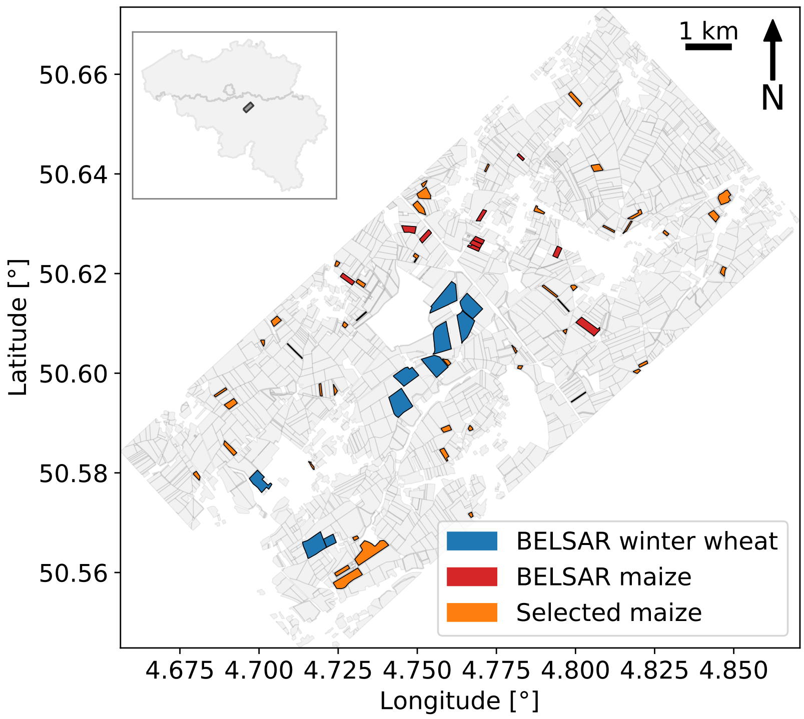

Figure 2.2: BELSAR area of interest, with the reference winter wheat and maize fields in which the *in situ* measurements were acquired in blue and red respectively, other maize fields in the area in orange, and all the other agricultural fields inventoried as delineated in the anonymized land parcel identification system of Wallonia, Belgium, in grey.

ally, high-end global navigation satellite system (GNSS)/inertial navigation system (INS) devices were installed on them to be able to track their navigation and attitude precisely. Each sensor is capable of transmitting and receiving in fully-polarimetric (HH, HV, VH, and VV) ping-pong mode on a chirp-to-chirp basis, allowing both sensors to simultaneously collect mono- and bistatic SAR images.

The radar operates in frequency modulated continuous wave mode (FMCW) at the central frequency of 1.3 GHz, with an operating frequency range of 1.2 to 1.4 GHz. However, this large available radar

Figure 2.3: (**left**) MetaSensing BV's airborne L-band SAR system on-board one of the two CESNA Gran Caravan airplanes and (**right**) a picture of one airplane taken from the other while flying in the across-track (XT) configuration.

Table 2.1: Dates (format: day-month-2018) of airborne SAR acquisitions and *in situ* measurements (ISM) of vegetation and soil variables, with the corresponding development stages of maize.

ID	Flight date	ISM date	Maize stage
F1	30/05	30-31/05 & 05/06	Leaf development
F2	20/06	21-22/06 & 26/06	Stem elongation
F3	30/07	01/08 & 02/08	Dough stage
F4	28/08	29/08 & 30/08	Fully ripe (M2, M5) & bare soil with stalks
F5	10/09	10/09 & 11/09	Bare soil with stalks

bandwidth could not be exploited due to the authorization from the Belgian Institute for Post and Telecommunications being restricted to a bandwidth of 50 MHz centered on 1.375 GHz. The pulse repetition frequency (PRF) was 1004 Hz and the sampling frequency was 50 MHz.

On each of the five flight missions, named F1 to F5, three parallel passes were necessary to cover the 4.5 km wide area depicted in Figure 2.2. The flights were conducted along three overlapping tracks Zulu (Z), Alpha (A), and Bravo (B) in alternating opposite directions. A forth short data sample, Zulu Short (Z_{short}), was also acquired over a selected subset of the area of interest (AOI) incorporating the most numerous

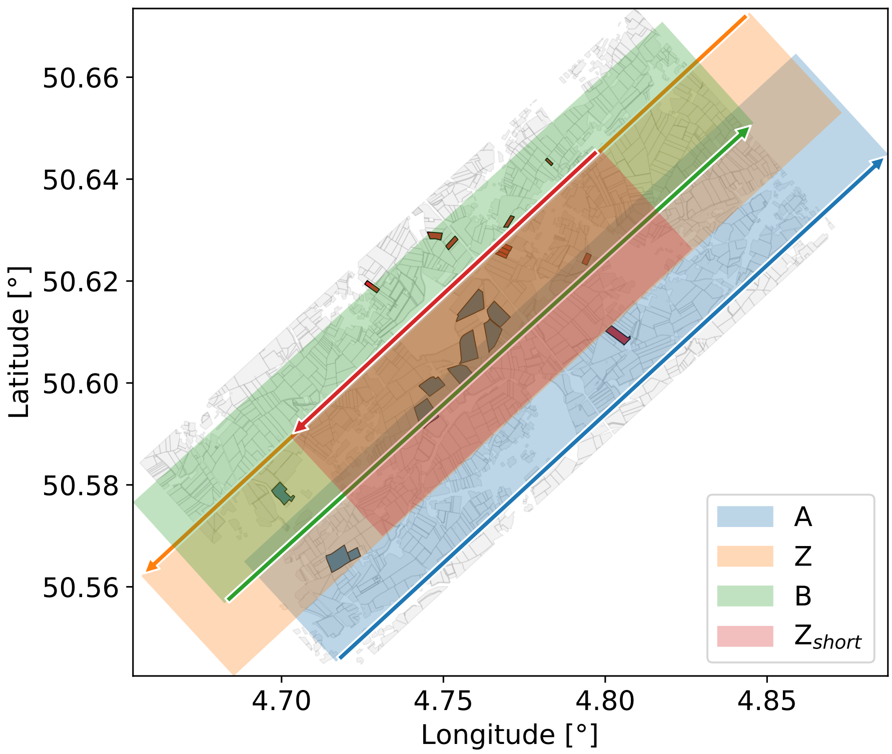

Figure 2.4: Track design in alternating opposite directions to cover the BELSAR area of interest, and the subset area Z_{short}. The arrows indicate the trajectory of the left-looking sensors for each track.

and representative fields (both maize and winter wheat), to perform a quick preliminary quality analysis of the data. Tracks A and B were flown from southwest to northeast, while Z and Z_{short} were covered from northeast to southwest. It should be noted that the length of each track slightly varied from one flight to the other. Variations in size of the tracks from one flight to the next as well as their overlap resulted in some fields being imaged only on certain dates and others being imaged several times on the same day with different acquisition geometries. The latter were considered as different fields, and thus separate data points in this study.

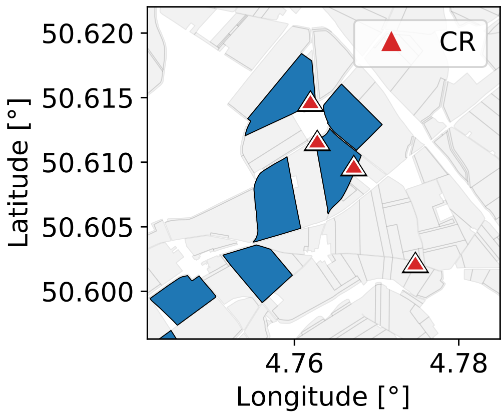

Figure 2.5: (**left**) Corner reflectors localization within the subset area Z_{short} and (**right**) a corner reflector in the field.

Four triangular pyramidal corner reflectors were deployed in the subset area, Z_{short}, and used for monostatic acquisitions to produce a geometrical reference as well as the point spread function (PSF), which provided the achieved resolutions and an indication about the quality of the synchronization between the transmitter and the receiver. They were located in a row in the across-track direction, spaced across one strip image, from near range to far range, remaining in the central part of it. Positions and azimuth orientation were determined for acquisition along the central track, Z. The elevation angle was adapted depending on the authorized altitude for each flight. The position of the corner reflectors was measured with a precision of 1 m using a GNSS receiver. They were deployed and correctly aligned in azimuth and elevation for each flight. The complete set of tables describing the tracks and corner reflector installation can be found in the final report of the BELSAR-Campaign project (*Technical Assistance for the Deployment of a L-Band SAR system to perform bistatic and interferometric SAR measurements during the ESA BelSAR Campaign*, 2020).

On each flight mission, and for each track, mono- and bistatic data were acquired in two different bistatic geometries by flying the two airplanes carrying the multistatic system in tandem once in across-track (XT) and once in along-track (AT) flight configuration. These acquisition configurations were established on the basis of ESA's requirement to reproduce the configuration planned for the SAOCOM-CS satellite mission (Gebert et al., 2014). Recommended values for both along-track and across-track baselines, which are illustrated in Figure 2.6, were established with the objective of keeping a convenient interferometric coherence range for interferometric applications. The small authorized frequency bandwidth and the quite low flight altitude drastically limited the critical baseline regarding geometric decorrelation and expected interferometric coherence (Orban et al., 2021). Recommended XT baseline was then as short as 30 m at slightly different altitudes of about 5 m and with the master plane slightly behind the slave plane (∼5 m). In the case of the AT configuration, the along-track baseline constraint was dictated by the need for azimuthal spectra superposition, which imposed an along-track baseline of about a quarter of the flight altitude: 3 dB half width at mid antenna pattern is a little smaller than the flight altitude and decreases with decreasing range. Consequently, if considering an along-track baseline of a fourth of the azimuthal footprint width at mid antenna pattern, common intersection of azimuth spectra will be half the azimuth bandwidth only at high range. This intersection decreases at lower ranges leading to larger azimuthal resolution losses. Additionally, it also means that azimuthal filtering must be strongly range dependent to keep a good coherence. To avoid important azimuth resolution losses, but also to ease azimuth filtering while keeping a larger ground range swath available, it was suggested to limit the across-track baseline to one eighth of the 3 dB azimuth footprint width at mid antenna pattern, or around a quarter of the flying altitude.

The actual AT and XT baselines respectively were 450 m and about 35 m for all flight missions except for the first one (F1) in AT configuration where an along-track baseline of about 900 m and a horizontal separation of about 60 to 80 m were observed (*BelSAR Data Acquisition Report*, 2019). This was much larger than expected. Ideally, there would have been no across-track separation and around 10 m in altitude separation. The actual baselines are shown on Figure 2.7 for the first two flight missions, F1 and F2. These limited baselines, coupled with the fact that both SAR sensors were left-looking, strongly limited the scope of this study to measurements in the backward region—i.e., the region in Figure 2.1 which has azimuth scattering angles, φ_s, comprised in $[\frac{\pi}{2}, \frac{3\pi}{2}]$—

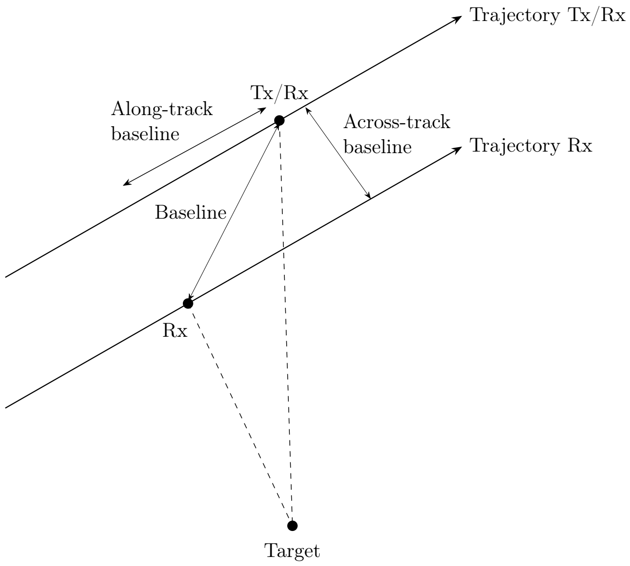

Figure 2.6: Sketch of BELSAR's bistatic geometry representing transmitter-receiver, Tx/Rx, the bistatic receiver, Rx, and the along- and across-track baselines that characterize the AT and XT flight configurations.

with very small bistatic angles, i.e., the angle subtended between the transmitter, target, and receiver. Rather than bistatic, the resulting XT configuration could even rather be labeled as quasi-monostatic.

Radar data were processed by MetaSensing BV using the time-domain back-projection algorithm, which also handles motion compensation. They were delivered as σ-calibrated single-look complex (SLC) focused SAR data in ground range geometry, with a ground resolution of 1 m in azimuth and 4 m in slant range, after Hann windowing with a 50 MHz transmitted pulse. The SAR images were geo-referenced and co-registered on a sub-pixel level based on the absolute position accuracy of the navigation data, i.e., 0.75 m. The implemented SAR processing chain is shown in Figure 2.9.

Geometric calibration was performed using the corner reflectors. For bistatic data, two range delays had to be defined, one for each system. One of the range delays was adjusted relatively to the absolute calibrated

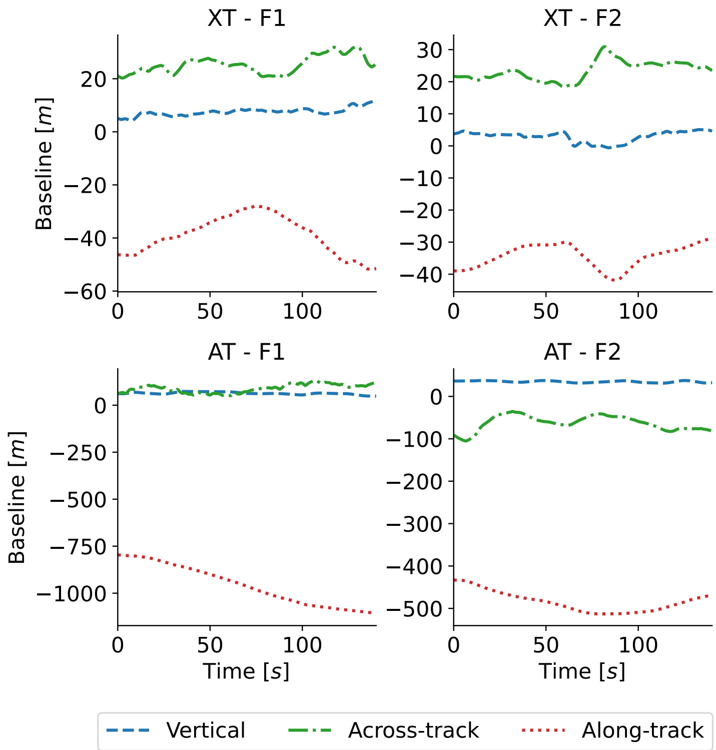

Figure 2.7: Actual vertical, across-track, and along-track baselines between the sensors over Z_{short} for the (**left**) first (F1) and (**right**) second (F2) flight missions in the (**top**) XT and (**bottom**) AT flight configurations.

one according to a global offset obtained from a coherence-based fine subpixel co-registration.

Radiometric calibration, providing the σ_0, was carried out on the basis of the corner reflector's response. The absolute calibration factor, K, was evaluated for each flight mission. The same procedure was applied to both mono- and bistatic data. Antenna pointing direction and incidence angles were computed using post-processed navigation data and an external digital elevation model (DEM). For XT acquisitions, it was considered that the corner reflectors viewed by the bistatic acquisitions behaved similarly to the monostatic case. For bistatic data in the AT

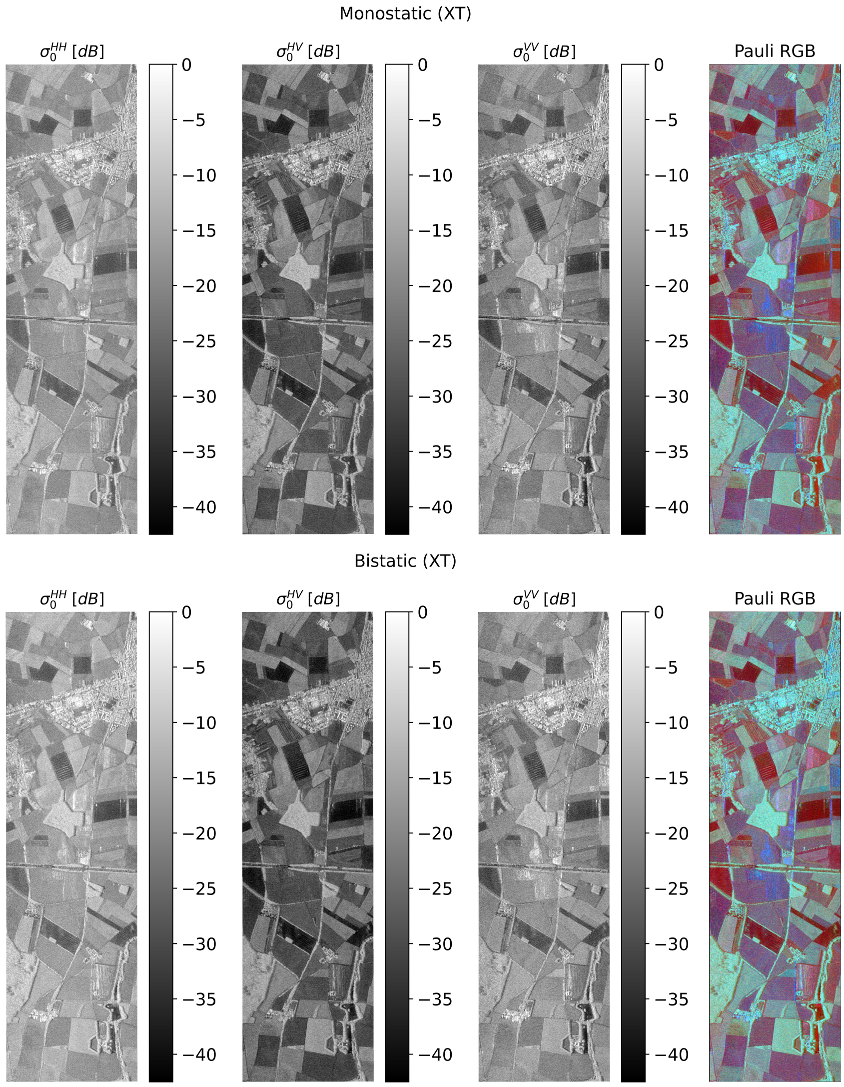

Figure 2.8: (**top**) Monostatic and (**bottom**) bistatic scattering coefficients σ_0 in HH, HV, and VV polarizations, as well as their Pauli RGB color composite (R: HH-VV ; G: HV+VH ; B: HH+VV), acquired on June 20 (F2) over a subset of the area covered by tracks Z and Z_{short} in the across-track (XT) bistatic configuration.

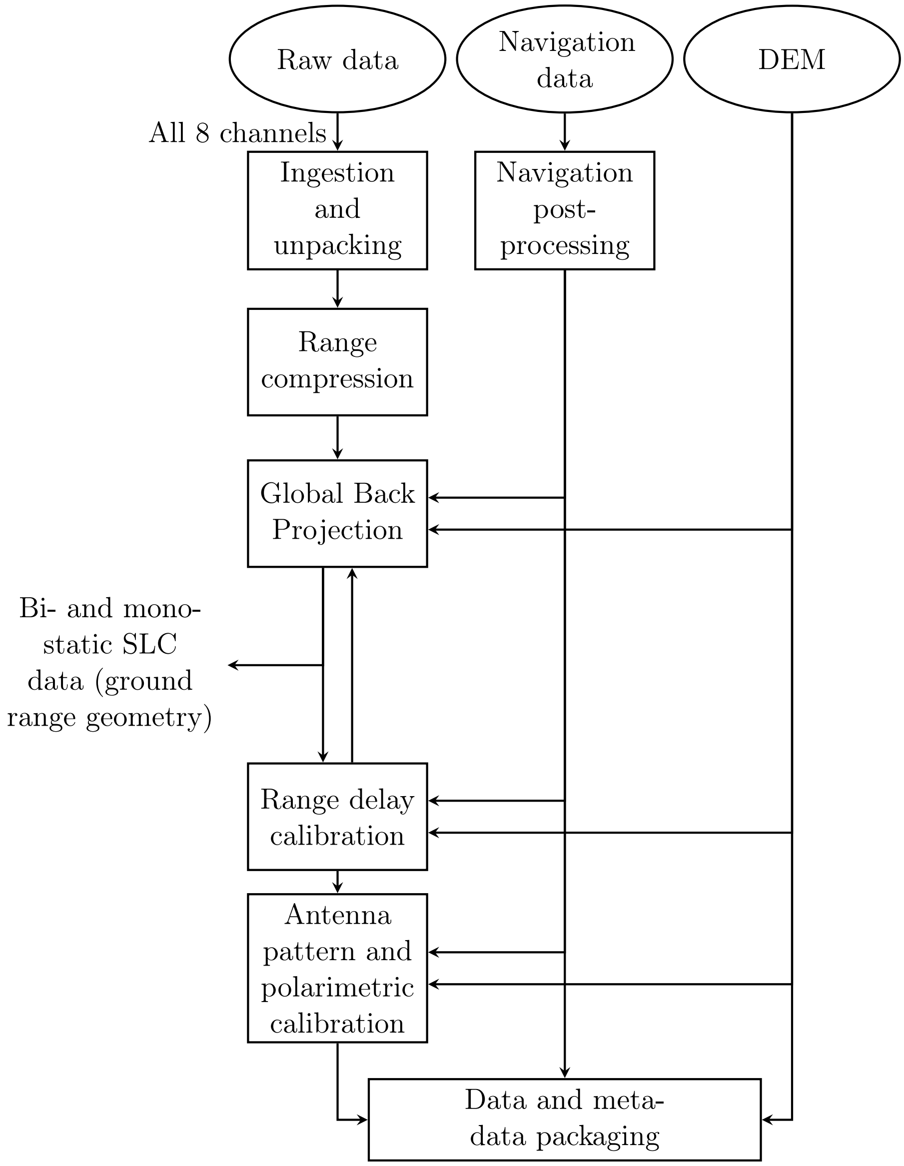

Figure 2.9: BELSAR L-band SAR processing chain.

configuration, the corner reflectors are not present. The radiometric offset for the bistatic AT data is thus based on the monostatic AT and bistatic XT data. This might result in an imbalance between bistatic and monostatic, or from flight to flight, in the AT data.

A polarimetric calibration was also applied, following the procedure described in Fore et al. (2015), in order to insure the images acquired in the different polarization channels correctly reflected the dependence of the target response to the polarization state of the signal. Data were calibrated for co-pol and cross-pol channel imbalances, that is amplitude and relative phase differences between polarization channels, at both transmission and reception. Based on the obtained polarimetric signatures and corner reflector's impulse response function (IRF) showing sufficiently good isolation between the polarization at antenna level, cross-talk was considered negligible.

Finally, data were delivered in 320 (= 2 sensors × 5 flights missions × 4 tracks × 2 bistatic configurations × 4 polarizations) NetCDF files composed of a series of arrays including the antenna pattern, navigation data, DEM used, geographical position of the focused pixels in geographical coordinates (WGS84) (*MetaSAR-L NetCDF File Format Description*, 2019).

In the context of this study, the acquisitions in the AT configuration suffer from two main problems. First, the spatial baseline between the sensors changed between the first flight mission, F1 (900 m), and the subsequent flight missions, F2 to F5 (450 m). This had for consequence to make incomparable between them the images which resulted from the first and subsequent flights, and hence to decrease significantly the quantity of data available for the analysis performed in this study. Then, and especially, the calibration of the bistatic images in AT had to be performed without the corner reflectors, which were not visible in the corresponding images, based on the monostatic acquisitions and those in XT. This may have resulted in imbalances. Images acquired in the XT configuration were not affected by those problems, hence only those are considered in this study and in Chapter 3. A sample of these images can be seen on Figure 2.8.

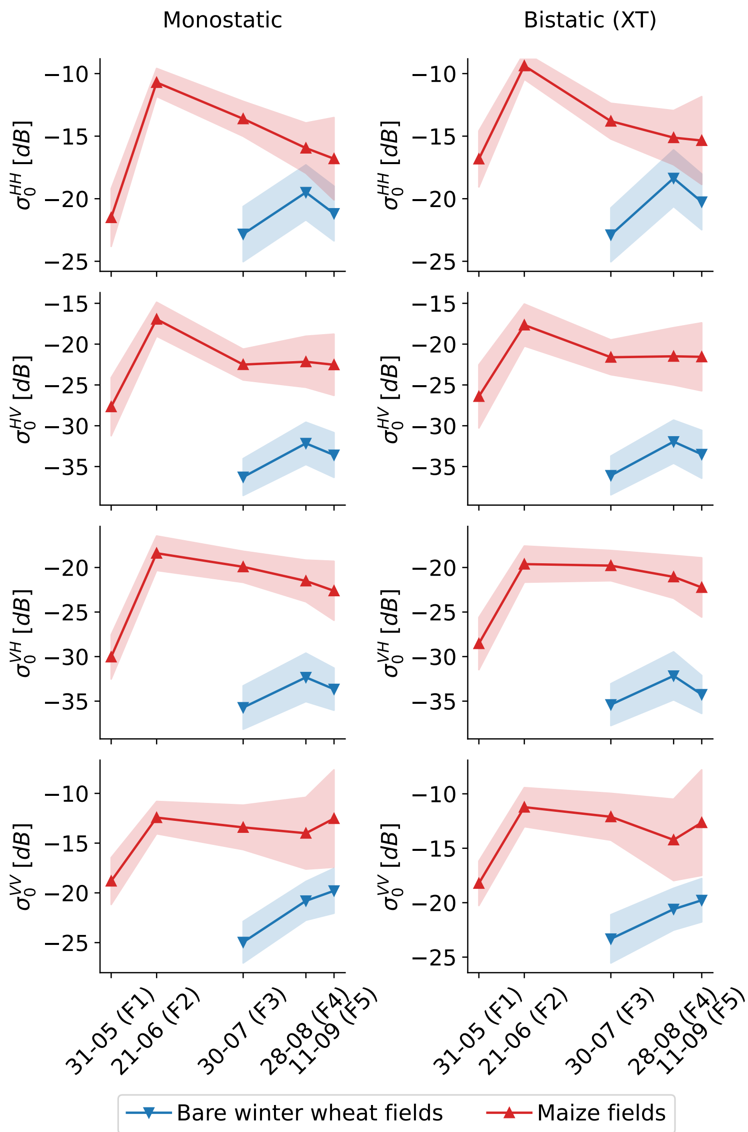

Figure 2.10: Time series of the average (**left**) monostatic and (**right**) bistatic scattering coefficients σ_0 in (**top to bottom**) HH, HV, VH, and VV polarizations, recorded in the BELSAR reference fields. The translucent areas represent two standard deviations around the mean.

2.2.3 *In situ* data

The summer of 2018 was marked by an exceptional drought that impacted the campaign. Crops reached maturity early in the season and were consequently harvested several weeks earlier than usual. This limited the time window during which the crops could be observed and also resulted in unusually dry soil conditions.

Along with each flight mission, measurements of vegetation and soil biogeophysical variables were recorded in 8 maize and 10 winter wheat fields inside the imaged area. A total of 10 maize fields were actually visited, but two of them were never imaged by the L-band SAR system and the *in situ* measurements recorded there were therefore excluded from the dataset in this study. These fields are subsequently referred to as BELSAR reference fields and are reported in Figure 2.2. At the time of the first acquisition, winter wheat and maize crops were already in place. Harvesting took place between the second (F2) and third (F3) acquisitions for winter wheat, and between the third (F3) and last (F5) for maize. Some SAR acquisitions were therefore conducted over bare fields, with stalks still present on the maize fields after harvest.

The time series of the vegetation and soil biogeophysical variables collected *in situ* in these fields are represented in Figure 2.11. In addition, the time series of their average mono- and bistatic scattering coefficients, acquired in the XT flight configuration, are depicted in Figure 2.10. Finally, a summary of the airborne acquisitions dates and the corresponding *in situ* measurements dates can be found in Table 2.1–the *in situ* measurements were performed with a delay of maximum six days with respect to the airborne SAR missions.

Maize crop variables

Sowing density, green area index (GAI), plant height, wet biomass and vegetation water content were, among others, measured to characterize the vegetation canopy. These measurements were performed in accordance with the guidelines laid down by JECAM (Hosseini et al., 2018).

Maize crop biophysical variables were measured, up to the harvest–which occurred at different dates in the sampled fields, i.e., between end of July (F3) and September (F5)–in three representative plots well inside the boundaries of each of the eight reference fields, and then averaged

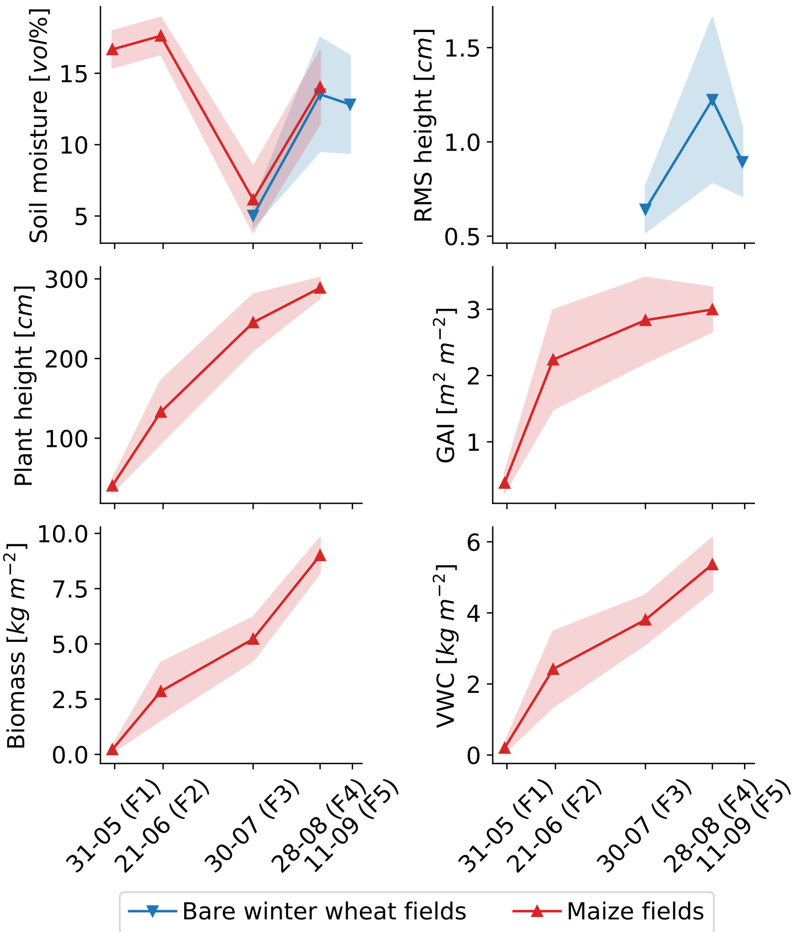

Figure 2.11: Time series of the vegetation and soil biogeophysical variables measured *in situ* in vegetated maize and recently harvested winter wheat fields. The translucent areas represent two standard deviations around the mean.

at the field level. These plots were selected for their representativity according to their normalized difference vegetation index (NDVI) profile, which had been computed from Pleiades images days prior to the start of the campaign.

For each of the three plots in each reference field, GAI measurements

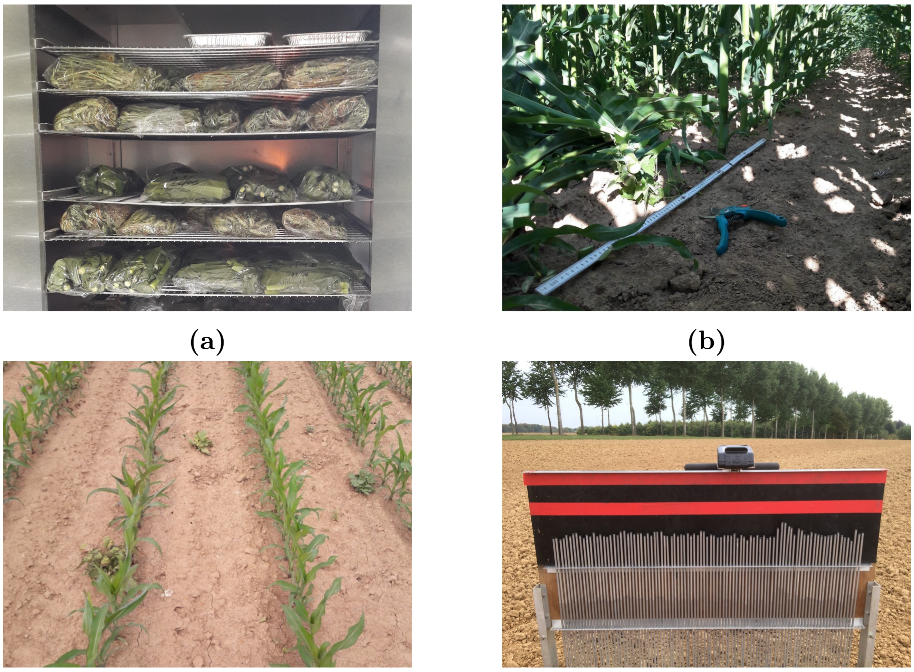

(a) **(b)** **(c)** **(d)**

Figure 2.12: (**a**) Oven drying of the plant subsamples, (**b**) crop cutting along a 1 m row, (**c**) maize planting rows, and (**d**) pin profilometer.

were derived using the CAN-EYE software (Weiss and Baret, 2017) from 10 digital hemispherical pictures (DHPs), one every 3.75 m, with an approximate nadir view 1 m above the crop canopy.

In addition, the height of the plants was measured with a ruler from the ground level to its highest part, i.e., leaf, flower, ear or panicle depending on the crop and the stage of development, without extending it manually. For each run, nine plants were measured in each plot to derive a field average.

Plant density was measured once at the beginning of the growing season by measuring both interline and interplant distances. Row spacing was measured directly between two rows three times per plot across different rows. The interplant distance was derived by counting the number of plants in a one-meter length of sowing row three times per plot.

Finally, the vegetation biomass was determined by destructive sampling and oven drying. In each plot, all the plants along three sowing lines of 1 m were cut and weighted on the field to determine their total fresh weight and, together with plant density, the above-ground plant biomass ($\mathrm{kg\,m^{-2}}$). The three harvested rows were randomly selected diagonally from each other. A subsample of the cut plants was then randomly selected, weighed and stored in a micro-perforated plastic bag which was then oven-dried at 60 °C for 72 h. The dry weight of the subsample was then measured to obtain the dry matter content of the plants, from which vegetation water content was derived. There were no weeds in the plots. Pictures of the subsamples in the oven and of the crop cutting are shown in Figure 2.12.

Below-canopy and bare soil variables

Soil moisture and surface roughness measurements were conducted in the harvested, and therefore bare, reference winter wheat fields, and only the former were recorded in the vegetated maize fields[1].

Volumetric soil moisture measurements were conducted using time domain reflectometry (TDR) sensors with 11 cm rods. At least 10 locations per reference field were monitored with three repetitions per location. All soil moisture measurements within each field were averaged to provide field average soil moisture values. The range of soil moisture values is 3.03 to 18.9 vol%, which depicts very dry conditions, especially in July (F3).

Soil surface roughness was determined using a pin profilometer, shown in Figure 2.12, of 1 m length, with a spacing of 1 cm. Roughness profiles were measured in two directions, i.e., along and across the direction of tillage. Pictures of the pin profilometer in both directions were taken and then digitized to correct for tilted pictures and to allow determination of root-mean-square (RMS) heights, which was calculated according to the procedure described in Davidson et al. (2003). At least five profiles per reference field were taken in both orientations on each acquisition date. Maize fields could not be monitored while the crop was still in place. By means of linear regression analysis, it was found that the mean of

[1] In this chapter, measurements recorded less than 20 m from the field boundary were taking into account, contrary to Bouchat et al. (2022b) in which they were excluded, which explains the slight discrepancies observed in the corresponding results.

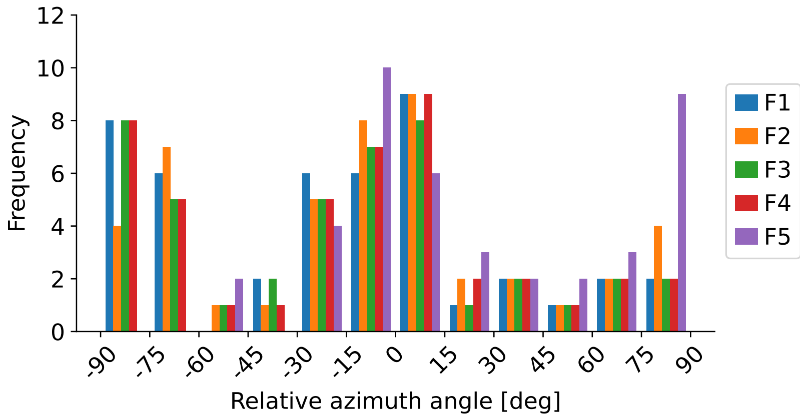

Figure 2.13: The distribution of all considered maize fields in the BELSAR AOI in relation to their relative azimuth angle, i.e., the angle between the SAR incidence plane and the planting rows, for each flight (F1 to F5). An angle of 0° means that the rows of maize are completely parallel to the SAR signal beam. Fields acquired on different, overlapping flight tracks (on both A and Z, or on B and Z) are counted twice.

RMS heights across and along the direction of tillage is best correlated to both mono- and bistatic scattering coefficients and is therefore used in this study.

2.2.4 Row orientation data

The relative azimuth angle, i.e., the angle between the plane of incidence of the SAR beam and the orientation of the planting rows, of 37 maize fields in the BELSAR AOI has been derived from high-resolution orthophotos. The fields were selected based on their size and shape, so that their rows were straight and all oriented in the same direction. All but one of the BELSAR reference maize fields are part of this set.

The BELSAR AOI, the 10 winter wheat and 8 maize fields for which *in situ* data are available, and these 37 maize fields, are all depicted in Figure 2.2.

2.3 Methods

The assessment of the sensitivity of the L-band mono- and bistatic SAR data to vegetation and soil biogeophysical variables is the subject of a separate methodology from the one used to assess their sensitivity to the vegetation row structure.

For the former, a regression analysis is performed to evaluate the sensitivity of the SAR measurements to the vegetation biophysical variables in maize crops, as well as to the surface soil moisture and roughness under the canopy in maize fields and in harvested (and therefore bare) winter wheat fields. The aim is to compare the potential of simultaneous mono- and bistatic SAR data, which are designated as multistatic in this study, with traditional monostatic data for vegetation and soil monitoring applications.

For the latter, the canopy row structure effect is analyzed through the relationship between the orientation of the maize rows relative to the SAR beam and the scattering measurements in almost all the imaged maize fields and at various phenological stages.

2.3.1 Vegetation row structure effect

Maize is traditionally planted in rows, so that the space between them is much greater than that between plants, as shown in Figure 2.12. A maize field therefore has a different aspect depending on whether it is viewed in the direction of its rows or perpendicular to them, notably because the view of the ground is more obstructed by the presence of plants in the latter case than in the former. This makes it an anisotropic target.

In order to assess the effect of the orientation of the rows of maize on the mono- and bistatic scattering measurements, a total of 37 sufficiently regular and large maize fields in the BELSAR AOI are sorted into two groups according to the orientation of their rows relative to the SAR signal beam. The first group comprises all fields which have a relative azimuth angle up to 30° departed from the plane of incidence of the signal beam. The second is made up of the fields which have a relative azimuth scattering angles between $-90°$ and $-60°$ or between $60°$ and $90°$, i.e., (almost) perpendicular to the signal beam. Other fields in the AOI which belong to neither of the two aforementioned groups are discarded. As sensor trajectories differ slightly from flight to flight, the angle is calculated for each acquisition. In addition, acquisitions of fields present on two different tracks (A and Z or B and Z) are considered as distinct. The distribution of fields in relation to their relative azimuth angle is shown on Figure 2.13.

Assuming the normality of the samples, Welch's unequal variances t-tests (Welch, 1947) are then run for each SAR acquisition date to check whether the mean mono- and bistatic scattering coefficients of the two orientation groups are statistically distinct, which would suggest that the orientation of the rows relative to the signal beam has a significant impact on the scattering measurements.

2.3.2 Regression analysis

The potential of multistatic versus monostatic scattering measurements for monitoring vegetation and soil variable dynamics is assessed using regression analysis with a simple linear and a Random Forest (RF) regression model (Breiman, 2001), in an approach similar to (Vreugdenhil et al., 2018).

Linear regressor

The mono- and bistatic scattering coefficients σ_0 are first averaged at the field level for each polarization channel. Then, for every possible pair of polarizations, ratios of monostatic scattering coefficients as well as monostatic to bistatic scattering coefficients (so-called multistatic) are computed. Both ratios and coefficients are subsequently converted to decibels. These ratios can be seen as a generalization of the cross-ratio (CR), i.e., VH/VV, a radar vegetation index particularly suitable for vegetation monitoring (Veloso et al., 2017).

Next, the linear dependence of the monostatic scattering coefficients, the ratios of monostatic scattering coefficients, and the multistatic ratios on the vegetation an soil biogeophysical variable measured *in situ* is assessed via simple linear regression analysis. To that end, each biogeophysical variable measurement is temporally matched with each monostatic scattering coefficient, as well as with each mono- and multistatic ratio of scattering coefficients.

Finally, simple linear regression models are then fitted on the data via ordinary least squares, and the comparative performance of the models is quantified by their coefficients of determination,

$$R^2 = 1 - \frac{\sum_{i=1}^{n}(y_i - \hat{y}_i)^2}{\sum_{i=0}^{n}(y_i - \bar{y})^2},$$

where y_i, $i = 1, \ldots, n$, are the observed scattering coefficients and ratios thereof, $\hat{y}_i$, $i = 1, \ldots, n$, are the predictions of the regression model, and $\bar{y}$ is the mean of the observations.

Random forest regressor

The analysis is then expanded using RF regressions which, contrary to linear regression, do not make assumptions on the predictive relationship between dependent and explanatory variables. RFs are ensemble machine learning methods. The forest is made up of a number of decision trees which are trained on a subsample of the training dataset that is drawn with replacement. The data that are left out of the subsample are called out-of-bag (OOB). These OOB data can be used to obtain an estimate of the regression error of the model, known as the OOB score.

RF regressors are therefore trained with bootstrap aggregation to predict each biogeophysical variable individually. Their features, i.e., the dependent variables, are the mono- and bistatic scattering coefficients in decibels. OOB R^2 scores are then calculated to assess each model's ability to capture the relationship between mono- and bistatic SAR data and the corresponding biogeophysical variable. Finally, the relative importance of the features for the prediction of each variable is estimated, to help identify informative inputs to the model (Antoniadis et al., 2021).

2.4 Results and discussion

2.4.1 Maize row orientation effect

The fields of which the scattering coefficient measurements are discussed in this section are the 37 fields described in Section 2.3.2. Except for the 7 BELSAR reference maize fields that were measured *in situ*, no information is available on these maize fields other than their relative orientation to the SAR beam.

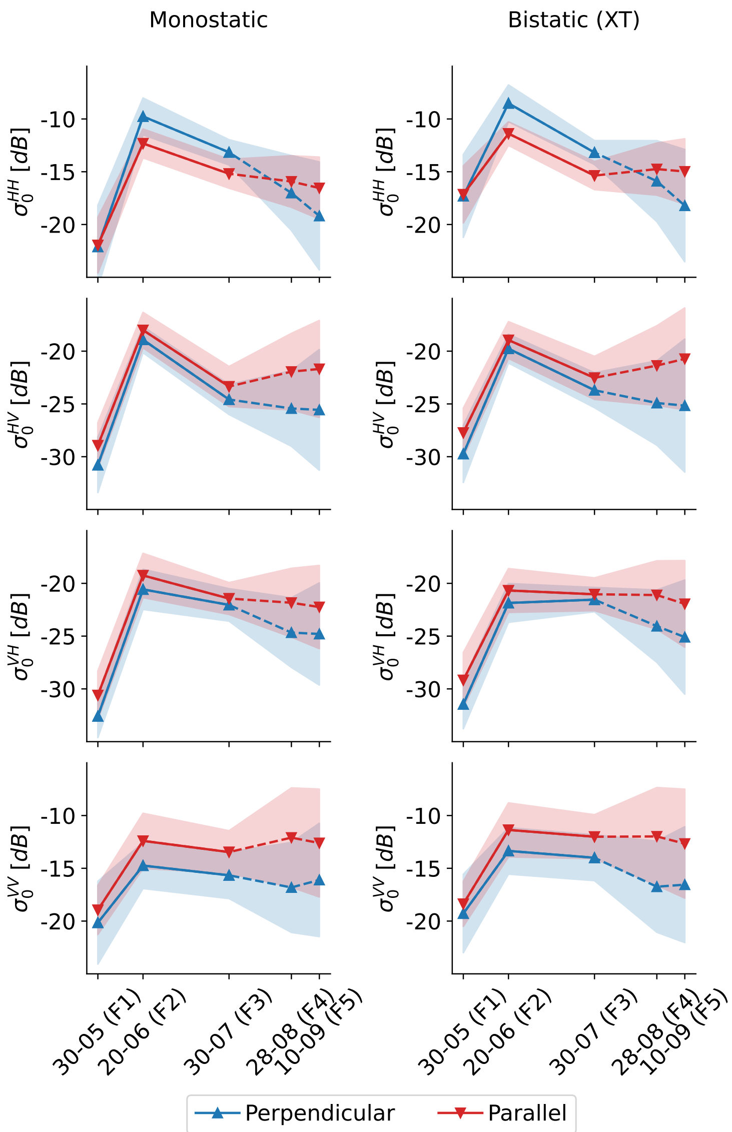

Figure 2.14: Time series of the average (**left**) monostatic and (**right**) bistatic (XT) scattering coefficients σ_0 in (**top to bottom**) HH, HV, VH, and VV polarizations for each orientation group. The translucent areas represent two standard deviations around the mean.

It is very unlikely that these fields were harvested (in sufficient numbers) before July 30 (F3) and likely that the majority were harvested before August 20 (F4), based on the reference fields and farming practices in the region of interest. This analysis will therefore focus on the first three acquisitions (F1 to F3).

Time series of average mono- and bistatic scattering coefficients for each orientation group are depicted on Figure 2.14. The sample size of both orientation group is similar for each acquisition date of interest. For the “perpendicular" group, the sample size is between 14 and 15 from F1 to F4 and 9 on F5. For the “parallel" group, the sample size is between 18 and 21. Furthermore, the acquisitions of the fields in each group have comparable incidence angle distributions and the maize crops show similar patterns of development. It is therefore very likely that the diverging behavior of the time series is mainly driven by the orientation of the maize rows relative to the signal beam.

The time series of monostatic and bistatic scattering coefficients are not significantly different from each other, except for the horizontal co-polarization, HH, where the separation between the two orientation groups for the second and third acquisitions is slightly larger in bistatic than in monostatic mode.

Welch’s t-tests performed for each acquisition date show that the two orientation groups significantly diverge from one another on June 20 (F2) and July 30 (F3), in both co-polarizations, HH and VV, but especially in the former. Before that, on May 30 (F1), both orientation groups are indistinguishable from one another in HH or VV, probably because the crop is still underdeveloped. After July 30 (F3), the maize fields are harvested gradually until mid-September (F5).

In HV, VH, and VV polarizations, the mean mono- and bistatic scattering coefficients for the group with fields the rows of which are (almost) parallel to the sensor beam is larger than that of the group with fields the rows of which are (almost) perpendicular to it, for each acquisition date. This is likely related to the the relatively small sample size, rather than to an effect of the rows. Indeed, this difference persists and even increases beyond harvest, when the fields are bare except for stem residues, which would presumably be unlikely were the number of fields in each group larger. In horizontal co-polarization, HH, however, for the second (F2) and third (F3) acquisitions, fields with rows perpendicular to the

SAR beam have a higher values of scattering coefficients than those the rows of which are parallel to it. This does not hold true for the first (F1) acquisition, when the crop is not yet fully developed, nor for the fourth (F4) and fifth (F5) acquisitions, which take place after the beginning of the harvest.

These observations seem to point to an effect of the relative orientation of the maize rows, and thus the row structure of the canopy, in both HH and VV, but that is far more pronounced in the former, while for the cross-polarizations, HV and VH, no effect is discernible.

These results are consistent with other studies on the effect of row orientation on backscatter measurements. In their experimental study on the effect of sugar-cane planting row direction on PALSAR (L-band) imagery, Araujo Picoli et al. (2013) report that in HH the values of backscattering coefficient are higher for fields with perpendicular rows than for those with parallel rows. For HV, however, the find no statistically significant effect of the planting row direction. Multiple theoretical investigations have also shown that the row orientation has a significant effect on backscatter measurements in co-polarization, and especially in HH, e.g., Sharma et al. (2020), Wegmüller et al. (2011), and Zribi et al. (2002). However, in these model studies, qualitatively similar behaviors are reported for HH and VV, which is not apparent here. Regarding the impact of the row structure of crops on bistatic radar measurements, there is, to our knowledge, no published study on the subject.

2.4.2 Sensitivity assessment

The coefficients of determination, R^2, of the simple linear regression models fitted on the radar and biogeophysical measurements are depicted in Figure 2.15, and the results of the RF regression analysis are reported in Table 2.2.

Linear sensitivity to soil moisture and roughness in bare fields

The sensitivity of both monostatic and multistatic radar systems to soil moisture is assessed in recently harvested, and hence bare, winter wheat fields.

Monostatic scattering coefficients in co- and cross-polarizations (HH, HV, VH, and VV) are linearly sensitive to soil moisture in bare fields,

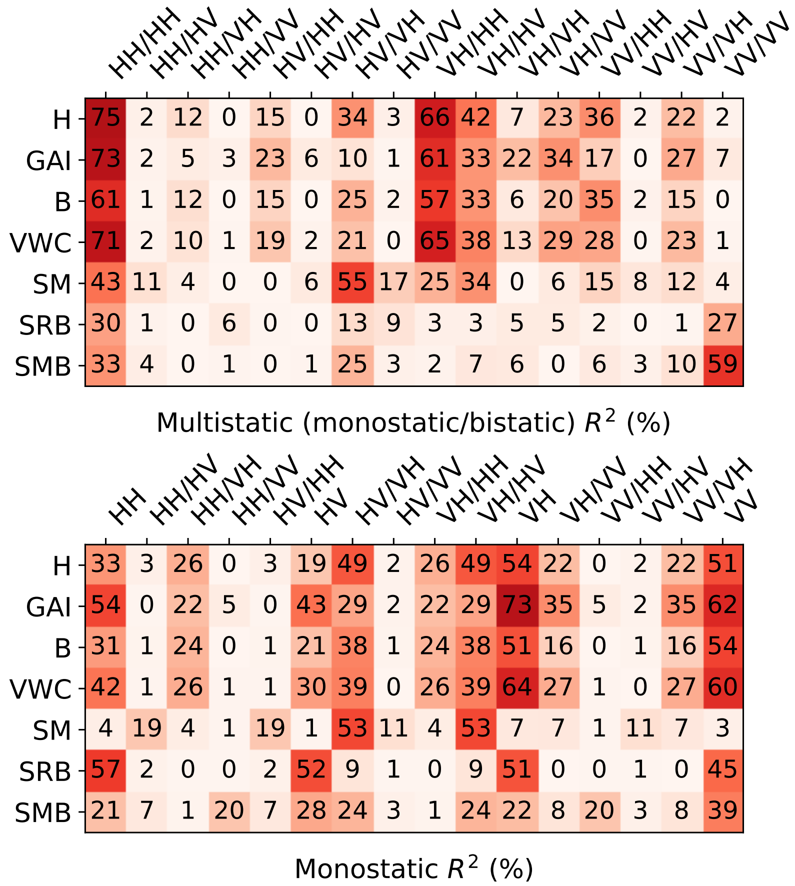

Figure 2.15: Coefficients of determination, R^2 (%), of simple linear regressions between (**top**) multistatic ratios, i.e., ratios of monostatic to bistatic (XT) scattering coefficients, (**bottom**) monostatic scattering coefficients and their ratios, and, for maize crops ($n = 26$), plant height (H), green area index (GAI), biomass (B), vegetation water content (VWC), soil moisture under canopy (SM), as well as, for bare winter wheat fields, soil moisture (SMB ; $n = 36$) and mean RMS height (SRB ; $n = 37$).

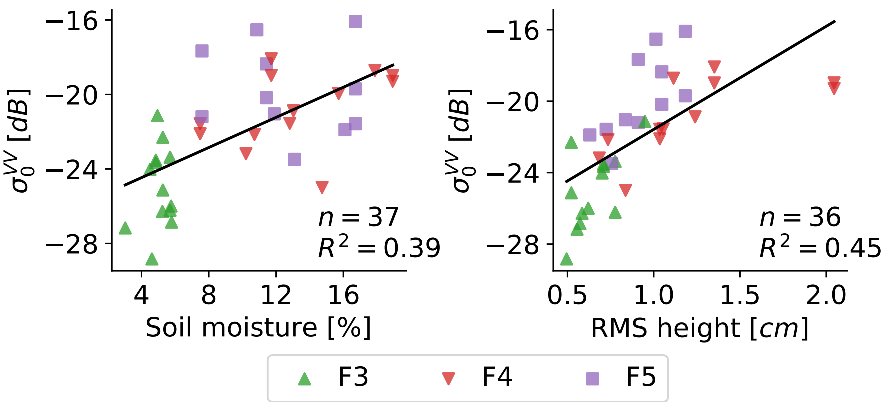

Figure 2.16: Scatter plots of the monostatic scattering coefficient σ_0 in VV as a function of (**left**) the volumetric soil moisture and (**right**) the RMS height measured *in situ* in the BELSAR reference winter wheat fields after the harvest (bare).

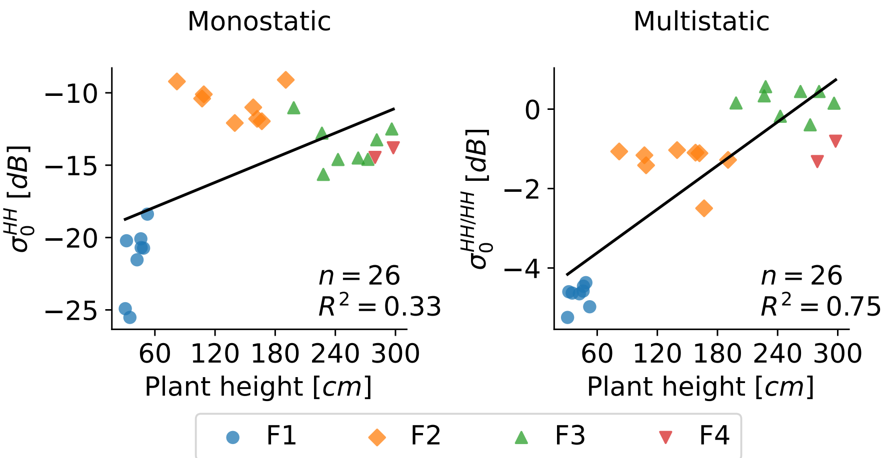

Figure 2.17: Scatter plots of (**left**) the monostatic scattering coefficient σ_0 in HH and (**right**) the (multistatic) ratio of monostatic to bistatic scattering coefficients in HH as a function of the plant height measured *in situ* in the BELSAR reference maize fields.

i.e., the field average monostatic scattering coefficients increase with soil moisture. A relatively high correlation is found for VV in particular, with a R^2 score of 39 %. However, all four monostatic scattering coefficients also show high R^2 scores for surface roughness, which might indicate that the signal is sensitive to it as well as to soil moisture, as depicted in Figure 2.16. This makes the soil moisture retrieval from monostatic observations challenging, particularly in the horizontal co-polarization, HH, for which a relatively high R^2 score of 57 % is found for the surface roughness, i.e., 36 percentage points higher than its score for soil moisture. As for the ratios of monostatic scattering coefficients, they all have relatively low R^2 scores for both soil moisture and surface roughness.

Regarding the multistatic system, the ratio of vertically copolarized multistatic scattering coefficients, VV/VV, shows relatively high R^2 scores for soil moisture, with 59 %, while having a low score for surface roughness, with 27 %. It thus seem to be marginally more sensitive to soil moisture than to surface roughness, which could suggest that using multistatic scattering observations might mitigate the impact of surface roughness in soil moisture retrieval, as opposed to monostatic ones.

Linear sensitivity to biogeophysical variables in vegetated fields

In vegetated maize fields, the coefficients of determination suggest that the multistatic system might be moderately more sensitive to the vegetation biophysical variables compared to the monostatic one. The multistatic system allows predicting, from the best performing polarization ratio for each vegetation variable, 75, 73, 61, and 71 % (all in HH/HH) of the variance in maize plant height, green area index, biomass, and vegetation water content, outperforming the monostatic system by 21 (VH), 7 (VV), and 7 % (HV/VH) for each biophysical variable except the GAI, respectively, for which the score is equal for both systems. With regards to the soil moisture under the canopy, both the monostatic and the multistatic systems have similar R^2 scores, respectively 55 (HV/VH) and 53 % (HV/VH and VH/HV). These are almost on par with the scores for the canopy variables, which is fairly surprising given the attenuation of the signal by the vegetation.

For the monostatic system, the vertical co- and cross-polarizations, VV and VH, have similar performances and largely outperform all other polarizations and ratios thereof, with the significant exception of the soil moisture under the canopy, to which only the cross-polarization ratios (HV/VH and VH/HV) seem sensitive. For its multistatic counterpart, however, the best choice for maize monitoring would by far be the ratio of horizontally co-polarized monostatic to bistatic scattering coefficients HH/HH. It is noteworthy that the vertical polarization VV does not seem to bring any gain in terms of sensitivity to vegetation variables to the multistatic system in this configuration.

The multistatic ratios, HV/HV, VH/VH, and VV/VV, have near-zero R^2 for all maize biophysical variables, as well as for the surface soil moisture under the canopy. This indicates that the ratios are (almost) constant and thus the information content of mono- and bistatic acquisitions is the same for HV, VH, and VV. Conversely, in HH polarization, bistatic acquisitions seem to increase the information content of the system compared to monostatic acquisitions alone. For example, Figure 2.17 illustrates the impact that the addition of a bistatic component to the system, via its use in a ratio, has on the relationship between maize plant height and radar measurements in horizontal co-polarization. This suggests that in HH the acquisitions have a greater dependence in the acquisition geometry of the sensors forming the bistatic system than the other polarizations. These results are therefore in agreement with the results of the analysis of the effect of the vegetation row structure in Section 2.4.1, which show that measurements in horizontal co-polarization, HH, are significantly more impacted by the anisotropy of the target induced by the row structure of the vegetation canopy.

It is noteworthy that the discrepancies between the coefficients of determination reported in Figure 2.15 for the cross-polarization channels, HV and VH, of the monostatic system suggest that the reciprocity theorem does not hold true for vegetated maize fields. It does seem to be valid to a reasonable degree, however, for bare soils in harvested winter wheat fields. The reason for this difference between vegetated and bare fields might be due to the theorem being only valid for quiet environments, an assumption that is not always verified in real conditions as also reported in Totir et al. (2011), or because of the anisotropic nature of the target (Pierdicca et al., 2021).

Table 2.2: Out-of-bag (OOB) R^2 scores and feature importance from RF regressors trained to predict, for maize crops ($n = 26$), plant height, green area index (GAI), biomass, vegetation water content (VWC), soil moisture under canopy (SM), and, for bare winter wheat fields, soil moisture (SMB ; $n = 36$) and RMS height (SRB ; $n = 37$), from mono- and bistatic (XT) scattering coefficients.

Biogeophysical variable		**OOB R²**	**Feature importance**							
			Monostatic				**Bistatic**			
			HH	**HV**	**VH**	**VV**	**HH**	**HV**	**VH**	**VV**
Plant height (cm)	H	0.80	0.13	0.02	0.05	0.18	0.08	0.03	0.26	0.26
Green area index ($m^2\,m^{-2}$)	GAI	0.77	0.05	0.02	0.11	0.26	0.01	0.03	0.15	0.36
Biomass ($kg\,m^{-2}$)	B	0.77	0.10	0.03	0.07	0.18	0.05	0.03	0.31	0.24
Vegetation water content ($kg\,m^{-2}$)	VWC	0.83	0.07	0.01	0.06	0.18	0.04	0.03	0.31	0.30
Soil moisture (%)	SM	0.45	0.07	0.18	0.08	0.14	0.16	0.10	0.11	0.15
RMS height after harvest (cm)	SRB	0.47	0.16	0.04	0.06	0.25	0.25	0.05	0.16	0.04
Soil moisture after harvest (%)	SMB	0.32	0.08	0.06	0.07	0.51	0.07	0.11	0.07	0.05

Random forest regression analysis

The OOB R^2 scores of the RF regressors, reported in Table 2.2, are high for the vegetation biophysical variables, with 0.80 for the plant height, 0.77 for the GAI, 0.77 for the biomass, and 0.83 for the plant water content, but low for soil moisture, under the canopy and on bare soil, and its roughness, with scores of 0.45, 0.47 and 0.32 respectively. Compared to RF regressors trained with monostatic data only, the OOB R^2 scores obtained using both mono- and bistatic data are consistently higher for all variables except plant height and bare soil moisture and roughness, for which the OOB R^2 are 0.85, 0.54, and 0.38, respectively. High OOB scores indicate the model's ability, or conversely its inability in the case of a low score, to capture the relationship between the variable in question and the mono- and bistatic coefficients (HH, HV, VH, and VV). The fact that these scores are higher than the best results reported in the linear regression analysis highlights the value of using all available polarimetric information.

The low scores for soil moisture and soil roughness suggest that soil moisture cannot be readily retrieved from mono- or bistatic scattering coefficients, probably because of their entanglement. On the other hand, high scores for vegetation variables attest to the potential of L-band SAR for monitoring maize dynamics throughout the growing season. For the latter, feature importance analysis even indicates that bistatic data provide complementary information to the monostatic sensor. The bistatic vertical cross- and co-polarizations, VH and VV, are indeed the most discriminating features among all scattering coefficients. As for the monostatic coefficients, the most informative polarization for vegetation variables is distinctly VV and not VH, while data in the latter polarization showed an equally strong linear relationship in general as the former in the linear regression analysis.

Finally, the results are almost identical in decibels or natural units. The latter were therefore not reported here. This is to be expected with an RF regressor since the form of the relationship between dependent and independent variables is not defined in advance, unlike in simple linear regression, for example.

2.5 Conclusions

In this study, we assessed the potential of multistatic SAR for crop and soil moisture monitoring. The results confirm that L-band SAR is well suited to monitoring vegetation dynamics in maize crops. They also suggest that multistatic SAR systems are somewhat more sensitive to maize crop biophysical variables than purely monostatic ones, even with very short bistatic angles and baselines. Moreover, the analysis highlighted the effect of the maize row orientation relative to the SAR beam. The row planting direction was shown to have a significant impact on the mono- and bistatic scattering measurements in L-band in both co-polarizations, but especially in HH, as soon as the stem elongation phase.

Concerning soil moisture and surface roughness, the results were more contrasted. Linear regression analysis suggested an advantage in using simultaneous mono- and bistatic scattering data for soil moisture retrieval, as the latter seemed to provide additional information which would enable the disentanglement of their respective contributions. However, the random forest regression analysis also demonstrated the inherent difficulty of capturing the relationship between soil moisture and scattering coefficients, pointing to the need for a physics-based modeling approach for this application.

It should be pointed out that, despite the merits of using an empirical dataset in an attempt to substantiate previous theoretical studies, the BELSAR sample size is fairly small. This implies, for example, making the assumption that the data evenly collected on three to four separate occasions over the course of five months, depending on the field, are representative of the entire growing season despite the low temporal distribution of the sample. Furthermore, the results of this assessment were derived from data acquired in the backward region, with a very small bistatic angle ($\sim 1°$), i.e., in a quasi-monostatic configuration. From theoretical studies on the scattering properties of vegetation and soil, however, it is expected that multistatic systems with considerably larger bistatic baselines and angles—with the bistatic sensor in the forward region—could significantly improve the accuracy of vegetation and soil biogeophysical variables retrieval. A larger data set with a greater range of acquisition geometries would therefore be needed to draw general conclusions about the performance of multistatic systems for applications in agriculture and soil monitoring.

Finally, with regard to future spaceborne SAR missions, this study helps to demonstrate the value of L-band SAR for agricultural applications and, to a lesser extent, the merits of multistatic systems. The relatively low capacity of C- and X-band sensors, the only ones currently widely available, for monitoring high-biomass crops such as maize, could be remedied by L-band sensors thanks to their higher penetration ability into the vegetation. As for the expected benefits of launching a multistatic system into space—or even just a bistatic sensor to passively accompany an existing monostatic platform such as the forthcoming NISAR and ROSE-L—the results have demonstrated the limited advantage of the quasi-monostatic configuration of the sensors used in the BELSAR campaign over traditional monostatic systems. This study therefore further highlights the existing trade-off between the need to have a very small baseline between sensors for certain interferometric applications, and the usefulness of a large baseline to significantly increase the information content of the captured signal for improving agricultural and hydrological applications.

Chapter 3

Semi-empirical model inversion for green area index and soil moisture retrieval

This chapter is adapted from:

Jean Bouchat, Emma Tronquo, Anne Orban, Xavier Neyt, Niko EC Verhoest, and Pierre Defourny (2022a). "Green Area Index and Soil Moisture Retrieval in Maize Fields Using Multi-Polarized C-and L-Band SAR Data and the Water Cloud Model". In: *Remote Sensing* 14.10, p. 2496. DOI: `10.3390/rs14102496`

—

Abstract

The green area index (GAI) and the soil moisture under the canopy are two key variables for agricultural monitoring. Currently, most large-scale GAI estimation methods exploit optical data and are rendered ineffective in the case of frequent cloud cover. Synthetic aperture radar (SAR) measurements could allow the remote estimation of both variables at the parcel level regardless of clouds. In this study, several methods were implemented and tested for the simultaneous estimation of both variables using a semi-empirical model and dual-polarized radar backscatter measurements. The results were then contrasted against those obtained with knowledge of one variable while estimating the other. The methods were tested on the BELSAR dataset consisting of *in situ* measurements of biogeophysical variables of vegetation and soil in maize fields combined with multi-polarized C- and L-band SAR data from Sentinel-1 (S1) and BELSAR. Accurate GAI estimates were obtained from jointly estimating the two variables of interest using a Random Forest (RF) regressor for the inversion of a pair of semi-empirical models calibrated using cross- and vertical co-polarized SAR data in L- and C-band, with correlation coefficients of 0.79 and 0.65 and root-mean-square errors (RMSEs) of $0.77\,\mathrm{m}^2\,\mathrm{m}^{-2}$ and $0.98\,\mathrm{m}^2\,\mathrm{m}^{-2}$ respectively between estimates and *in situ* measurements. The method, however, proved inadequate for soil moisture monitoring in the conditions of the campaign. These results indicate that GAI retrieval in maize crops using only dual-polarized radar data could successfully substitute for estimates derived from optical data when they are not available, such as in the case of persistent cloud cover. They also further highlight the relevance of L-band SAR for agricultural monitoring.

3.1 Introduction

Monitoring the growth, health, and performance of crops throughout the growing season is an important aspect of agricultural management at the farm, regional or even global scale. Two variables of great relevance for crop monitoring are the green area index (Delegido et al., 2015; Duveiller et al., 2012) and the surface moisture content of the soil under the canopy. Field measurements of those variables are, however, often too cumbersome to be carried out at large scale, whereas remote sensing can provide timely, cost-effective, and possibly accurate estimation methods.

Most well-established operational agricultural monitoring systems today rely on optical remote sensing systems. These have been successfully used for GAI retrieval, e.g., Amin et al. (2021), Delloye et al. (2018), Clevers et al. (2017), and Verrelst et al. (2015), as well as for the estimation of surface soil moisture, though less effectively, e.g., Verstraeten et al. (2006), Van doninck et al. (2011), Qin et al. (2013), Babaeian et al. (2018), and Rahimzadeh-Bajgiran et al. (2013). However, in many parts of the world, they are frequently impeded by the presence of clouds obscuring the view of the sensors (Whitcraft et al., 2015; Wang et al., 2009).

Unlike the latter, synthetic aperture radars are weather-independent, active sensors able to penetrate the vegetation as well as the soil underneath in order to extract valuable information on them thanks to the sensitivity of microwaves to the dielectric and geometric properties of the objects with which they interact.

The sensitivity of SAR to the GAI and surface soil moisture of maize fields has been investigated in numerous empirical studies. Jiao et al. (2010) reported high correlation coefficients between SAR backscatter signatures and GAI in maize in X-, C-, and L-band from TerraSAR-X, RADARSAT-2, and PALSAR respectively, which are the most commonly used frequency bands for agriculture monitoring. The frequency band of the radar signal is in fact a determining factor in its sensitivity to both GAI and soil moisture, mainly because the penetration depth of the signal into the canopy largely depends on it. In maize, a saturation phenomenon tends to occur to backscatter in C-band for GAI values exceeding 3 (Jiao et al., 2011) to $4\,\mathrm{m}^2\,\mathrm{m}^{-2}$ (Beriaux et al., 2013). The penetration depth of the radar signal is even more decisive for soil moisture monitoring. If it is too shallow, microwaves cannot reach and interact with the ground, rendering the soil contribution to the backscatter negligible and the signal insensitive to surface soil moisture (Ulaby et al., 1986). In their study on the penetration capabilities of SAR signals in C- and L-band, El Hajj et al. (2018) reported that L-band waves can penetrate a well-developed vegetation cover of wheat or grass, i.e., with a normalized difference vegetation index (NDVI) larger than 0.7, and reach the underlying ground, whereas C-band waves proved to be more limiting. Backscatter data in L-band is therefore expected to allow for the monitoring of both vegetation biophysical variables and soil moisture in maize fields further into the later stages of the plant development than backscatter in X- or C-band. Besides soil and vegetation characteristics, the sensitivity to GAI and soil moisture is also dependent on the sensor incidence angle and polarization. At shallow incidence angles the contribution of the soil is reduced (Ulaby et al., 1986) while the vegetation contribution to the signal is enhanced (Blaes et al., 2006). At steep incidence angles, the attenuation of the signal by the vegetation is diminished and the soil contribution to the backscatter increases (Veloso et al., 2017). Regarding the polarization of the signal, the potential of the dual-polarized C-band data from S1, and especially the ratio of its two available polarizations, for maize monitoring through its GAI, was highlighted in Veloso et al. (2017), Vreugdenhil et al. (2018), and Khabbazan et al. (2019). Meanwhile, multiple studies have demonstrated the suitability of multi-polarization C- (Yang et al., 2012; Gherboudj et al., 2011) and L-band (Bhogapurapu et al., 2022) data for soil moisture monitoring under a vegetation cover.

The retrieval of crop biophysical variables as well as the surface soil moisture from under their canopy using radar data has been addressed with varying degrees of success since the eighties, e.g., Pampaloni and Paloscia (1986), Karam et al. (1992), Toure et al. (1994), Ferrazzoli et al. (2000), Macelloni et al. (2001), Della Vecchia et al. (2006a), and Konings et al. (2017). One of the more widely used approaches for the operational monitoring of crops was proposed by Attema and Ulaby (1978) and then reformulated by Prévot et al. (1993). The idea behind this approach was to determine a simplified solution to the radiative transfer (RT) equation formulated for a medium where the canopy of the crop is represented by a cloud of identical and randomly distributed water droplets held in place by the vegetation matter (Leeuwen, 1996). It resulted in a semi-empirical model for the backscattering coefficient of vegetated surfaces, called Water Cloud model (WCM), which has been successfully used in a number of studies for the retrieval of various crop biophysical variables, e.g., Bériaux et al. (2015), Chauhan et al. (2018), and Park et al. (2019), and of the surface soil moisture in the presence of a crop, e.g., Lievens and Verhoest (2011), Liu and Shi (2016), Baghdadi et al. (2017), Wang et al. (2021), Rains et al. (2021), and Zribi et al. (2019). The WCM simulates the radar backscattering coefficient of crops as the incoherent sum of the scattering from the vegetation layer and the contribution from the underlying soil attenuated by the canopy. The contribution of the soil is mainly driven by the surface soil moisture and the surface roughness, which can in some cases be neglected if it does not vary during the observation period. In its reformulated version by Prévot et al. (1993), the contribution of the vegetation depends on one to two canopy descriptors, e.g., the GAI, which can then be retrieved by the inversion of the model with radar data and ancillary information on the contribution of the soil, mainly through its surface moisture (Bériaux et al., 2011). However, relying on *in situ* measurements or estimates of the surface soil moisture to retrieve the GAI of a crop renders the use of the WCM for operational crop monitoring impractical, even at moderately large scale. To circumvent this problem, a system formed by a pair WCMs calibrated using different polarizations can be solved to simultaneously retrieve the GAI and the surface soil moisture of crops, dispensing with the need for *in situ* measurements or estimates of the latter. The feasibility of this method was investigated for the retrieval of the GAI of maize crops from C-band data using multiple inversion strategies (Mandal et al., 2019), as well as the estimation of the biomass and soil moisture in winter wheat fields (Hosseini and McNairn, 2017) and the GAI in maize and soybean fields (Hosseini et al., 2015) from C- and L-band multi-polarized SAR data, and retrieval accuracies similar to those of methods based on optical remote sensing were reported.

This study leverages parts of the BELSAR dataset (Bouchat et al., 2024), described in-depth in Chapter 2, as well as SAR acquisitions from S1. The data therefore consist of C- and L-band SAR data as well as concurrent field measurements of biogeophysical variables of the vegetation and underlying soil acquired in eight maize fields representative of the Hesbaye region of Belgium. Its aim is to develop and assess the potential of a method using a semi-empirical model derived from a relaxation of the physical constraints of the WCM for the retrieval of the GAI in maize crops, as well as, secondarily, the surface soil moisture under the canopy, with SAR and *in situ* data from the BELSAR field campaign. First, the sensitivity of L-band backscatter to the maize GAI, the surface soil moisture under the canopy, and the incidence angle of the SAR beam, is assessed by means of a regression analysis, as well as forward modeling of the semi-empirical model. Then, the ability of the semi-empirical model to allow the retrieval of one of the two aforementioned variables at a time, with knowledge of the other, is investigated for each available SAR frequency and polarization. Finally, an algorithm is implemented for the simultaneous retrieval of both GAI and volumetric surface soil moisture in maize crops using only multi-polarized backscatter data and the incidence angle of the SAR beam, and its results are compared to those obtained with ancillary data on GAI or soil moisture.

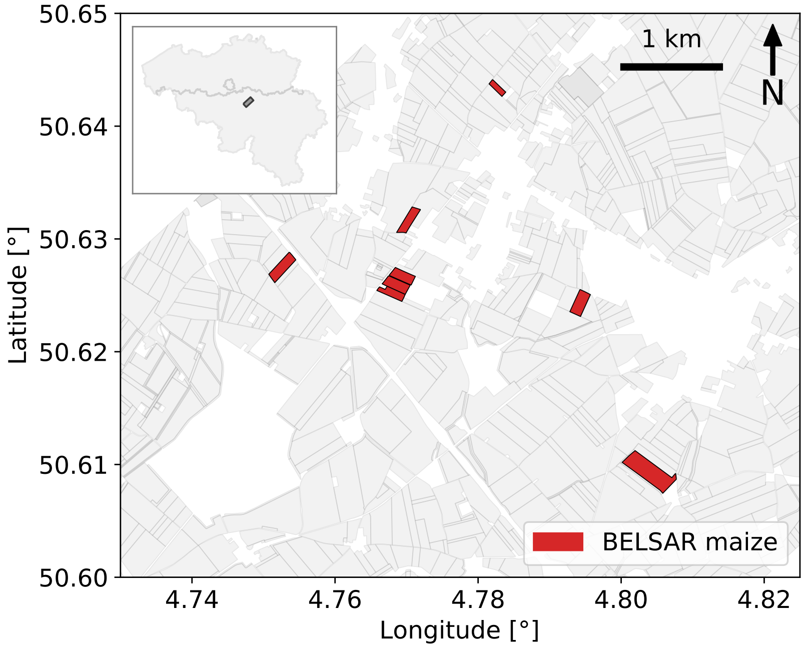

Figure 3.1: Subset of the BELSAR AOI, with all eight maize fields considered in this study in red, and other agricultural fields inventoried in the anonymized land parcel identification system of Wallonia, Belgium, in grey.

3.2 Data

This section merely provides the elements that are strictly necessary to understand the results presented in the present study. A in-depth description of the dataset can however be found in Chapter 2.

3.2.1 Site description

The BELSAR airborne and field campaign that yielded the dataset used in this study took place during the 2018 growing season, between the end of May and mid-September, in the BELAIR HESBANIA test site, between Gembloux and Sint-Truiden, Belgium. The site, which is depicted in Figure 3.1, belongs to the global Joint Experiment for Crop

Table 3.1: Acquisition dates (day-month format) of the L- and C-band SAR images from BELSAR and Sentinel-1, respectively, and of the corresponding *in situ* measurements of vegetation and soil variables.

ID	SAR measurements		*In situ* measurements	
	BELSAR	**Sentinel-1**	**Vegetation**	**Soil**
F1	30-05	28-05	31-05 and 01-06	29-05
F2	20-06	21-06	21-06 and 22-06	20-06
F3	30-07	02-08	02-08	26-07
F4	28-08	26-08	29-08	28-08

Assessment and Monitoring (JECAM) network. It corresponds to a typical landscape of intensive agriculture of the Hesbaye region. It is mostly covered by relatively large, homogeneous, flat fields with a uniform topsoil texture of silt loam.

3.2.2 SAR data

L-band from BELSAR

The L-band SAR data were collected from an airborne radar system operated by MetaSensing BV during the BELSAR campaign in a series of flights taking place approximately one month apart during the growing season of maize. Four radar acquisitions, named F1, F2, F3, and F4, coincided with the presence of maize crops in the imaged area, in Figure 3.1. Concurrent *in situ* measurements of biogeophysical variables of crop and soil were recorded in 10 maize fields following each of the flights, 8 of which were actually imaged and are therefore included in this study. The dates of the airborne acquisitions and the corresponding *in situ* measurements are reported in Table 3.1.

The airborne L-band SAR system from MetaSensing BV (Macedo et al., 2019) used in this study consisted of a left-looking sensor operating at a central frequency of 1.375 GHz, with a 50 MHz bandwidth, and delivering fully polarimetric (HH, HV, VH, VV) radar images. In this study, the cross-polarization channels, HV and VH, were averaged and the resulting channel was called HV to distinguish it from its C-band counterpart.

Radar data were processed by MetaSensing BV using the time-domain back-projection algorithm, performing motion compensation, and delivered as σ-calibrated single-look complex (SLC) focused SAR data. These radar images were co-registered based on the absolute position accuracy of the navigation data, i.e., around 0.75 m, and released in ground range geometry with a ground sampling distance of 1 m.

Four trihedral corner reflectors were deployed on site and used as standard point targets for the radiometric and polarimetric calibrations that were performed according to the procedure described in Fore et al. (2015). The radiometric calibration providing the σ_0 was based on the corner reflectors' response and the calibration constant K was evaluated for each flight, F1 to F4. A polarimetric calibration was also applied in order to insure the images acquired in the different polarization channels correctly reflected the dependence of the target response to the polarization state of the signal. Data were calibrated for co-pol and cross-pol channel imbalances, that is amplitude and relative phase differences between polarization channels, at both transmission and reception. Cross-talk was considered negligible, based on the obtained polarimetric signatures and the impulse response function (IRF) of the corner reflectors showing sufficiently good isolation between the polarization at antenna level.

A 20 m inner buffer was applied to the boundaries of the fields in which *in situ* data were collected to reduce border effects. Values of L-band backscattering coefficients σ_0 and incidence angle were then averaged over each of these fields. Their time series are represented in Figure 3.2. It is noteworthy that, compared with Chapter 2, only monostatic data from the BELSAR campaign are used in this study.

C-band from Sentinel-1

S1 is a constellation of two polar-orbiting satellites carrying SAR systems operating in C-band, at 5.405 GHz. The constellation, launched in 2014 and 2016, was designed and is operated by the European Space Agency (ESA) to provide radar imagery for the Copernicus program of the European Commission. Following an anomaly at the end of December 2021, one of the two satellites of the constellation is no longer operational, doubling the revisit period. The replacement of the faulty

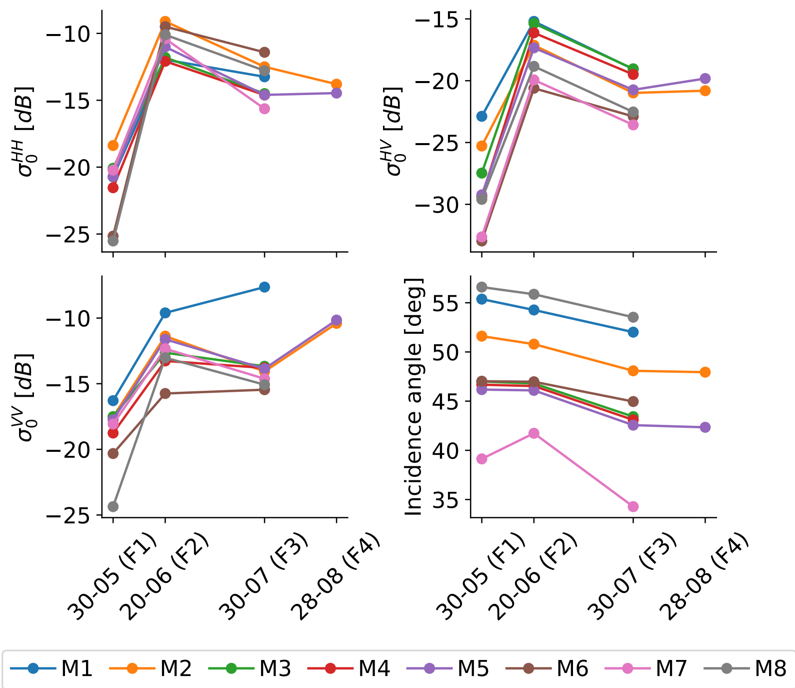

Figure 3.2: Time series of average L-band backscattering coefficient σ_0 and incidence angle acquired from an airplane during the BELSAR-Campaign. M1 to M8 designate the maize fields in which data were collected.

sensor is scheduled for Q4 2024.

The study site in Figure 3.1 is imaged by the SAR systems of the S1 constellation from four different relative orbits, numbered 37, 88, 110, and 161. Each relative orbit provides an image of the area of interest (AOI) every 6 days in interferometric wide (IW) swath mode. However, in order to limit the effects of the morning dew and those resulting from modifications of the observation geometry, all the images used in this study were acquired from the relative orbit number 161. In this ascending orbit, the sensors pass over the AOI at 5:32 pm, with a mean incidence angle for the area of about 42°. The satellite images were acquired on May 28, June 21, August 2 and August 26, with a maximum of 3 days of separation (mean 1.5 days) from the dates when *in situ* measurements

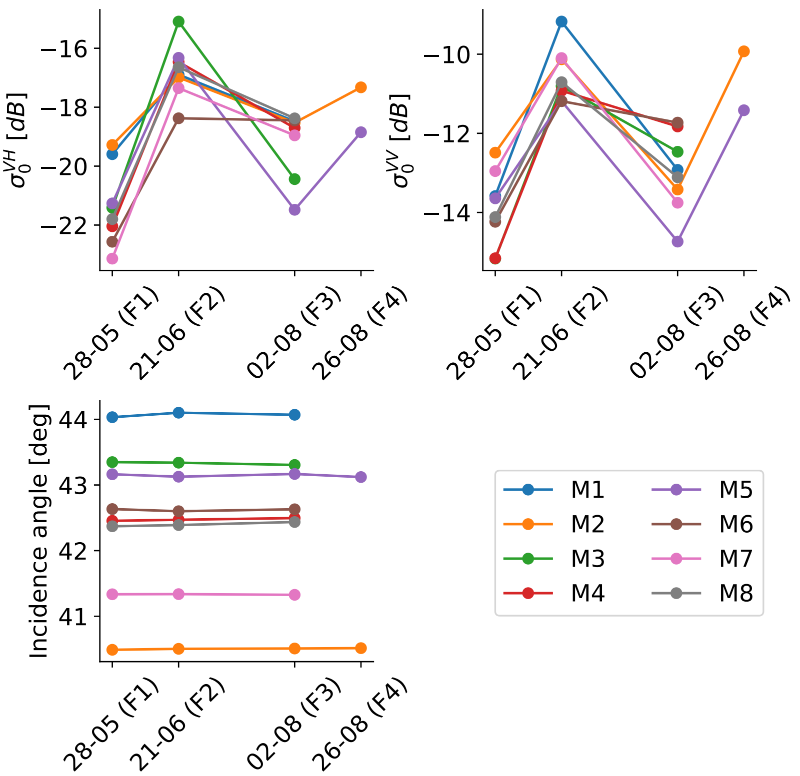

Figure 3.3: Time series of average C-band backscattering coefficient σ_0 and incidence angle from Sentinel-1 (relative orbit 161, ascending) imagery. M1 to M8 designate the maize fields in which data were collected.

of biogeophysical variables were recorded in maize fields.

S1 data were processed with ESA's Sentinel-1 toolbox (S1TBX) using the Sentinel Application Platform (SNAP) (*SNAP – ESA Sentinel Application Platform v8.0.0*, 2020). The three main processing steps applied to the Level-1 SLC data in IW mode were, in order, the thermal noise removal, the radiometric calibration to obtain backscattering coefficients σ_0, and the range Doppler terrain correction using the Shuttle Radar Topography Mission (SRTM) 1 Arc-Second Global digital elevation model (DEM) (Eros, 2015). This procedure resulted in images of backscattering coefficients σ_0 and incidence angles with a 10 m ground sampling distance.

As with the L-band data, a 20 m inner buffer was applied to the fields in which *in situ* data were collected and values of C-band backscattering coefficient σ_0 and incidence angle were then averaged over each of them. Their time series are represented in Figure 3.3.

3.2.3 *In situ* measurements of vegetation and soil variables

Synchronously with each airborne SAR acquisition, biogeophysical variables of vegetation and underlying soil were collected in eight maize fields in the imaged area, for a total of 26 data points. The fields are flat and homogeneous, with a surface area ranging from 1 to around 9 ha. Their location in the AOI is depicted in Figure 3.1, and the correspondence between the acquisition dates of the radar images and the *in situ* measurements can be found in Table 3.1.

Maize crop biophysical variables were collected in three representative plots inside each of the 8 reference fields, and then averaged at the field level. These plots were selected according to their NDVI, which had been computed from Pleiades images days prior to the start of the campaign. For each of the three plots in each reference field, GAI measurements were derived from 10 digital hemispherical pictures (DHPs), one every 3.75 m, with an approximate nadir view 1 m above the crop canopy, using the CAN-EYE software. The phenological development stage of the plants in each plot was also recorded. When first surveyed, on May 31 (F1), the maize plants were at the leaf development stage, with 5 to 8 leaves already unfolded. Then, on June 21 (F2), the plants were at the stem elongation stage, with 2 to 5 nodes detectable. Next, on August 2 (F4), the crops were ripening and at their dough stage, with kernels yellowish at around 55 % dry matter. Finally, on August 28, only 2 fields remain unharvested and are fully ripe, with kernels hard and shiny at about 65 % dry matter. These observations were described using the BBCH-scale (Meier, 1997).

Volumetric soil moisture measurements were conducted using time domain reflectometry (TDR) sensors with 11 cm rods. At least 10 locations per reference field were monitored with three repetitions per location. All soil moisture measurements within each field were averaged to

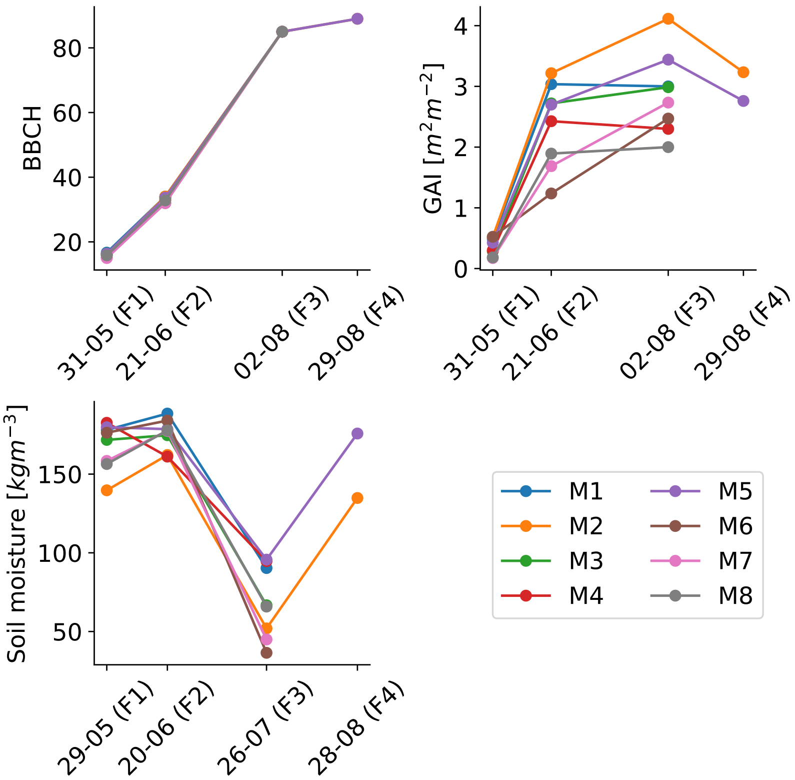

Figure 3.4: Time series of BBCH, volumetric surface soil moisture, and GAI measured *in situ* in eight maize fields, M1 to M8, during the BELSAR-Campaign.

provide field average soil moisture values. The range of measured soil moisture values is 36 to 188 $\mathrm{kg\,m^{-3}}$. In Belgium, such low range depicts unusually dry conditions for the season. The summer of 2018 was indeed marked by an exceptional drought that accelerated the maturation of crops, which were consequently harvested several weeks earlier than usual.

Time series of the vegetation and soil biogeophysical variables collected *in situ* in the reference fields are represented in Figure 3.4.

Table 3.2: Mean and standard deviation of several biophysical variables measured in the eight maize fields during the BELSAR campaign. Height and VWC designate the plant height and the vegetation water content. Dates are in the day-month format.

Date (ID)	BBCH		GAI [$m^2\,m^{-2}$]		Height [cm]		Biomass [$kg\,m^{-2}$]		VWC [$kg\,m^{-2}$]	
	Mean	**Std**	**Mean**	**Std**	**Mean**	**Std**	**Mean**	**Std**	**Mean**	**Std**
31-05 (F1)	15.8	0.6	0.4	0.1	40.4	8.2	0.2	0.1	0.2	0.1
21-06 (F2)	33.0	0.8	2.2	0.7	133.0	37.9	2.9	1.2	2.4	1.0
02-08 (F3)	85.0	0.0	2.8	0.6	245.3	33.9	5.2	0.9	3.8	0.7
29-08 (F4)	89.0	0.0	3.0	0.3	288.7	10.0	9.0	0.6	5.4	0.6

3.3 Methodology

3.3.1 SAR signal modeling

Semi-empirical model

The semi-empirical model used to simulate the radar backscatter from maize fields is based on a relaxed version of the WCM (Prévot et al., 1993). The WCM is a semi-empirical model that simulates the backscattering coefficient of a vegetated field, σ_0^{tot}, in natural units, as the incoherent sum of the scattering from the vegetation, σ_0^{veg}, and the contribution from the underlying soil, σ_0^{soil}, attenuated by the canopy,

$$\sigma_0^{\text{tot}} = \sigma_0^{\text{veg}} + \tau^2 \sigma_0^{\text{soil}}. \tag{3.1}$$

The contribution of the vegetation is described as

$$\sigma_0^{\text{veg}} = AV_1 \cos(\theta)(1 - \tau^2), \tag{3.2}$$

where

$$\tau^2 = e^{-2BV_2 \sec(\theta)} \tag{3.3}$$

is the two-way transmissivity through the canopy, θ is the incidence angle of the SAR signal beam, V_1, V_2 are vegetation descriptors, and A, B are model parameters.

In this study, the vegetation descriptors, V_1 and V_2, are, respectively, 1 and the GAI ($\text{m}^2\,\text{m}^{-2}$) of the maize crop. The GAI is indeed a very suitable descriptor of the canopy since it is an indicator of light interception and thus, indirectly, photosynthesis (Prévot et al., 1993). The GAI was also shown, in Chapter 2, to be the biophysical variable most correlated with backscatter in both horizontal and cross-polarization—while being on par with the others in VV—of all those measured during the BELSAR Campaign.

As for the contribution from the soil to the backscatter, experimental evidence suggests that σ_0^{soil} in decibel (dB) is as a linear function of the volumetric surface soil moisture, V_m ($\text{kg}\,\text{m}^{-3}$) (Ulaby et al., 1978). However, a closer fit was achieved with a linear relationship between σ_0^{soil} in natural units and V_m, hence,

$$\sigma_0^{\text{soil}} = CV_m - D, \tag{3.4}$$

where C, D are model parameters that account for the influence of soil moisture and soil roughness, respectively. The same soil model was used in Hosseini et al. (2015), Hosseini and McNairn (2017), Hosseini et al. (2019), and Mandal et al. (2019). This model implies that the soil roughness is constant throughout the observation period, i.e., the growing season of the crop, which is a reasonable assumption with respect to Belgian agricultural practices concerning maize.

It is important to note that in this study, as in Hosseini et al. (2015), the model parameters are not constrained to make physical sense, which means that the two contributions to the total backscatter, σ_0^{veg} and σ_0^{soil}, can be negative for certain values of the GAI and V_m. This relaxation of the physical constraints of the model therefore represents a departure from radiative transfer theory.

Calibration

The model parameters A, B, C, and D are calibrated via non-linear least squares, which amounts to minimizing the sum of square residuals (SSR),

$$\min_{A,B,C,D\in\mathbb{R}} \sum_{i=0}^{N-1} (\sigma_0^{\text{obs},i} - \sigma_0^{\text{tot},i})^2, \tag{3.5}$$

where N is the number of data points in the calibration set, and $\sigma_0^{\text{obs},i}$ and $\sigma_0^{\text{tot},i}$, $i = 0, 1, \dots, N-1$, are the backscattering coefficients, in natural units, observed and simulated with the model, respectively. This problem is solved numerically by alternating between the basin-hopping algorithm (Wales and Doye, 1997), which is a stepping technique for global optimization, and a truncated Newton method (Nash, 1984), for local minimization, starting from an initial guess (A_0, B_0, C_0, D_0) for the model parameters. As mentioned above, no additional constraints are imposed on this optimization problem.

3.3.2 Backward modeling

Algebraic inversion

After the model is calibrated, it can be algebraically inverted in order to retrieve either the GAI or the volumetric surface soil moisture, V_m, of a maize crop. Hence, an estimate of the green area index,

$$\widehat{\mathrm{GAI}} = -\frac{\cos(\theta)}{2B} \ln\left(\frac{A\cos(\theta) - \sigma_0^{\mathrm{obs}}}{A\cos(\theta) - CV_m + D}\right), \tag{3.6}$$

and an estimate of the volumetric surface soil moisture,

$$\widehat{V_m} = \frac{1}{C}\left(\frac{\sigma_0^{\mathrm{obs}} - A\cos(\theta)(1 - e^{-2B\ \mathrm{GAI}\ \sec(\theta)})}{e^{-2B\ \mathrm{GAI}\ \sec(\theta)}} + D\right), \tag{3.7}$$

can be obtained from a measurement of the backscattering coefficient, σ_0^{obs}, the incidence angle of the SAR signal beam, θ, and V_m or the GAI respectively.

Simultaneous retrieval of green area index and surface soil moisture

The algebraic inversion of the semi-empirical model allows to retrieve either the GAI or the surface soil moisture from SAR data with knowledge of the other variable. However, *in situ* measurements of GAI and surface soil moisture are poorly suited to an operational setting. The use of two polarizations of a multi-polarized SAR measurement can dispense with the necessity to have knowledge of one of the two variables of interest, i.e., GAI and surface soil moisture, to obtain the other. Two WCMs can be calibrated using backscattering coefficients in different polarizations, forming a system of two non-linear equations with two unknowns, $\widehat{\mathrm{GAI}}$ and $\widehat{V_m}$,

$$\begin{cases} \sigma_0^{\mathrm{obs,pq}} = A_{\mathrm{pq}}\ \widehat{\mathrm{GAI}}\ \cos(\theta)\ (1 - e^{-2B_{\mathrm{pq}}\sec(\theta)}) + (C_{\mathrm{pq}}\widehat{V_m} - D_{\mathrm{pq}})\ e^{-2B_{\mathrm{pq}}\sec(\theta)} \\ \sigma_0^{\mathrm{obs,rs}} = A_{\mathrm{rs}}\ \widehat{\mathrm{GAI}}\ \cos(\theta)\ (1 - e^{-2B_{\mathrm{rs}}\sec(\theta)}) + (C_{\mathrm{rs}}\widehat{V_m} - D_{\mathrm{rs}})\ e^{-2B_{\mathrm{rs}}\sec(\theta)} \end{cases} \tag{3.8}$$

where $\sigma_0^{\mathrm{obs,pq}}$ and $\sigma_0^{\mathrm{obs,rs}}$ are the measured backscattering coefficients in the *pq* and *rs* polarizations, and A_{pq}, B_{pq}, C_{pq}, D_{pq}, A_{rs}, B_{rs}, C_{rs}, D_{rs} are the parameters of the two WCMs, with $\mathrm{pq}, \mathrm{rs} \in \{\mathrm{HH}, \mathrm{HV}, \mathrm{VV}\}$, $\mathrm{pq} \neq \mathrm{rs}$, for fully polarimetric data, and $\mathrm{pq} = \mathrm{VH}$, $\mathrm{rs} = \mathrm{VV}$ for dual-polarized data.

The resolution of Equation (3.8) is an ill-posed problem. Several combinations of GAI and V_m can indeed correspond to a same SAR measurement (Bériaux et al., 2015). Inversion techniques aim at finding an approximate solution to the inverse problem by indirectly imposing additional constraints, which are dependent on their specific implementation, on the solution such that it becomes unique, thereby regularizing the problem. Three inversion techniques are explored and reported in this study: (1) an iterative optimization (IO) method (Kelley, 1999); (2) a look-up table (LUT) search; (3) a RF regressor approach (Breiman, 2001).

The IO method consists in finding solutions to Equation (3.8) iteratively from an initial guess of the solution. The Levenberg-Marquardt algorithm (Moré, 1978) is used for this purpose. Since the existence of local minima cannot be excluded for the inverse problem, the method is not guaranteed to return the global minimum of the objective function. The possibility that its approximate solution is a local minimum depends largely on its initial approximation and its stopping criterion. In this paper, the latter specifies that the method stops when the approximate solution or objective value of the last iteration is too close to the ones of the previous iteration, or when a predetermined number of iterations is reached.

The LUT search begins by the generation of a data cube of simulated backscattering coefficients by forward modeling the pair of WCMs in Equation (3.8) with varying values of GAI, V_m and θ. The inversion of a set of backscatter measurements and incidence angles is then performed by searching in the cube the entries that most closely correspond to them according to a criterion, the minimum Euclidean distance in this paper, and returning the GAI and soil moisture values from which they were simulated. In addition to the proximity criterion, the returned approximate solution therefore depends on the step size between the table entries and the criterion for choosing between multiple entries with identical proximity. In this study, if two inputs have the same distance to the observed radar data, the returned GAI and soil moisture values correspond to the entry for which their value as well as that of the incidence angle are the smallest.

Finally, the RF regressor consists in training a RF on the data contained in the LUT to make up for the low number of data observed in the field, and then using the trained model to produce estimates of the variables of interest from SAR measurements. The returned solution is computed as the mean of the predicted values of the variables of interest by the decision trees in the forest. As with the two previous inversion techniques, the choice of the hyperparameters, quantitative and categorical, of the method has an impact on the approximate solution that is found (Probst et al., 2019). These hyperparameters can be the object of an optimization procedure, also called tuning, by various methods such as a grid search. The use of bootstrapping also introduces a random element in the method. It is therefore expected that the three inversion strategies listed above will produce different results between them and depending on the values of their hyperparameters. The comparison between these methods in this paper is therefore not absolute but relative to the problem presented and the experimental data collected.

3.3.3 Experimental design

The main purpose of this study is to evaluate the performance of an algorithm using a semi-empirical model that is a relaxed version of the WCM for the simultaneous estimation of GAI and surface soil moisture in maize fields from radar data only. For this purpose, several methods, i.e., IO, LUT search, and RF regressor, are implemented and tested with the L- and C-band multi-polarized SAR, vegetation, and soil data from the BELSAR campaign. The results obtained are then compared to those that the semi-empirical can deliver when one of the two variables of interest is known. A flowchart providing a summary of the different steps in the methodology of this study can be found in Figure 3.5.

3.3.4 Validation and comparison between inversion methods

Since the number of data that are available is relatively small, the goodness-of-fit and retrieval performance of the models are evaluated through a leave-one-out cross-validation (LOOCV) scheme. Let M be the number of data points in the dataset. At each of the M iterations of the scheme, the model is trained on $M - 1$ data points. The remaining data point is then used to evaluate the goodness-of-fit of the model, by simulating the backscatter of the crop with the true values of GAI, V_m, and θ of the data point, as well as the accuracy of the model predictions, by estimating the GAI and V_m from their corresponding radar measure-

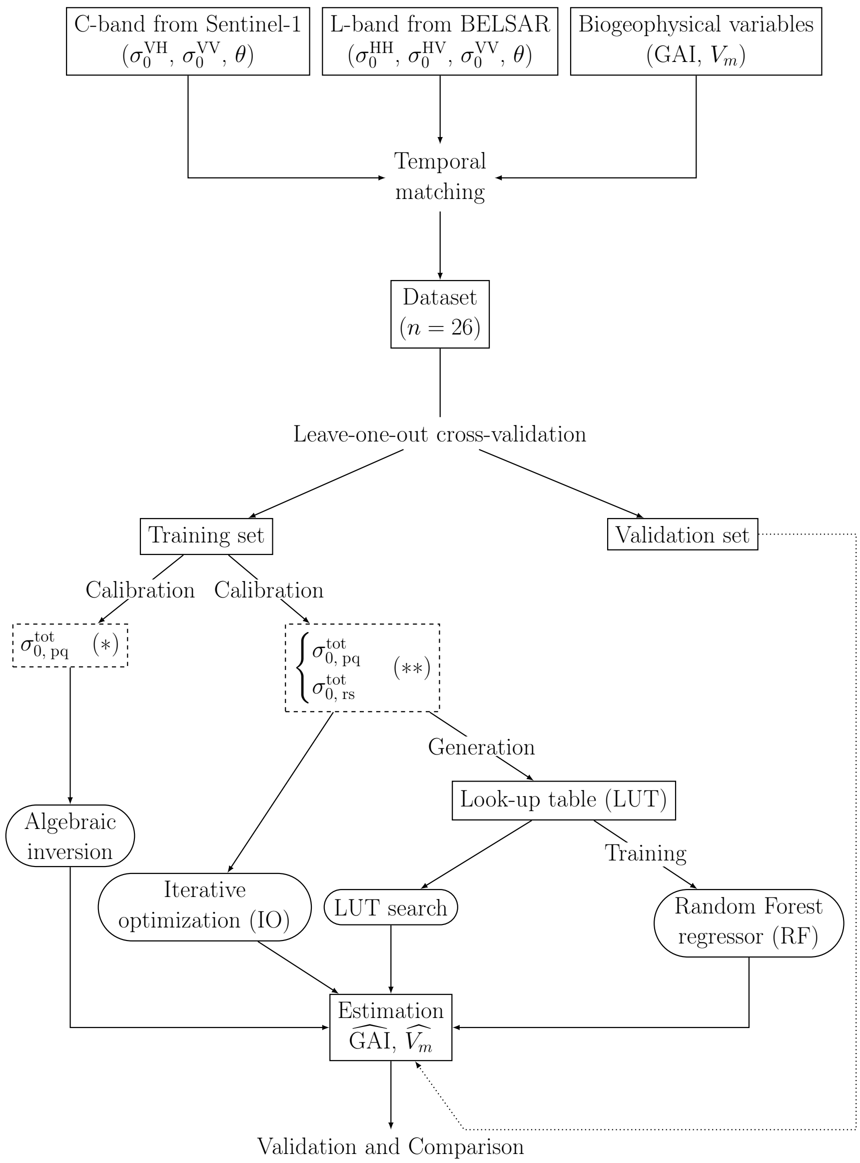

$(*)$ L-band: $\text{pq} \in \{\text{HH}, \text{HV}, \text{VV}\}$;
C-band: $\text{pq} \in \{\text{VH}, \text{VV}\}$

$(**)$ L-band: $\text{pq}, \text{rs} \in \{\text{HH}, \text{HV}, \text{VV}\}$, $\text{pq} \neq \text{rs}$;
C-band: $\text{pq} = \text{VH}$, $\text{rs} = \text{VV}$

Figure 3.5: Flowchart of the experimental design.

ments. The aggregation of these M evaluations through appropriate metrics then enables to evaluate the estimation performance of the different models and the ability of the semi-empirical model to simulate the backscatter of crops. The metrics used in this study to quantify the difference between estimated and observed values are Pearson's correlation coefficient, R, the RMSE, and the relative RMSE (RRMSE). The RRMSE is defined in this study as the RMSE divided by the difference between the maximum and minimum values of the observations. Their definitions can be found in Table 3.3. This normalization facilitates the comparison between data that have different ranges of values, such as the backscattering coefficients in co- and cross-polarization, as is apparent in Figure 3.2 and Figure 3.3. For this reason, it is used in this study to evaluate the goodness-of-fit of the semi-empirical model, while the GAI and V_m estimates are evaluated with the RMSE to ease the comparison with state-of-the-art retrieval methods, as well as offer a more straightforward understanding of the real-world applicability of the investigated methods.

3.4 Results

3.4.1 Sensitivity analysis

The potential of the C-band radar data from S1 for maize monitoring has already been established and quantified in several studies, e.g. (Veloso et al., 2017; Vreugdenhil et al., 2018; Khabbazan et al., 2019). For this reason, only the sensitivity of the L-band backscatter measurements from the BELSAR dataset to variations of the GAI, the volumetric surface soil moisture under the canopy, V_m, and incidence angle, θ, will be assessed in this study. It will be carried out in two ways. First using linear and linear-log regression models with the measured backscattering coefficients, as in Vreugdenhil et al. (2018) and Wiseman et al. (2014). Linear-log regression models are linear regression models computed using the logarithm of the independent variable. Second, by simulating backscattering coefficients with the semi-empirical model described in Section 3.3.1 and observing their response to variations of GAI, V_m, and θ.

Table 3.3: Error metrics used to measure model performance, where $\hat{y}_i$, $i = 1,\ldots,N$, are the model estimations, y_i, $i = 1,\ldots,N$, the observations, and $\bar{\hat{y}}$ and $\bar{y}$ their arithmetic means.

Error metric	Symbol	Definition
Correlation coefficient	R	$\dfrac{\sum_{i=1}^{N}(y_i-\bar{y}_i)(\hat{y}_i-\bar{\hat{y}}_i)}{\sqrt{\sum_{i=1}^{N}(y_i-\bar{y}_i)^2\sum_{i=1}^{N}(\hat{y}_i-\bar{\hat{y}}_i)^2}}$
Root-mean-square error	$RMSE$	$\sqrt{\dfrac{1}{N}\sum_{i=1}^{N}(y_i-\hat{y}_i)^2}$
Relative RMSE	$RRMSE$	$\dfrac{\sqrt{\frac{1}{N}\sum_{i=1}^{N}(y_i-\hat{y}_i)^2}}{\max_{i\in\{1,\ldots,N\}} y_i - \min_{i\in\{1,\ldots,N\}} y_i}$

Sensitivity of L-band σ_0 to GAI and V_m

The linear and linear-log regression lines, depicted in Figure 3.6, suggest through their coefficients of determinations, R^2_{lin} and $R^2_{lin\text{-}log}$, that the L-band backscattering coefficients σ_0 from BELSAR are moderately sensitive to the GAI, especially in HV, with $R^2_{lin} = 0.60$ and $R^2_{lin\text{-}log} = 0.72$, and in VV, with $R^2_{lin} = 0.62$ and $R^2_{lin\text{-}log} = 0.69$, but have no sensitivity to the surface soil moisture under the canopy, with $R^2_{lin} = 0.01$ and $R^2_{lin\text{-}log} = 0.01$ in both HV and VV. This finding is discussed in more detail in Chapter 2, where the GAI is reported as the crop biophysical variable that is the most linearly correlated with the L-band backscattering coefficients used in this work, among all the crop variables measured *in situ* during the BELSAR campaign, i.e., GAI, plant height, wet and dry biomass, and vegetation water content which are reported in Table 3.2.

Sensitivity of the semi-empirical model to GAI, V_m, and θ

The sensitivity of the semi-empirical model, and of the L-band backscatter measurements through it, to variations of GAI, V_m, and θ is investigated by calibrating the model with the entire BELSAR dataset ($n = 26$) for each polarization, and then forward modeling backscattering coeffi-

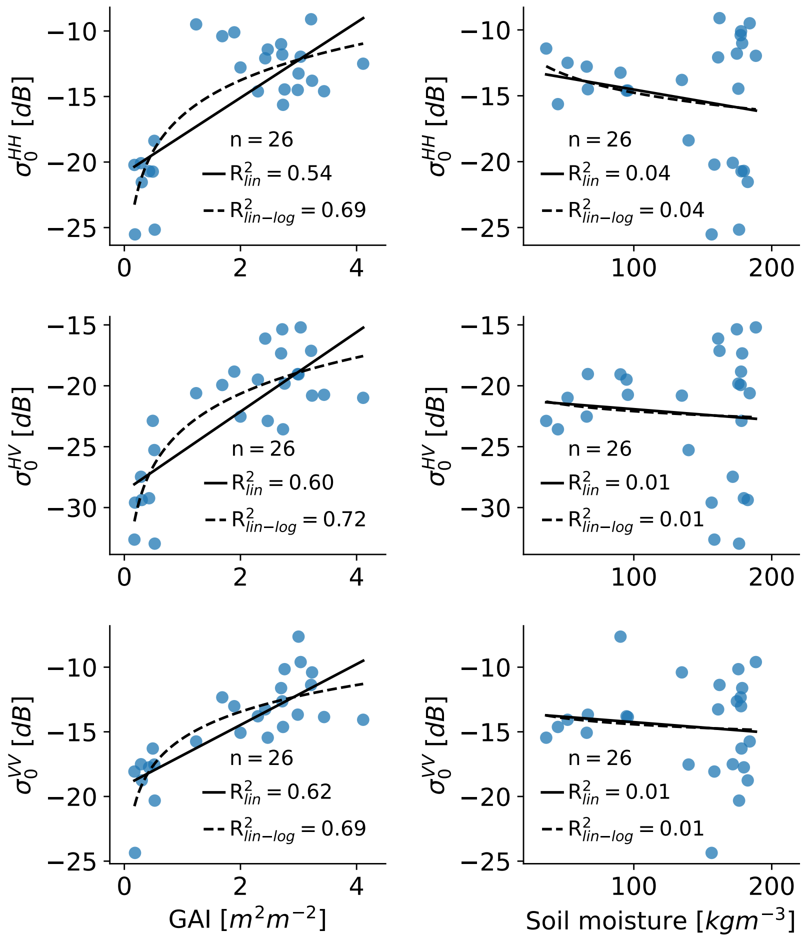

Figure 3.6: Scatter plots, as well as linear and linear-log regressions lines, of the volumetric surface soil moisture and GAI as a function of the backscattering coefficient σ_0 in (**top**) HH, (**middle**) HV, and (**bottom**) VV polarization.

cients with varying values of the three variables on which it depends.

The values of the parameters of the model calibrated with HH, HV, and VV polarized L-band data from BELSAR are listed in Table 3.4. Note that the calibration procedure for the model is based on the minimization of the sum of its squared residuals, a non-convex objective.

Table 3.4: Values of the parameters of the semi-empirical calibrated with all available *in situ* measurements of GAI and volumetric surface soil moisture, V_m, and their corresponding L-band SAR backscattering coefficients and incidence angles.

Pol	A	B	C	D
HH	1.35×10^{-1}	1.73×10^{-1}	7.88×10^{-4}	1.32×10^{-1}
HV	-3.24×10^{-2}	-6.58×10^{-2}	6.68×10^{-5}	9.74×10^{-3}
VV	-4.44×10^{-3}	-1.60×10^{-1}	7.48×10^{-5}	-4.58×10^{-3}

While convergence to a global minimum cannot be guaranteed for this optimization problem, the minimization procedure, starting from an initial guess for values of the model parameters (A, B, C, and D), was found to be fairly insensitive to this initial choice. Indeed, a range of initial values was tested for the start of the iterative minimization algorithm, and it was found that relatively large perturbations of these initial guesses have a negligible impact on the cross-validation errors made by the model. For this reason, all the calibration procedures of the semi-empirical model in this study have $(A_0, B_0, C_0, D_0) = (1, 1, 1, 1)$ as initial guess.

The fit of the semi-empirical model with the parameter values reported in Table 3.4 is similar in terms of RMSE for backscattering coefficients in HV and VV, with values of 0.16 and 0.15 respectively. However, the correlation coefficient in HV is higher than in VV, i.e., 0.83 against 0.72. The goodness-of-fit of the model is significantly worse in HH, with an R of 0.65 and an RRMSE of 0.22.

The backscattering coefficients simulations performed with the semi-empirical model calibrated with the parameter values listed in Table 3.4 for various values of GAI, V_m, and θ, are reported in Figure 3.7 and Figure 3.8. These simulations provide insight on the sensitivity of the model, and indirectly the L-band SAR backscatter, to these variables. Variations in the value of the incidence angle have little overall effect on the sensitivity of the model simulations to variations in GAI or surface soil moisture values. Only the response of the model in VV is slightly affected by variations of θ, and only at high GAI values, i.e., around $4\,\mathrm{m}^2\,\mathrm{m}^{-2}$. Besides, the simulated backscattering coefficients in VV do

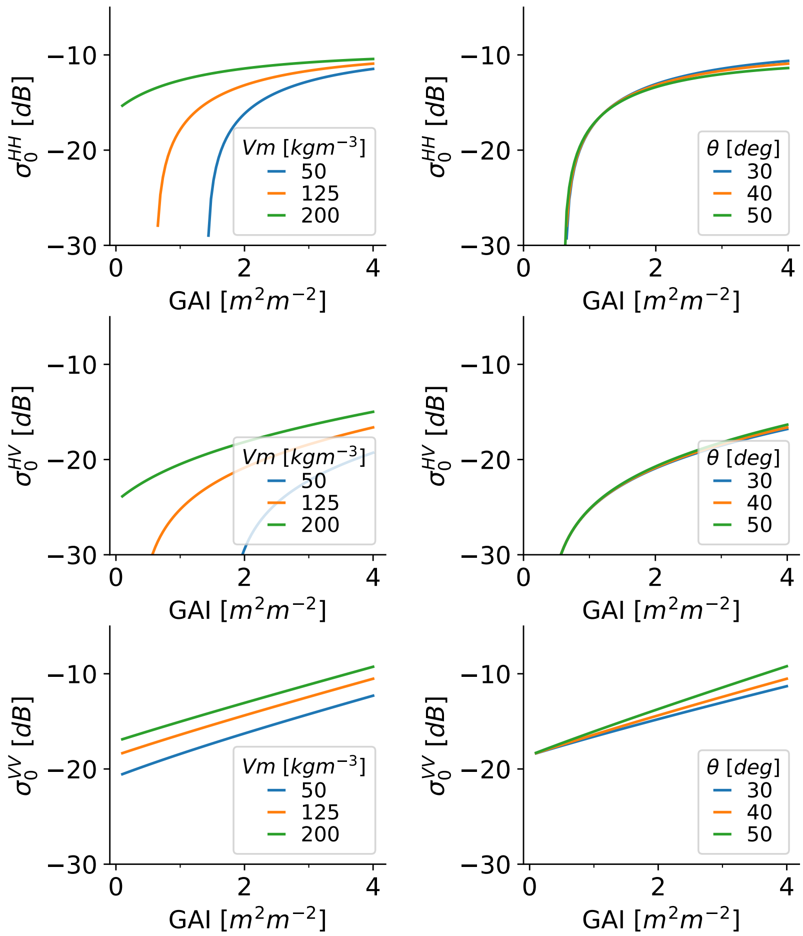

Figure 3.7: Backscattering coefficient simulations σ_0 in polarization (**top**) HH, (**middle**) HV, and (**bottom**) VV as a function of GAI (**left**) for multiple values of volumetric surface soil moisture, V_m, with the incidence angle $\theta = 40°$, and (**right**) for multiple incidence angles, with $V_m = 125\,\mathrm{kg\,m^{-3}}$.

not seem to converge, or saturate, with increasing GAI and are quite sensitive to variations in its value. On the other hand, they do not appear to be very sensitive to variations of the surface soil moisture value, V_m. The simulations in HV seem to be the most balanced, i.e.,

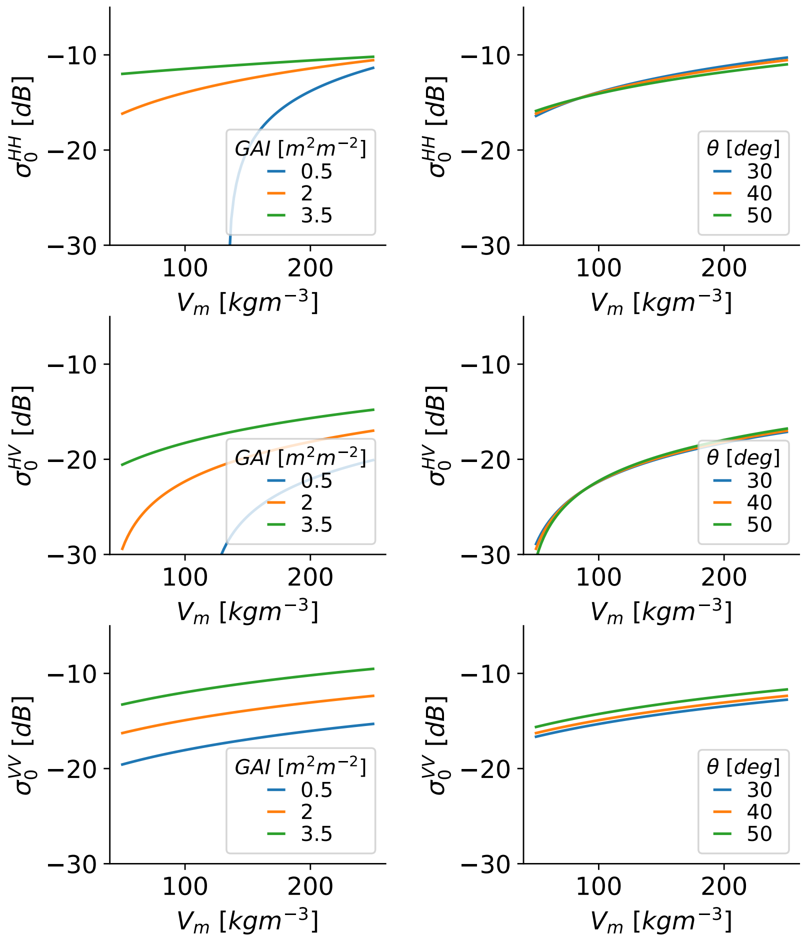

Figure 3.8: Backscattering coefficient simulations σ_0 in polarization (**top**) HH, (**middle**) HV, and (**bottom**) VV as a function of volumetric surface soil moisture, V_m, (**left**) for multiple values of GAI with the incidence angle $\theta = 40°$, and (**right**) for multiple incidence angles with $\text{GAI} = 2\,\text{m}^2\,\text{m}^{-2}$.

they are sensitive to changes in GAI and V_m, even at higher values, although this sensitivity decreases as GAI and V_m values increase. They are also more sensitive than those in VV to the surface soil moisture under the canopy. In general, the GAI has a significant impact on the sensitivity of the model to the surface soil moisture. This phenomenon is expected; the more developed the crop, the less capacity the signal has to penetrate it to interact with the soil. Finally, simulations in HH already saturate for moderately high values of GAI, at around $2\,\mathrm{m}^2\,\mathrm{m}^{-2}$, and are not very sensitive to soil moisture except at the early stages of crop growth.

Based on this sensitivity assessment, HV seems to be the most appropriate polarization for estimating GAI and V_m. It is then closely followed by VV, while HH appears insensitive to these biogeophysical variables in comparison.

3.4.2 Algebraic inversion of the model

The retrieval of either the GAI or the volumetric surface soil moisture, V_m, is performed through the algebraic inversion of the semi-empirical model described in Section 3.3.2. This method requires the knowledge, or at least an estimate, of V_m to retrieve the GAI of a maize crop, and conversely.

The quality of the fit between the measured backscattering coefficients and those simulated with the semi-empirical model, for each polarization, is depicted in Figure 3.9 and Figure 3.11 for the L-band from BELSAR and C-band from S1, respectively. The coefficients in the figures are expressed in natural power units rather than decibels, even though the latter are more frequently encountered in the field of radar remote sensing. This is tied to the fact that the model is calibrated in these units and that the simulations of the semi-empirical model are not constrained in such way that they would have to be physically consistent, i.e., they can have negative values, as mentioned in Section 3.3.1. This is indeed the case for the simulations in HH, in Figure 3.9a, therefore the calibration results cannot be reported in decibels without omitting negative values. These physically impossible results are the consequence of the relaxation of the physical constraints of the WCM.

In L-band, the fit of the simulations in HH, with a correlation coefficient of 0.47 and an RRMSE of 0.26, is significantly worse than for HV, with an R of 0.75 and an RRMSE of 0.18. In VV, the errors are highly influenced by only two data points that penalize the correlation coefficient and RRMSE, with values of 0.46 and 0.21 respectively. Without these outliers, given the tight distribution of the points along the 1:1

line, better results than in HV could be expected.

In C-band, despite errors in line with those obtained with L-band data, with correlation coefficients of 0.53 and 0.61, and rRMSEs of 0.21 and 0.22, for VH and VV, respectively, the model simulations appear to be less faithful to the backscattering coefficients measurements than those obtained with L-band data, as attested by the distribution of the data points in the scatter plots in Figure 3.11.

The estimates of GAI and V_m obtained through the algebraic inversion of the semi-empirical model, in a LOOCV scheme, are shown in Figure 3.10 for the L-band data, and in Figure 3.12 for the C-band data, and the estimation errors for each frequency band are reported in Table 3.5a and Table 3.5b, respectively.

The most accurate GAI estimates obtained using this method are derived from L-band SAR data in VV, with an R of 0.87 and an RMSE of $0.68\,\mathrm{m^2\,m^{-2}}$. The vertical co-polarization, although leading to better GAI retrieval accuracies than HV, with an R of 0.825 and an RMSE of $0.75\,\mathrm{m^2\,m^{-2}}$, is on the other hand less suitable than the latter for the estimation of the surface soil moisture, with an R of 0.60 and an RMSE of $54.73\,\mathrm{kg\,m^{-3}}$ for HV, and an R of 0.39 and an RMSE of $81.25\,\mathrm{kg\,m^{-3}}$ for VV. As for HH, its GAI and V_m retrieval accuracies are very low, with R values of 0.48 and 0.37 and RMSEs of $1.41\,\mathrm{m^2\,m^{-2}}$ and $81.53\,\mathrm{kg\,m^{-3}}$ respectively.

It is important to note, however, that threshold values were set to limit the values of the GAI estimates to a range between 0 and $4\,\mathrm{m^2\,m^{-2}}$, as in Bériaux et al. (2015), and V_m estimates between 0 and $250\,\mathrm{kg\,m^{-3}}$. These extreme values used as prior information artificially increase the precision of the model estimates since they limit its least physically plausible outputs.

3.4.3 Simultaneous retrieval of GAI and surface soil moisture

The simultaneous retrieval of both GAI and V_m with dual-polarized SAR data (HH and HV, HH and VV, or HV and VV, for the L-band data, and VH and VV for the C-band data) is performed using three inversion strategies: the IO method, the LUT search, and the RF regression. These are described in Section 3.3.2.

For the IO method, the initial values for the GAI and V_m required by

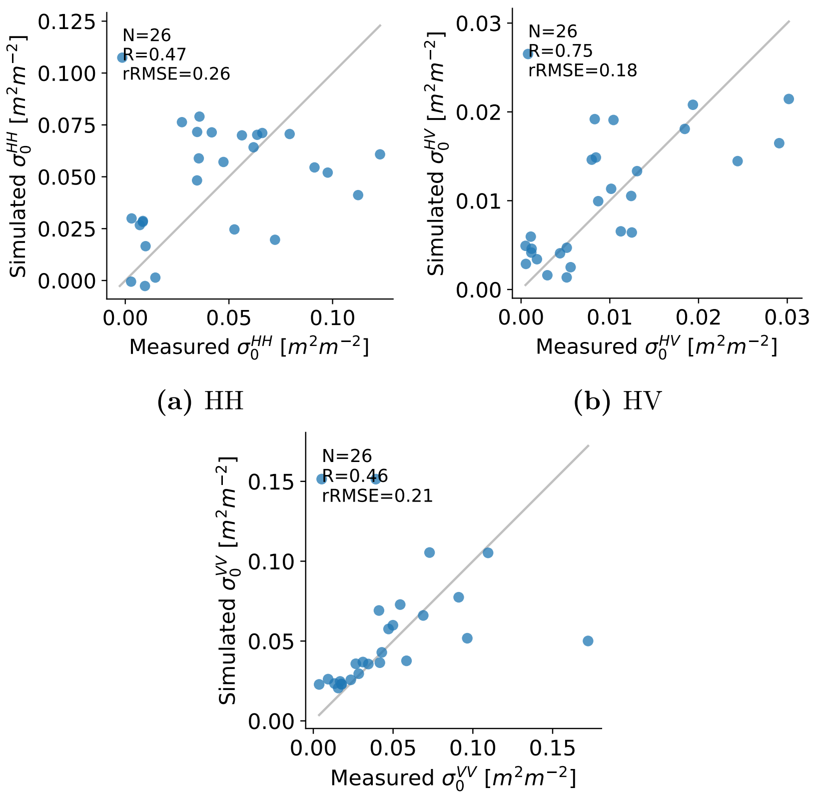

(a) HH

(b) HV

(c) VV

Figure 3.9: Results from the leave-one-out cross-validation for the calibration of the semi-empirical model with L-band data.

the Levenberg-Marquardt algorithm were set at $2\,\mathrm{m^2\,m^{-2}}$ and $125\,\mathrm{kg\,m^{-3}}$. With regard to the LUT search and RF regressor, the pairs of backscattering coefficients forming the data cube were simulated from a grid of GAI, V_m, and θ values such that

$$\begin{aligned}
\mathrm{GAI} &= \{x : x = 0.05n,\ n \in \{0, 1, \ldots, 80\}\},\\
V_m &= \{x : x = 0.5n,\ n \in \{0, 1, \ldots, 500\}\},\\
\theta &= \{x : x = 20 + 0.5n,\ n \in \{0, 1, \ldots, 80\}\}.
\end{aligned}$$

A grid search resulted in the number and maximum depth of the RF

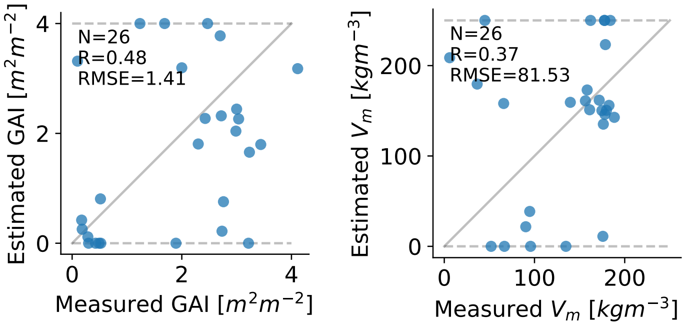

(a) HH

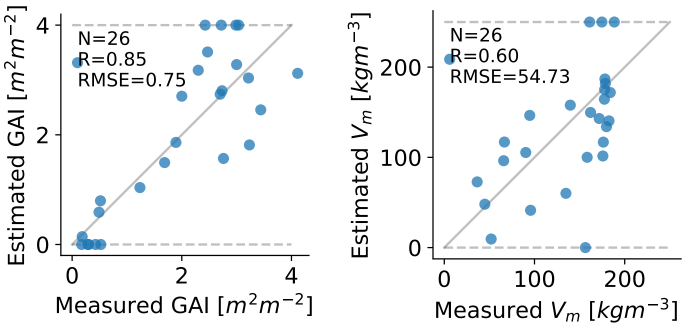

(b) HV

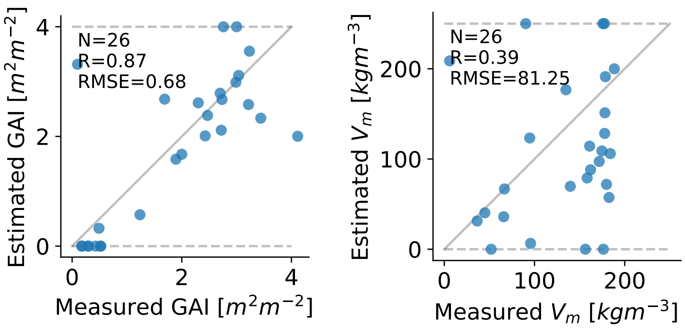

(c) VV

Figure 3.10: Results from the leave-one-out cross-validation for the retrieval of either maize (**left**) GAI or (**right**) volumetric surface soil moisture, V_m, using the algebraic inversion of the semi-empirical model with L-band data.

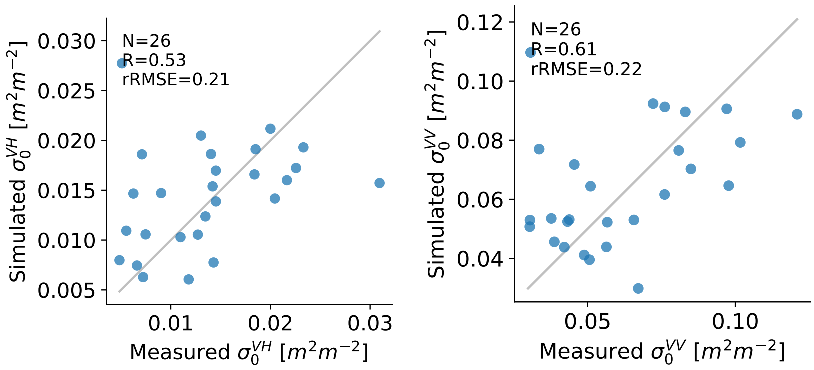

(a) VH **(b)** VV

Figure 3.11: Results from the leave-one-out cross-validation for the calibration of the semi-empirical model with C-band data.

regressor trees being set at 100 and 4 respectively.

Since the semi-empirical models are calibrated separately using distinct polarizations, the calibration results for this retrieval method are the same as the ones for the one relying on the algebraic inversion of the model. They are reported in Figure 3.9 and Figure 3.11 for the L- and C-band data, respectively. As for the validation results from the LOOCV for each available frequency band and polarization pair, they are reported in Table 3.6.

In L-band, of the three inversion strategies, the RF regressor with the polarization pair HV and VV resulted in the most accurate estimates for both GAI and volumetric surface soil moisture, with an R of 0.79 and an RMSE of $0.77\,\mathrm{m^2\,m^{-2}}$, and an R of 0.20 and an RMSE of $70.60\,\mathrm{kg\,m^{-3}}$, respectively. These validation results, from the LOOCV with the RF regressor, as well those obtained with the other two polarization pairs, are depicted in Figure 3.13.

Of the three polarization pairs in this frequency band, the pair HV and VV provides the best GAI estimates for each inversion strategy. This finding does not hold for V_m, however, since the pair HH and HV yields a lower RMSE than the other pairs with the IO method, with a value of $80.75\,\mathrm{kg\,m^{-3}}$, although these errors remain much larger than those obtained via the RF regressor. Furthermore, for each polarization

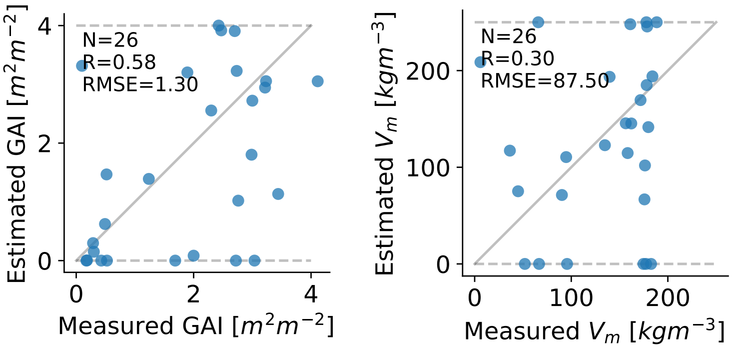

(a) VH

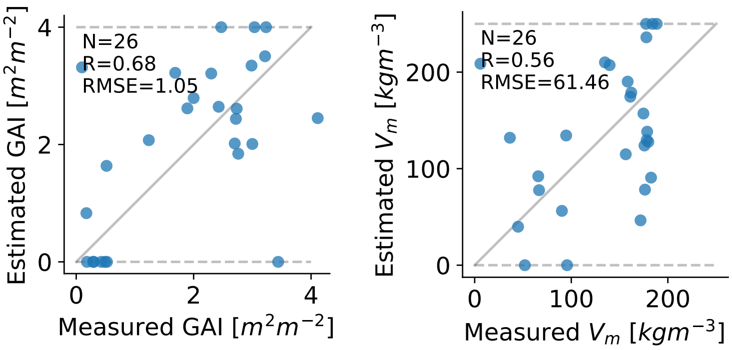

(b) VV

Figure 3.12: Results from the leave-one-out cross-validation for the retrieval of either maize (**left**) GAI or (**right**) volumetric surface soil moisture, V_m, using the algebraic inversion of the semi-empirical model with C-band data.

pair, the GAI estimates obtained with the RF regressor are better than those of the other two inversion strategies, which is consistent with the findings of Mandal et al. (2019) in their investigation into multiple inversion strategies for the estimation of the GAI in maize crops using the semi-empirical model with C-band data.

For the C-band data with the only available polarization pair, VH and VV, the strategy resulting in the most accurate GAI and V_m estimates is the RF regressor, as with the L-band, with correlation coefficients of

Table 3.5: Results from the leave-one-out cross-validation for the retrieval of either GAI or volumetric surface soil moisture, V_m, in maize fields from (**a**) L- and (**b**) C-band backscattering measurements ($n = 26$) with the algebraic inversion of the semi-empirical model.

(**a**) L-band

Polarization	**GAI** $[\mathrm{m^2\,m^{-2}}]$		$\mathbf{V_m}$ $[\mathrm{kg\,m^{-3}}]$	
	R	**RMSE**	**R**	**RMSE**
HH	0.48	1.41	0.37	81.53
HV	0.825	0.75	0.60	54.73
VV	0.87	0.68	0.39	81.25

(**b**) C-band

Polarization	**GAI** $[\mathrm{m^2\,m^{-2}}]$		$\mathbf{V_m}$ $[\mathrm{kg\,m^{-3}}]$	
	R	**RMSE**	**R**	**RMSE**
VH	0.58	1.30	0.30	87.50
VV	0.68	1.05	0.56	61.46

0.65 and 0.29, and RMSEs of $0.98\,\mathrm{m^2\,m^{-2}}$ and $69.34\,\mathrm{kg\,m^{-3}}$.

Based on these observations, the L-band seems therefore better suited for the estimation of the GAI with this method, and the C-band for the estimation of V_m, although results for the latter are quite close between the two frequency bands. However, this observation must be qualified. Concerning V_m, neither the estimates obtained from L-band data nor those obtained from C-band data seem to be usable for accurate soil moisture monitoring based on the loose distributions around the 1:1 line visible in Figure 3.13 and Figure 3.14. As for the GAI, there is a clear overestimation of its value at the beginning of the growing season for both frequency bands. However, this may be due to an imbalance in the calibration dataset.

Finally, this method, which consists of simultaneously estimating the GAI and volumetric surface soil moisture of a maize crop, thus provides similar, although slightly less accurate, results than the method based on the algebraic inversion of the semi-empirical model. However, the former has the decisive advantage, in an operational context, that it only requires backscattering measurements in two polarizations and the incidence angle of the SAR beam, and no ancillary information on either one of the variables of interest to provide estimates of the other. Note as well that for none of these strategies the thresholds imposed for the estimates of GAI and V_m were reached, unlike for the method based on the algebraic inversion of the semi-empirical model.

3.5 Discussion

The sensitivity assessment of the L-band data, based on a regression analysis and simulations of the backscatter of the maize crop by forward modeling with the semi-empirical model based on a relaxed WCM, demonstrated the sensitivity of the L-band backscattering measurements to variations of the GAI in those crops. However, it also revealed the significantly lower sensitivity of the SAR measurements to the volumetric surface soil moisture under the canopy, possibly due to drought conditions, which is also apparent in the estimation results obtained from both retrieval methods, i.e., the algebraic inversion of the semi-empirical model and the joint estimation of both variables from radar backscatter measurements in two distinct polarizations.

The algebraic inversion of the model, the results of which are reported in Section 3.4.2, consists in finding one of the two variables of interest using the other as well as backscattering measurements in a single polarization and the incidence angle of the SAR beam. This method for either GAI or soil moisture retrieval provided more accurate results with SAR backscatter measurements in L-band rather than in C-band, especially for the GAI retrieval. Furthermore, for this purpose, the vertical co-polarization, VV, in L-band was the most adequate, but only slightly better than HV. For the estimation of the soil moisture under the canopy, on the other hand, while accuracies were low for all frequency bands and polarizations, the cross-polarization in L-band yielded the best results, while the horizontal co-polarization, HH, in L-band did not provide satisfactory results for either variable, as the sensitivity assessment prefigured. These findings are in agreement with the study of Tronquo et al. (2022) who also exploited the BELSAR dataset and re-

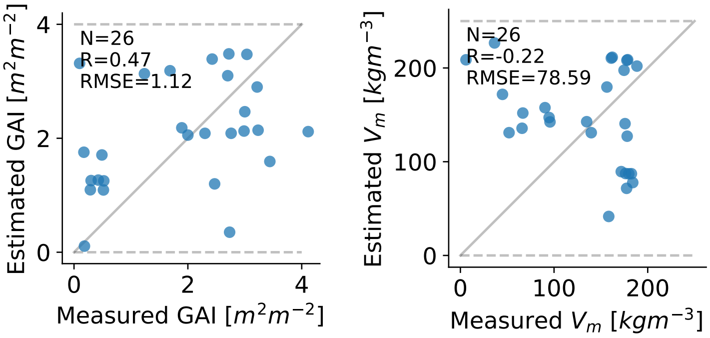

(a) HH and HV

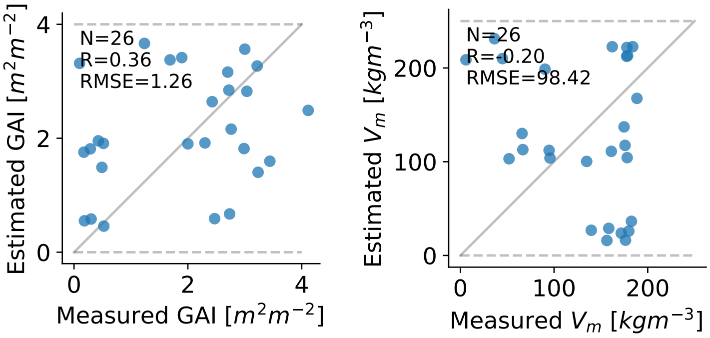

(b) HH and VV

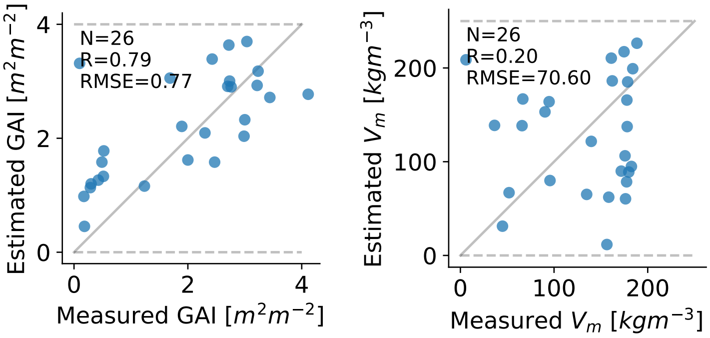

(c) HV and VV

Figure 3.13: Results from the leave-one-out cross-validation for the simultaneous retrieval of maize (**left**) GAI or (**right**) volumetric surface soil moisture, V_m, using a RF regressor.

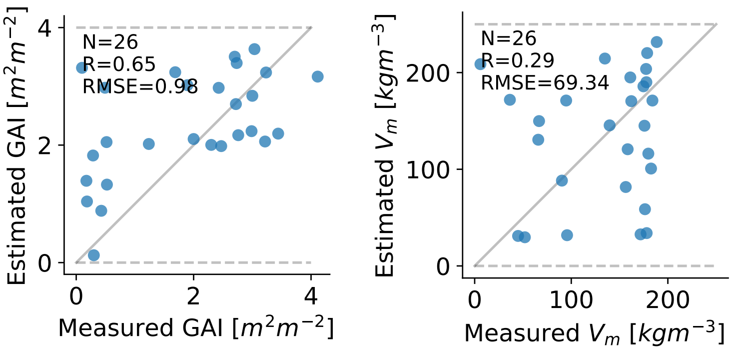

Figure 3.14: Results from the leave-one-out cross-validation for the simultaneous retrieval of maize (**left**) GAI or (**right**) volumetric surface soil moisture, V_m, using a RF regressor with C-band data.

ported that the most accurate soil moisture retrieval results over bare soils were found for VH and VV polarization. As for the C-band, finally, the cross-polarization, VH, provided more accurate estimates of both GAI and surface soil moisture than VV.

The simultaneous retrieval method, the results of which are reported in Section 3.4.3, dispensed with the need for ancillary data altogether and allowed the joint estimation of the two variables of interest simultaneously from dual-polarized SAR measurements and their incidence angle alone. Relatively accurate GAI estimates were obtained with a strategy consisting in training a RF regressor with data simulated by a pair semi-empirical models fitted on dual-polarized radar data. However, as with the first method, the accuracy of the surface soil moisture estimates obtained did not prove adequate enough for its monitoring, unlike the GAI estimates. The best accuracies for GAI retrieval with this method were obtained with L-band data in HV and VV polarizations, and the estimates derived from the C-band data from S1 were not as good as those obtained from the L-band data from BELSAR. This second method did not provide GAI estimates as accurate as the previous one with the L-band data, though they were still fairly similar. It was the opposite for the C-band data. The similarity between the results of the first and second methods, as well as their accuracy, suggest

Table 3.6: Results from the leave-one-out cross-validation for the simultaneous retrieval of GAI and volumetric surface soil moisture, V_m, in maize fields from (**a**) L- and (**b**) C-band backscattering measurements ($n = 26$) with different inversion strategies for the semi-empirical model: the iterative optimization (IO), the look-up table (LUT) search, and the Random Forest (RF) regressor.

(**a**) L-band

Method	**Polarizations**	**GAI** [$m^2\,m^{-2}$]		$\mathbf{V_m}$ [$kg\,m^{-3}$]	
		R	**RMSE**	**R**	**RMSE**
IO	HH and HV	0.32	1.46	0.21	80.75
	HH and VV	0.17	1.49	−0.36	127.28
	HV and VV	0.69	1.16	0.28	92.43
LUT	HH and HV	0.10	1.60	−0.25	89.65
	HH and VV	0.43	1.26	−0.30	118.16
	HV and VV	0.76	1.00	0.14	82.23
RF	HH and HV	0.47	1.12	−0.22	78.59
	HH and VV	0.36	1.26	0.20	98.42
	HV and VV	0.79	0.77	0.20	70.60

(**b**) C-band

Method	**Polarizations**	**GAI** [$m^2\,m^{-2}$]		$\mathbf{V_m}$ [$kg\,m^{-3}$]	
		R	**RMSE**	**R**	**RMSE**
IO	VH and VV	0.59	1.27	0.16	87.80
LUT	VH and VV	0.54	1.22	0.21	81.15
RF	VH and VV	0.65	0.98	0.29	69.34

that, under the specific conditions of the BELSAR campaign, knowledge of the volumetric surface soil moisture does not provide a substantial improvement in accuracy for the estimation of the GAI of maize crops using the model with dual-polarized radar data.

The results show that the proposed semi-empirical model, based on a relaxation of the WCM, is simple and straightforward to implement and operate that already generalizes well from a limited number of training data (Hosseini et al., 2021), although its calibration and estimation capabilities are very dependent on them, as already mentioned about the WCM in Bériaux et al. (2015), causing it not to transfer well. Furthermore, it produced relatively accurate results—as compared to other state-of-the-art GAI estimation methods, e.g. (Delloye et al., 2018; Yu et al., 2020; Peng et al., 2021)—for the monitoring of maize crops through their GAI, whether with ancillary information on surface soil moisture or only with radar data provided that two polarization channels are available.

In view of the results reported for its retrieval, monitoring the surface soil moisture under the canopy in maize fields is not possible with the model described in Section 3.3.1. Several hypotheses can explain the relative insensitivity of this model to soil moisture variations. The model for the soil contribution to the total backscatter suggested by Ulaby et al. (1978), which depends linearly on volumetric surface soil moisture, might not be valid for the soil moisture conditions encountered, i.e., very dry soils and a very narrow range of surface moisture values due to an exceptionally dry season. The empirical Oh model (Oh et al., 1992) or the physics-based Integral Equation Model (IEM) (Fung et al., 1992; Fung, 1994) and Advanced Integral Equation Model (AIEM) (Chen et al., 2003; Wu and Chen, 2004) could be used as an alternative to it for relating soil properties to microwave scattering. These models require an accurate description of the surface roughness, however, and its parameterization from field measurements is known to be problematic. This issue was addressed by Tronquo et al. (2022) who proposed a method based on effective roughness modeling, whereby roughness parameters are calibrated based on backscatter observations, which can then be used for soil moisture retrieval. This approach could be implemented in the model framework in order to better reflect the actual soil contribution to the total backscatter. Another hypothesis explaining the insensitivity of the model to soil moisture, invokes the attenuation of the signal by the already well-developed canopy as early as the second acquisition, on June 21 (F2), although it seems less likely in view of the penetration ability of the L-band (El Hajj et al., 2018). The preponderance of double-bounce phenomena in the canopy that are not taken into account by the WCM,

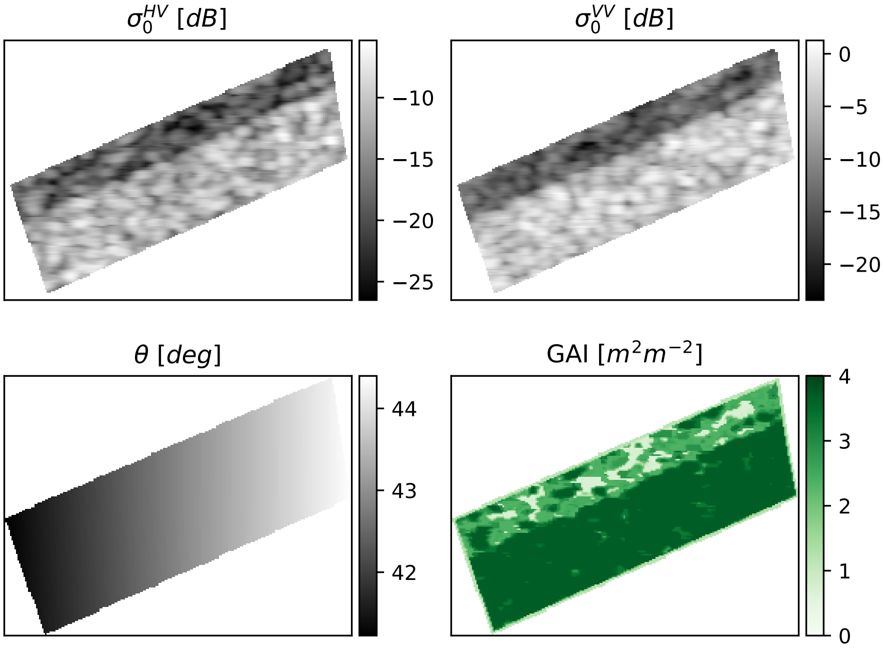

Figure 3.15: GAI map of a maize field, in which *in situ* data were collected, produced using a RF regressor trained with L-band backscattering coefficients σ_0 in HV and VV polarizations acquired on August 26 (F4). To reduce speckle, a 5×5 boxcar filter was applied on the SAR images prior to GAI retrieval.

on which the semi-empirical model used here is based, could also explain the poor sensitivity of the model. Or finally, a combination of these different factors could be the cause of the inaccuracy of the results.

The accuracy of the GAI estimates obtained with the algebraic inversion of the model and the simultaneous estimation of the two variables is encouraging. As expected for high biomass crops, the L-band performs significantly better than the C-band in this respect. Only the HH polarization does not yield the same satisfactory results for the GAI retrieval. This might be due to an effect of the orientation of the maize rows relative to the SAR signal beam, which is much greater in HH than in HV or VV, as shown in Chapter 2, and which was disregarded in this study, although the orientation of the maize rows is known for the fields con-

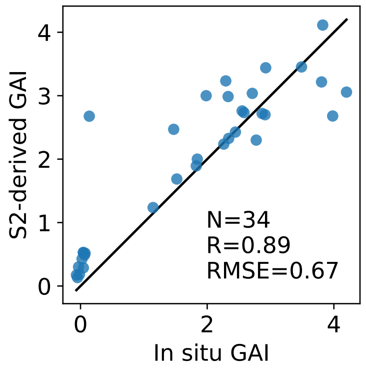

Figure 3.16: Comparison of the GAI retrieved from Sentinel-2 images and *in situ*.

sidered. The reason for this omission is that the WCM is not designed to account for it explicitly, and because the very small number of fields available did not allow to group them according to the orientation of their rows to distinguish their effect. The results are otherwise getting close to, though remaining less accurate than, those that can be expected from remote sensing methods exploiting optical data. For example, the results shown in Figure 3.16 demonstrate that the method developed by Delloye et al. (2018) for GAI retrieval from Sentinel-2 (S2) data is truer to GAI measured *in situ*, with an R of 0.89 and an RMSE of 0.67. The use of radar-only data, however, has a significant advantage over them in the presence of cloud cover, which is frequent during the growing season, and especially at its end, in the AOI. The GAI map in Figure 3.15 is an example of the relevance of such techniques. It reveals that harvesting has only begun in the northern part of the field, while the rest of the field is still vegetated, at a time when cloud cover is almost persistent.

3.6 Conclusion

A relaxed version of the WCM was used in this study for the simultaneous estimation of the GAI of maize crops and the surface soil moisture under their canopy from dual-polarized SAR data in C- and L-band. Accurate GAI estimates were obtained using a RF regressor to invert a pair of semi-empirical models calibrated with SAR data in cross-polarization and vertical co-polarization in both L- and C-band, with correlation coefficients of 0.79 and 0.65 and RMSEs of $0.77\,\mathrm{m}^2\,\mathrm{m}^{-2}$ and $0.98\,\mathrm{m}^2\,\mathrm{m}^{-2}$ respectively. However, the method was shown to be inadequate for soil moisture retrieval in the drought conditions of the field campaign. These encouraging results indicate that, provided the availability of a wide range of in situ data for the calibration of the model, GAI retrieval in maize crops using only dual-polarized radar data could successfully substitute for estimates derived from optical data when these are not available, such as in the case of persistent cloud cover. Furthermore, the effectiveness of multi-polarized L-band data for GAI monitoring reported in this study highlights the relevance for agriculture of the further development and exploitation of spaceborne L-band SAR with a high revisit time. The upcoming launch of NISAR and ROSE-L, with their L-band, high revisit, and systematic acquisition mode, could allow to extend and scale up the results of this study using a larger set of L-band SAR acquisitions and provide a valuable addition to the C- and X-band sensors already in orbit, which opens up exciting prospects for agricultural applications.

Chapter 4

Joint use of optical and SAR imagery for near real-time green area index retrieval

This chapter is adapted from:

Jean Bouchat, Quentin Deffense, Thomas De Maet, and Pierre Defourny (in prep.). "Joint use of optical and SAR imagery for near real-time green area index retrieval in maize"

—

Abstract

The green area index (GAI) is a key biophysical variable for crop monitoring. Its retrieval often relies on optical remote sensing, which can be hampered by frequent cloud cover. In this context, synthetic aperture radars (SARs) offer the advantage of being able to provide dense time series that can be used to complement sparse GAI time series retrieved from optical data. In this study, a transformer encoder is implemented to perform joint SAR-optical GAI retrieval in maize fields from past and current values of SAR backscatter coefficient and interferometric coherence, as well as past values of GAI when available. Sentinel-1 (S1) and Sentinel-2 (S2) data acquired from 2018 to 2021 over the Hesbaye region of Belgium are used for cross-validation. The results show that the model can successfully predict S2-derived GAI on an unseen growing season with a mean R^2 of 0.88 and root-mean-square error (RMSE) of 0.71. The method is also compared with data collected *in situ* in 10 maize fields in Belgium in 2018 and shown to outperform methods relying on the inversion of

a semi-empirical model based a relaxation of the Water Cloud model (WCM). These promising results pave the way for the generation of accurate, dense GAI time series throughout the crop growing season, ultimately improving the capability of operational crop monitoring systems in cloud-prone regions for which the timely delivery of information can be crucial.

4.1 Introduction

The leaf area index (LAI) is one of the most widely used measurements for the description of plant canopy structure. It is defined as half of the green leaf area per unit of horizontal ground surface area [$m^2\,m^{-2}$] (Chen and Black, 1992). As such, it characterizes the vegetation's capacity to perform photosynthesis and evapotranspiration, intercept rainfall, and exchange gases with the atmosphere (Zheng and Moskal, 2009). It is therefore a key input to Earth's carbon cycle models for the estimation of primary production—the LAI is recognized as an essential climate variable (WMO et al., 2022)—as well as crucial for the agricultural sector for the assessment of the development, health, and productivity of crops (Waldner et al., 2019; Duveiller et al., 2011).

Currently, most large-scale and cost-effective methods for the retrieval of the LAI in agricultural crops exploit optical remote sensing data (McNairn and Shang, 2016; Fang et al., 2019), e.g., De Peppo et al. (2021) and Delloye et al. (2018). More specifically, these methods actually provide their GAI. The GAI can be described as an extension of the LAI to all photosynthetically active elements of the canopy. Frequent cloud cover can, however, hinder the reliability of optical methods by obstructing the view of the sensors on which they rely. This constitutes a major issue since around 70 % of Earth's surface is covered by clouds at any one time (King et al., 2013). As a result, in many parts of the world, timely GAI monitoring cannot be ensured using optical systems alone. This is of considerable concern in many tropical regions where Earth observation (EO)-derived information plays a critical role in food security, and where the presence of clouds often coincides with vegetation growth.

SARs are active sensors operating in the microwave region of the electromagnetic spectrum, allowing them to penetrate clouds and interact with the vegetation. They are therefore capable of producing dense time series that can be used to improve the spatial and temporal coverage of their optical counterparts for land monitoring applications. This capacity can make SAR a considerable asset for operational crop monitoring systems in particular, where early and reliable access to information is of considerable importance. Furthermore, in crops, SAR backscatter is mainly driven by plant geometry and water content, to which the GAI is linked, being a measure of the plant canopy structure and development. Hence, while SAR backscatter is only indirectly linked to GAI, multiple experimental studies have nevertheless demonstrated that it is strongly correlated with it, e.g., Vreugdenhil et al. (2018) and Bouchat et al. (2022b). This sensitivity enables SAR to be used directly, e.g., Baghdadi et al. (2015), Hosseini et al. (2015), and Bouchat et al. (2022a), or as a complement to optical systems to build accurate and dependable methods for its retrieval in crops.

Recent years have seen an unprecedented expansion in the use of large quantities of optical and SAR remote sensing data. This has been made possible by the increased availability of freely accessible imagery, mainly thanks to the launch of the S1 and S2 EO missions by the European Space Agency (ESA) on behalf of the European Commission's Copernicus program. This abundance of data has led to the development of SAR-optical fusion techniques that focus on the reproduction or enhancement of optical imagery from SAR data (Kulkarni and Rege, 2020). Typically, these methods predict missing reflectance values by mapping SAR images to optical images, often using deep learning to model the relationship between both sources of data, and the reconstructed data can in turn be used to derive GAI. However, to date there have been relatively few attempts at exploiting systematic and dense SAR time series to directly fill past or ongoing gaps in optically-derived GAI time series—even though this would potentially avoid an accumulation of modeling errors and reduce production time. Efforts have nevertheless been made in this direction in recent years, but they have mainly been focused on the normalized difference vegetation index (NDVI) instead. Garioud et al. (2020) used SAR indices derived from S1 acquisitions as well as contextual data as inputs to a recurrent neural network for the estimation of S2-derived NDVI over grasslands. Li et al. (2022) extended the target of their regression to the S2-derived NDVI of both agricultural and woodlands. They used the dual-pol radar vegetation index (dpRVI) (Nasirzadehdizaji et al., 2019) computed from S1 backscatter data and a temporal-spatial transformer model to estimate it. Regarding GAI, more recently, Mastro et al. (2023), in their extension of the work of Pipia et al. (2019), explored the potential of SAR-based vegetation indices to fill gaps in S2-derived GAI time series over, among other crops, maize, through a multi-output Gaussian process approach.

In this chapter, joint SAR-optical GAI retrieval is performed over maize fields using dense C-band SAR time series from S1 and sparse GAI time series retrieved from optical images acquired by S2. The objective is to increase not only the temporal resolution but also the timeliness of operational crop monitoring systems that rely on optical data. The emphasis is therefore on retrieving new missing data as they come in—most often due to cloud cover—, rather than past data. The method therefore works as follows. First, GAI is retrieved along the growing season from S2 images using the algorithm in Delloye et al. (2018). Then, whenever gaps occur, they are filled using S1 data as well as previous S2-derived GAI values. The regression task is carried out by a transformer encoder neural network (Vaswani et al., 2017), for its ability to model highly complex dynamics and understand the sequential nature of the values to be retrieved. The accuracy of the method is then assessed both through cross-validation and external validation with *in situ* data collected during the BELSAR campaign, described in Chapter 2.

4.2 Materials and methods

4.2.1 Study area

The 53 km by 27.5 km area of interest (AOI), depicted in Figure 4.1, is located in Hesbaye region of Belgium. It is mostly covered by relatively large, homogeneous, and flat fields with a uniform topsoil texture of silt loam. The boundaries and crop types of all fields present within the AOI are inventoried in the anonymized land parcel identification system of Wallonia (Service public de Wallonie, 2021).

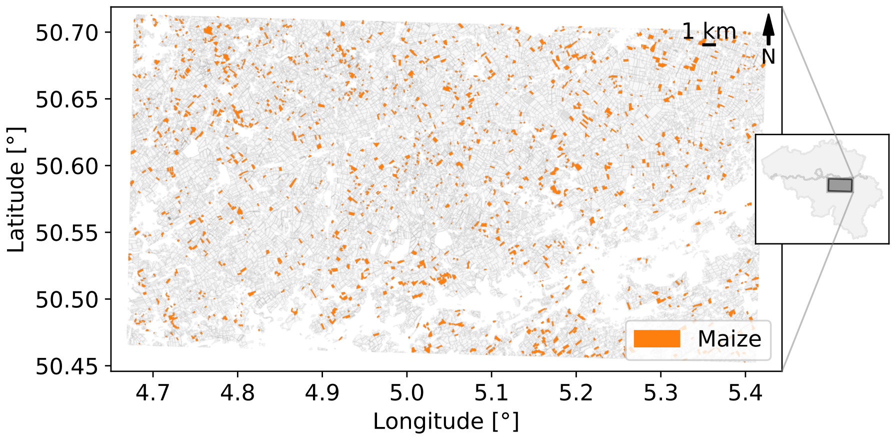

Figure 4.1: Area of interest in 2019 with maize fields in orange and all the other agricultural fields in gray.

4.2.2 Satellite imagery

The AOI is contained in S2's 31UFS tile, with a revisit period of 2.5 days, and four S1 relative orbits, two ascending: 88 and 161, and two descending: 37 and 110, with an average revisit of 3 days between two passes in the same direction. Only the 2018 to 2021 growing seasons are considered in this study. Ulterior years were not taken into account due to the loss of Sentinel-1B on December 23, 2021, halving the constellation's acquisition density above the AOI. All satellite images are downloaded from the Copernicus Data Space Ecosystem (*Copernicus Data Space Ecosystem*, 2024).

SAR data from Sentinel-1

C-band SAR data acquired by the S1 constellation in interferometric wide (IW) swath mode are received in level-1 single-look complex (SLC) format and pre-processed with ESA's Sentinel-1 toolbox (S1TBX) using the Sentinel Application Platform (SNAP) (*SNAP – ESA Sentinel Application Platform v9.0.0*, 2022).

Backscattering coefficients σ_0 are obtained through: (1) TOPSAR split; (2) orbit file application; (3) thermal noise removal; (4) calibration to σ_0; (5) TOPSAR deburst; and (6) TOPSAR merge. The chain to

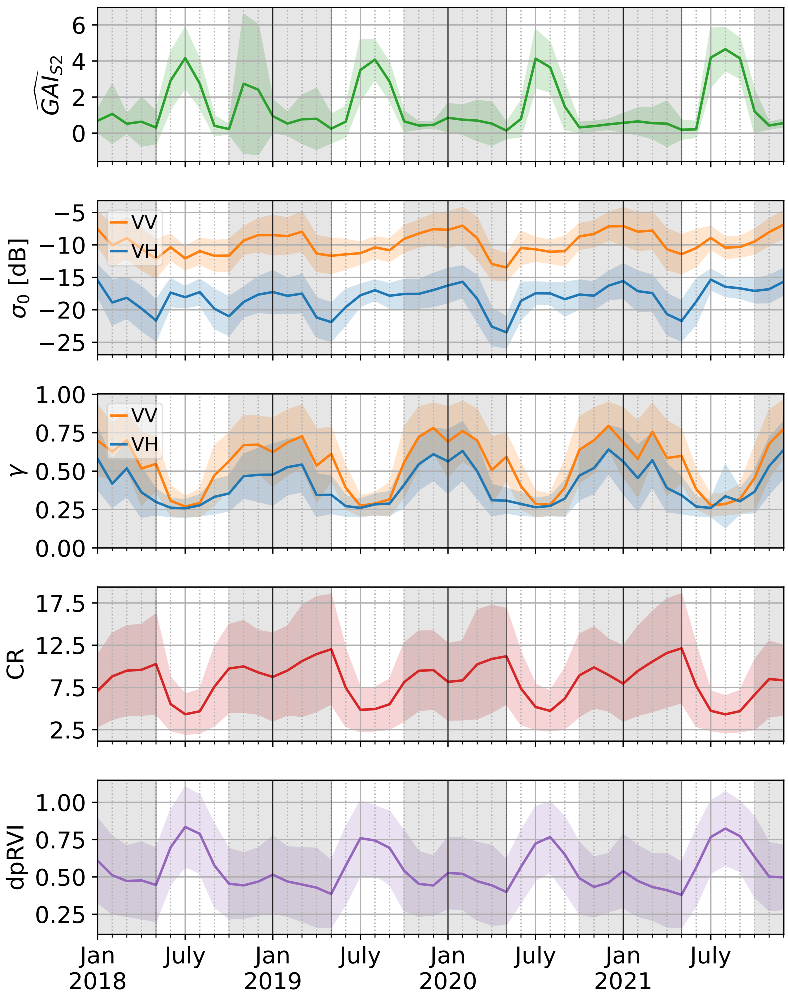

Figure 4.2: Time series of the mean (**top to bottom**) S2-derived GAI ($\widehat{\mathrm{GAI}}_{\mathrm{S2}}$), co- and cross- backscattering coefficients (VH, VV), 6-day interferometric coherence (γ), cross-ratio (CR), and dual-pol radar vegetation index (dpRVI), over all maize fields—the number of which varies from year to year—in the area of interest. Translucent areas represent one standard deviation either side from the mean. Shaded areas are outside the considered growing seasons and are therefore discarded.

compute interferometric coherence (γ) follows: (1) orbit file application; (2) calibration to σ_0; (3) TOPSAR split; (4) back-geocoding; (5) computation of the coherence γ; (6) TOPSAR deburst; and (7) TOPSAR merge. Finally, both products are terrain corrected using the Range Doppler orthorectification method with the Shuttle Radar Topography Mission (SRTM) 1 Arc-Second Global digital elevation model (DEM) (Eros, 2015) and resampled through a bilinear interpolation method to a 10 m pixel grid.

Zonal statistics (mean, standard deviation, maximum, and minimum) of the backscattering coefficient σ_0 and 6-day repeat-pass interferometric coherence, γ, as well as the mean local incidence angle, are then computed for each field. To avoid edge effects, an inner buffer of 20 m is imposed beforehand on the boundaries of the polygons designating the fields. Finally, two frequently used SAR vegetation indices are calculated: the cross-ratio (CR) (Vreugdenhil et al., 2018), CR = VV/VH, and the dpRVI (Nasirzadehdizaji et al., 2019),

$$\mathrm{dpRVI} = \frac{4\ \mathrm{VH}}{\mathrm{VH} + \mathrm{VV}}.$$

Time series of the average σ_0 and γ in VH and VV, CR, and dpRVI over all maize fields in the dataset are represented in Figure 4.2. The number of fields varies from year to year, it is reported in Table 4.2.

GAI retrieved from Sentinel-2 data

The S2 multi-spectral images are acquired in L1C format (ortho-rectified top-of-atmosphere reflectances). They are processed with Maccs-Atcor Joint Algorithm (MAJA), a tool for atmospheric correction and cloud detection developed by the CESBIO and CNES (*MAJA – The Multi-Temporal Cloud Screening and Atmospheric Correction Software v4.5.4*, 2022). From the 31UFS tile of 110×110 km^2 are extracted three bands at 10 m-resolution (B3, B4, B8) and four at 20 m-resolution (B5, B6, B7 and B11), along with the sun and view angles. The images are resampled to a 10 m pixel distance while the angles are averaged over the tile. GAI is then retrieved from these inputs using a neural network trained with the BV-NET tool as described in Delloye et al. (2018). Finally, a mask is applied to the resulting GAI image, excluding the clouds and their shadows.

4.2.3 SAR-optical GAI retrieval

The retrieval of a missing GAI value for a given date and field is performed using a transformer encoder with past and present SAR data alongside past GAI values acquired over the field in question during the considered growing season. Results are evaluated by means of a nested cross-validation and an external validation with *in situ* GAI measurements.

Transformer encoder

Retrieving the GAI of a crop at a given date from past and present SAR data, as well as from past values of the GAI, requires the regression model to be able to represent the non-linear relationship between SAR backscatter and GAI. In addition, in order to benefit from all the information available, the model must be able to take into account the influence of past SAR data and GAI on the current value of the latter. Finally, to help improve the information density of operational GAI monitoring systems, the model needs to be scalable, i.e., it has to be able to handle large amounts of data without being prohibitively expensive to run.

Introduced by Vaswani et al. (2017), transformers are deep-learning architectures primarily used in natural language processing (NLP). As all deep-learning models, they are capable of handling nonlinear relationships between inputs and outputs effectively, and, similarly to recursive neural networks (RNNs), such as the gated recurrent unit (GRU) (Cho et al., 2014), transformer encoders are designed to handle sequential data. However, unlike RNNs, they are less susceptible to the vanishing gradient problem thanks to their self-attention mechanism which eliminates the need for sequential input processing. This allows the model to weight the importance of elements in the input sequence as it encodes them, enabling it to concentrate on the parts of the input that are most relevant to the given task and to take better account of long-term dependencies between them. Noteworthy is also the transformer encoders' inherent parallelizability, which makes them particularly suitable for exploiting large data sets. These advantages explain why they are being rapidly adopted well beyond the scope of NLP, as is the case in this study.

To retrieve the GAI of a crop, the transformer encoder implemented

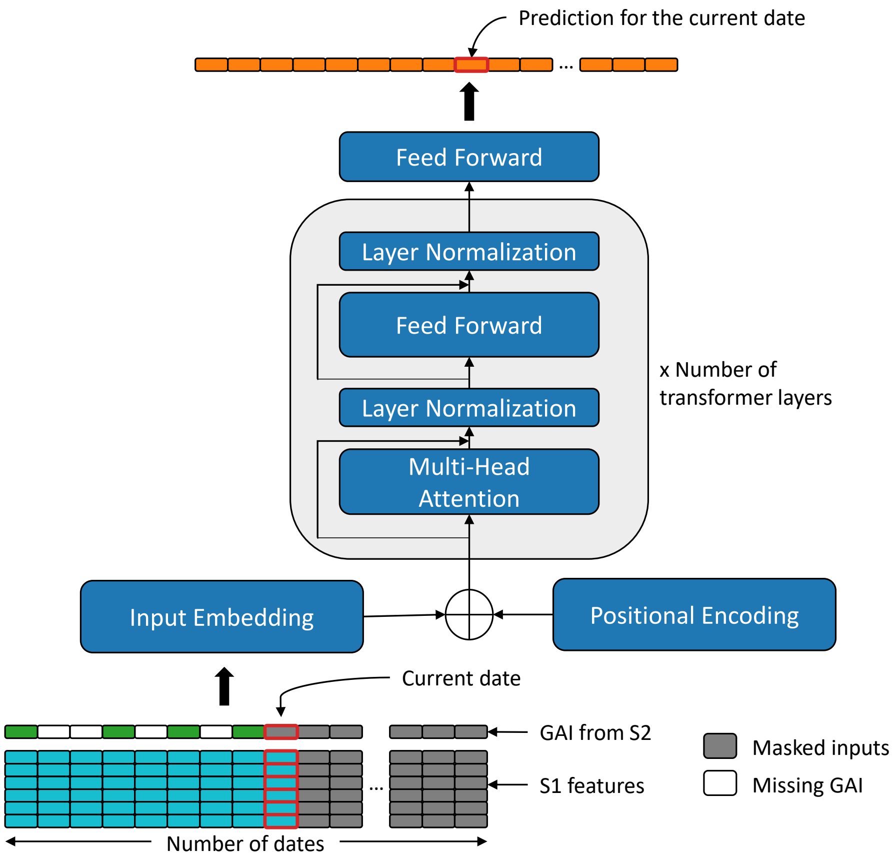

Figure 4.3: Diagram of the implemented transformer encoder.

in this study uses dense time series of SAR data from S1 and sparse GAI data derived from S2 images. Since the purpose of the model is the operational monitoring of the GAI throughout the crop growing season, it only integrates past GAI values, when available, and past and present SAR data to retrieve the current value of the GAI whenever it is missing, e.g., due to a lack of cloud-free optical data. The model flowchart can be found in Figure 4.3.

To build a dataset that can be easily processed by the model, and because acquisition times vary widely between relative orbits, rendering

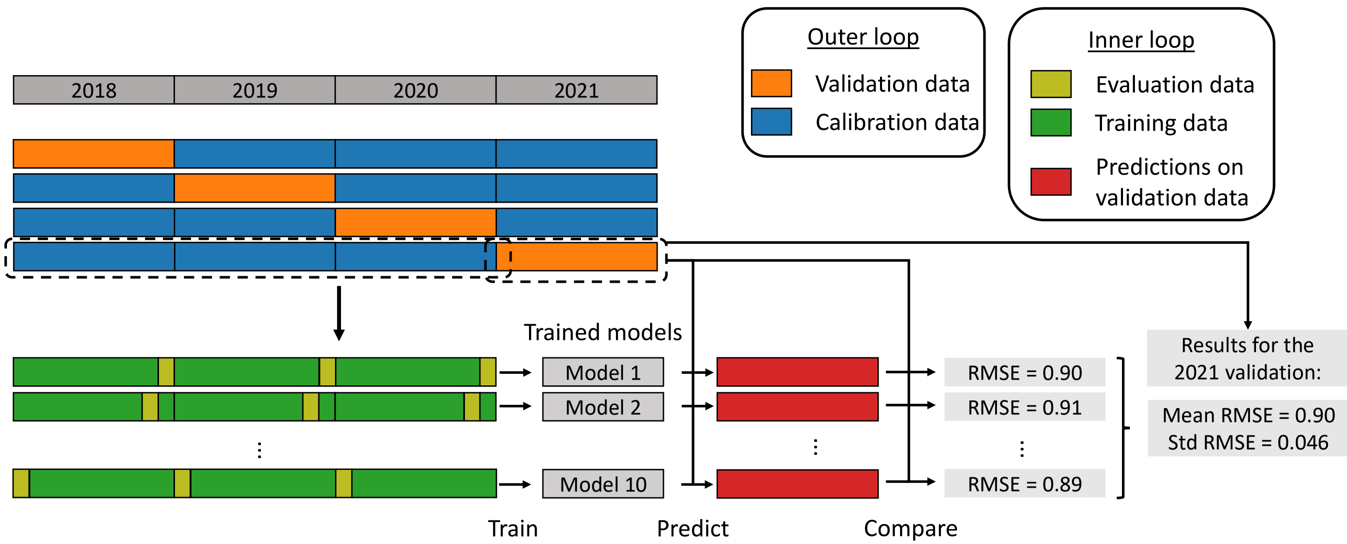

Figure 4.4: Nested cross-validation scheme. The outer loop consists in a 4-fold cross-validation, dividing fields according to the growing seasons. In each of the 4 folds runs a 10-fold cross-validation (inner loop), where the fields in the considered calibration set are randomly divided into 10 subsets. Each of these subsets serves in turn as an evaluation set, while the remaining 9 are used for training. For each growing season, the generalization error of the model is obtained by averaging the validation errors committed by the 10 models trained in the inner loop.

them incomparable in the AOI due in part to the effect of morning dew affecting only the descending acquisitions, S1 data in both ascending and descending orbits are matched on a common one-dimensional temporal grid indexed to S1's descending orbit acquisitions, as in Garioud et al. (2020). Accordingly, there are both an ascending and a descending acquisition for each time step of the model, and the latter is defined by the period between two SAR acquisitions in descending orbit. When they are available, the input GAI values are set on the grid by temporal interpolation using the nearest neighbor algorithm. Furthermore, a GAI value in considered missing on this grid when the closest S2 image from which it was retrieved is more than 5 days apart from the considered descending acquisition.

The method is object-based, meaning that for a given field, model features are computed over all pixels within (buffered) field boundaries. The SAR features of the model consist of, for both ascending and descending orbits, the mean, standard deviation, minimum, and maximum values of the backscattering coefficient and interferometric coherence in both VH and VV polarizations, the mean local incidence angle, the CR, and the dpRVI. With the addition of past GAI, this results in a total of 39 features per date of the time series. It should be noted that, although it could be an interesting feature because of its effect on backscatter, as demonstrated in Chapter 2, the orientation of maize rows is not included in the feature set simply because it was not readily available.

While the model is designed for filling gaps in time series as they occur, i.e., in near real-time, the same model architecture can also be used to populate gaps in past time series, where previous and subsequent values are known. However, since the method is designed for the ongoing retrieval of the GAI, it does not exploit knowledge of the values following the missing value, which could obviously improve its retrieval accuracy.

Nested cross-validation

The performance of the transformer encoder for GAI retrieval is evaluated and then compared to that of two models, a multilayer perceptron (MLP) and a bidirectional gated recurrent unit (BiGRU), to highlight its specific capabilities.

The MLP, commonly known as a "vanilla" neural network, belongs to the class of feed-forward neural networks. It is capable of modeling linear and non-linear relationships between inputs and outputs, and, under certain conditions, is also able to implicitly understand temporal relationships between them. The BiGRU belongs to the class of RNNs. It keeps an internal hidden state (or memory) that is updated for each date of the data sequence. This memory enables it to explicitly account for the sequential nature of the targeted data, as does the transform encoder. Establishing long-term contextual dependencies is difficult when using RNNs to extract information from long time series of inputs (Hochreiter et al., 2001). To improve it, although imperfectly, the BiGRU processes input time series in two directions, from beginning to end and vice versa. The interest in comparing the transformer encoder with the MLP and the BiGRU is to assess the usefulness of using a model capable of understanding the sequential nature of its inputs and outputs, which the MLP does not have the explicit capacity to do, as well as the long-term contextual dependencies between inputs, a task for which the BiGRU is theoretically less capable than the transformer encoder.

The performances of the models are evaluated using a nested cross-validation procedure, illustrated in Figure 4.4. Cross-validation is performed at two levels; for each fold of the external cross-validation, another internal cross-validation is performed. These are referred to as external and internal loops respectively.

The outer loop is used to estimate the generalization error of the model. The dataset is divided into four, according to the growing seasons it comprises, from 2018 to 2021. In each of the four outer folds, the calibration set contains the data from three growing seasons and the validation set the data from the remaining one.

This inner loop is where models are both trained and evaluated with data from the calibration set. It consists of a 10-fold cross-validation, where, for each fold, 90 % of the fields in the calibration set are randomly selected to train a model and the rest is used for its evaluation. The evaluation set serves for regularizing the learning, i.e., the optimization procedure of the model parameters. This practice, called early stopping, prevents overfitting to some extent. The model learns on its training set and, at the end of each epoch, i.e., one complete run of the learning procedure through the training set, evaluates its performance on its evaluation set. If this performance stops improving after an arbitrary number of epochs, the learning procedure stops and the model weights

Table 4.1: Error metrics used to measure model performance, where $\hat{y}_i$, $i = 1, \ldots, N$, are the predictions, y_i, $i = 1, \ldots, N$, the reference values, and $\bar{y}$ the arithmetic mean of the latter.

Error metric	**Symbol**	**Definition**
Coefficient of determination	R^2	$1 - \frac{\sum_{i=1}^{N}(y_i - \hat{y}_i)^2}{\sum_{i=0}^{N}(y_i - \bar{y})^2}$
Root-mean-square error	$RMSE$	$\sqrt{\frac{1}{N}\sum_{i=1}^{N}(y_i - \hat{y}_i)^2}$
Relative RMSE	$RRMSE$	$\frac{1}{\bar{y}}\sqrt{\frac{1}{N}\sum_{i=1}^{N}(y_i - \hat{y}_i)^2}$
Mean absolute error	MAE	$\frac{1}{N}\sum_{i=1}^{N}\lvert y_i - \hat{y}_i\rvert$
Relative MAE	$RMAE$	$\frac{1}{\bar{y}}\frac{1}{N}\sum_{i=1}^{N}\lvert y_i - \hat{y}_i\rvert$

are set.

Quantifying the performance of the method in the outer loop then consists in measuring the predictions of the 10 models trained in the inner loop against the corresponding validation set, and then averaging their respective errors. The definition of the error metrics used to measure model performance can be found in Table 4.1.

External validation

The external validation of the model is performed by training it on data from 2019 to 2021 and testing it against GAI data collected *in situ* during the 2018 growing season.

These *in situ* data ($N = 34$) were collected in the AOI on three to four separate occasions, depending on the field, at approximately one-month intervals, in 10 maize fields between May 30 and August 30, 2018 during the BELSAR campaign. In each field, GAI was measured in three homogeneous and representative subplots by means of digital hemispherical pictures (DHPs) processed with the CAN-EYE software (Weiss and Baret, 2017). The measurements were then averaged across the subplots to provide field-level values of the variable.

Details about the *in situ* data collection can be found in Chapter 2.

4.3 Results and discussion

4.3.1 GAI retrieval

The implemented transformer encoder starts with embedding the inputs with two dense layers of sizes 48 and 64. A positional encoding using sine and cosine functions is added to the input's embedding, as in Vaswani et al. (2017). The two transformer layers have four heads and a hidden size of 64. The model output is generated with two layers of size 32 and 1. The models are trained for 400 epochs with a patience of 30 epochs, a learning rate of 5×10^{-4} and a dropout rate of 0.2. These hyperparameters have been tuned empirically on the evaluation datasets in the inner loop.

For a given parcel at a given date, the model prediction—called predicted GAI ($\widehat{\text{GAI}}_{\text{S1-S2}}$)—is generated using the 38 SAR features described in Section 4.2.2 and the S2-derived GAI values—called reference GAI ($\widehat{\text{GAI}}_{\text{S2}}$)—from the past for each of the 31 S1 images in descending orbit acquired during the growing season—defined as beginning on May 1 and ending on October 30. This amounts to an input matrix of size $31 \cdot 39 = 1209$. Since the model is designed to generate its predictions progressively as S1 data are acquired, any future value of the SAR features is encoded as 0, while future and missing values (e.g., due to cloud cover) of the GAI are encoded as -1. These values are set arbitrarily outside their normal range.

Nested cross-validation results

The outer loop of the nested cross-validation is run on four growing seasons, from 2018 to 2021. In each of the four outer folds, 10 transformer encoders—the inner loop consisting in a 10-fold cross-validation—are trained on the data from three growing seasons and validated on data from the fourth. Validation results are displayed in Figure 4.5, where one-to-one plots demonstrate, for each growing season, the prediction performance of a randomly selected model from the inner loop. The mean and standard deviation of the error metrics computed over all 10 folds of the inner loop are reported in Table 4.2, and examples of times series of retrieved GAI are displayed in Figure 4.7.

The results for the 2018 to 2020 growing seasons are similar, with a

Table 4.2: Detailed nested cross-validation results (outer loop) for the transformer encoder, aggregated (total) and split between each fold (2018-2021). N and N_{parcels} are the number of data and parcels, respectively.

	Total		**2018**		**2019**		**2020**		**2021**	
	Mean	**Std**	**Mean**	**Std**	**Mean**	**Std**	**Mean**	**Std**	**Mean**	**Std**
R^2	0.87	0.009	0.89	0.017	0.89	0.007	0.87	0.017	0.84	0.017
$RMSE$	0.75	0.026	0.72	0.053	0.65	0.020	0.69	0.043	0.90	0.046
$RRMSE$	0.35	0.012	0.35	0.026	0.27	0.008	0.42	0.026	0.37	0.019
MAE	0.48	0.016	0.46	0.034	0.44	0.014	0.43	0.022	0.60	0.032
$RMAE$	0.23	0.007	0.22	0.017	0.18	0.006	0.26	0.014	0.25	0.013
N	17710	0	4146	0	3927	0	5205	0	4432	0
N_{parcels}	954	0	206	0	228	0	267	0	253	0

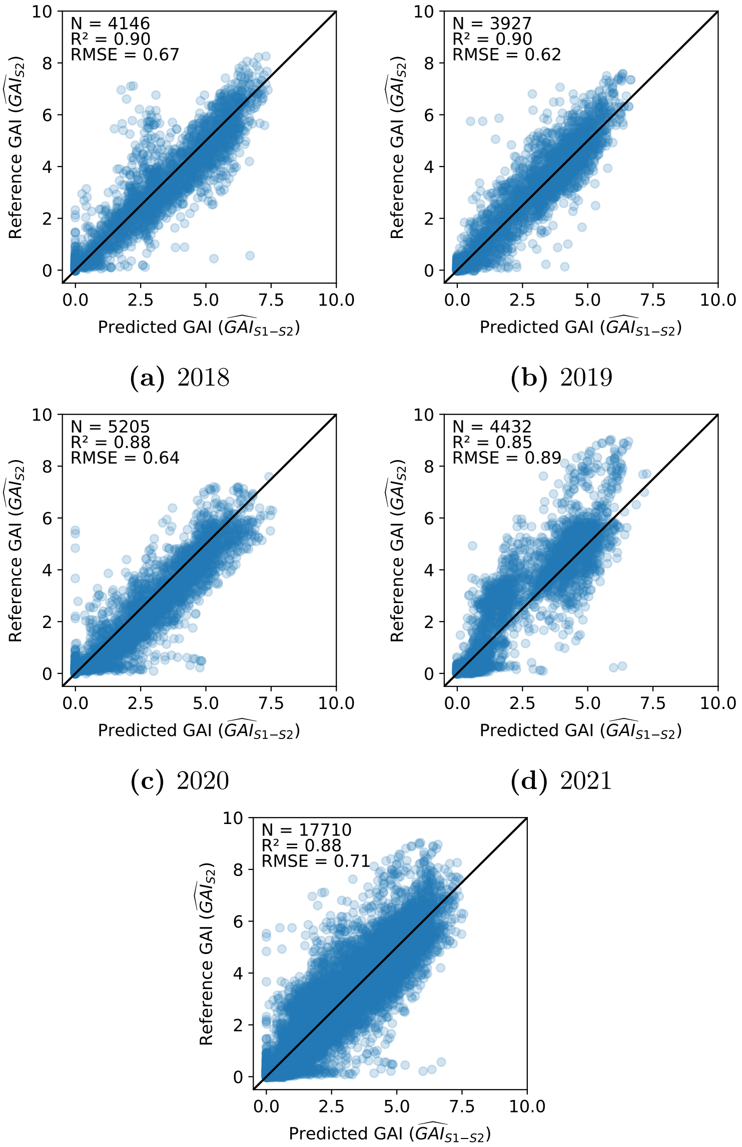

(a) 2018 **(b)** 2019

(c) 2020 **(d)** 2021

(e) Total

Figure 4.5: Nested cross-validation results for the transformer encoder (**a-d**) split between each growing season (2018-2021) and (**e**) aggregated. For each growing season, the model is trained with data from the other three years only.

mean R^2 between 0.87 and 0.89 and a mean RMSE between 0.65 and 0.72. The results for 2021, on the other hand, are substantially less accurate, with a mean R^2 of 0.84 and, especially, a mean RMSE of 0.90. The number of maize parcels (N_{parcels}) and data (N), i.e., the number of $\widehat{\text{GAI}}_{\text{S2}}$ for all parcels, are comparable year-to-year, with more than 200 parcels each year and N ranging from 3927 in 2019 and 5205 in 2020. It is therefore unlikely that the disparities between 2021 and the rest are related to the size of the sample. An explanation could be found in the effect on SAR acquisitions of the unprecedented heavy rainfall that led to flooding in many parts of Belgium in mid-July 2021. Their effect is likely apparent on the time series in Figure 4.2, where backscattering coefficients in both polarizations have higher values in July of that year than in previous years. This may have led to the underestimation of low S2-derived GAI values ($\widehat{\text{GAI}}_{\text{S2}} < 2.5$) visible in Figure 4.5. Besides accounting for the poorer results for 2021, the abnormal growing season could also be expected to have had an impact on the results for the 2018-2020 growing seasons, since the 2021 data were used to train the model validated on the latter.

Feature influence

To assess the influence of features on the retrieval of the present GAI value by the transformer encoder, a similar model is trained without any S1 features, i.e., the only model inputs are the past GAI values with the other parameters remaining unchanged. Its predictions are referred to as $\widehat{\text{GAI}}_{\text{S2 only}}$. Nested cross-validation results for this model and the one that, in addition to GAI past values, uses the S1 features are shown and compared in Figure 4.6.

The results plotted in Figure 4.6a indicate the higher variability and lower accuracy of $\widehat{\text{GAI}}_{\text{S2 only}}$ predictions. This is evidenced by the fact that they are more spread out around the 1:1 line than $\widehat{\text{GAI}}_{\text{S1-S2}}$. This observation is quantified by their respective RMSEs, 0.85 for the former and 0.71 for the latter. This suggests that the SAR features provide very relevant information for the model, particularly at low GAI values.

The errors made by the two transformer encoders as a function of the number of days since the last available $\widehat{\text{GAI}}_{\text{S2}}$, i.e., the last cloudless image of the parcel from S2, are reported in Figure 4.6b. The error committed by the transformer encoder using only past GAI as input is always

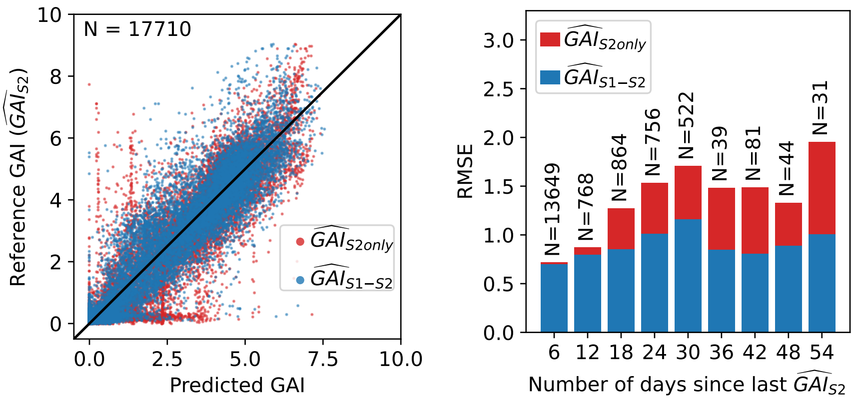

(a) **(b)**

Figure 4.6: Influence of past GAI values on the performance of the transformer encoder with, (**a**) the aggregated cross-validation results and (**b**) the effect of the length of time since the last available (cloud-free) optical image on the prediction error, for the transformer encoder using both Sentinel-1 features and past GAI (in blue) and only past GAI (in red).

greater than the other. This difference, as well as both errors, increases with the period between the last cloud-free S2 image and the date for which the GAI is retrieved, up until one month, i.e., around two fifths of the period between emergence and peak GAI. Afterwards, the errors stop strictly increasing. The cause of this unlikely behavior is probably the sharp reduction in the number of data points ($N \in [31, 81]$), making the ulterior samples non-representative. The similarity between the two errors at the start of the time series tends to show that past GAI is an important input for the model, but their significant divergence for longer time periods indicates that, despite capturing the sequential nature of the target variable, the transformer encoder does not act as a simple extrapolator. The ability of the model to effectively exploit the information in the S1 features is also highlighted by the stability of the error committed for $\widehat{\text{GAI}}_{\text{S1-S2}}$ in spite of the drastic changes vegetation undergoes in 30 days, i.e., a fifth of the period between emergence and harvest. This also points to the dependability of C-band SAR for agricultural

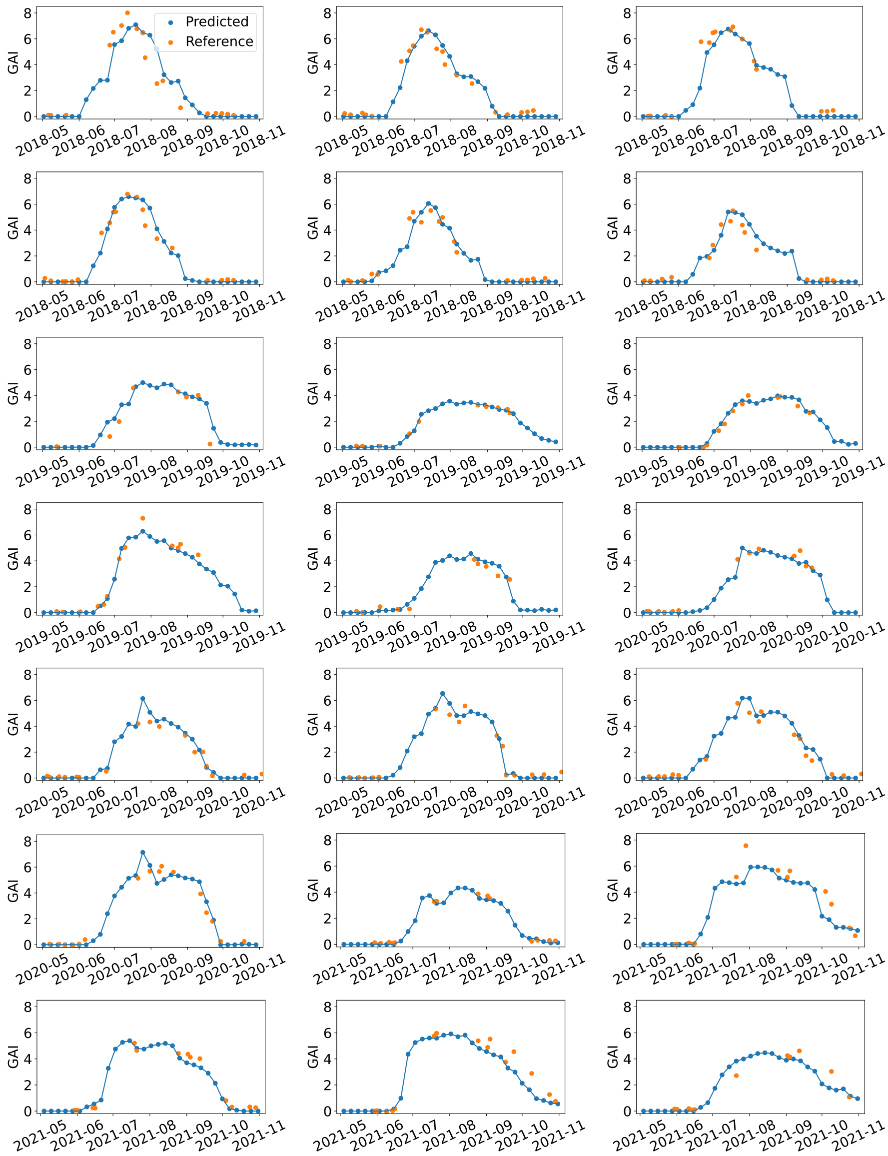

Figure 4.7: Examples of retrieved GAI time series.

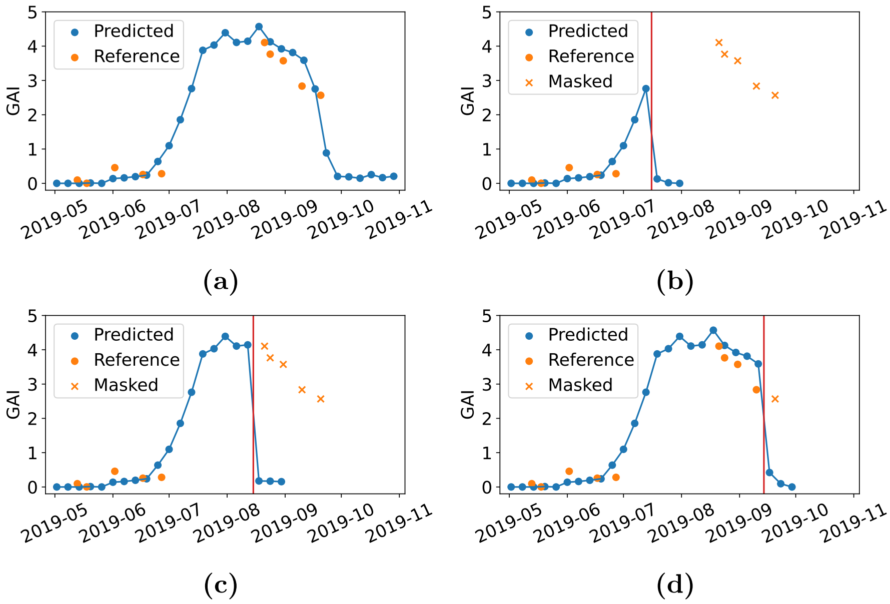

Figure 4.8: Example of (**a**) a retrieved GAI time series, (**b**) with an early, (**c**) mid, and (**d**) late simulated harvest event (red line). Reference and masked GAI are retrieved from Sentinel-2 images. The transformer encoder, trained with data from the 2018, 2020, and 2021 growing seasons, is able to detect the unexpected event.

monitoring.

The reliance of the model on the S1 features is also apparent in the early harvest simulations, an example of which is shown in Figure 4.8. To simulate these events, the validation time series were modified: the last three values of each feature were shifted to different points in the time series and substituted for the actual values at these points, so as to jump from the image of a vegetated parcel to that of a bare one (or one with maize stubbles remaining, as is common in the region of interest) after harvest. The timely and appropriate response of the model to these unexpected events—none, or a negligible number of parcels in the dataset underwent a similar early harvest—is evidence of the importance given to the SAR data rather than to past GAI values. This behavior is not inherent to this architecture, however, and other types of model could

Table 4.3: Nested-cross validation results (outer loop) for the bidirectional gated recurrent unit (BiGRU) and the multilayer perceptron (MLP). Error metrics are computed over 954 parcels, $N = 17710$.

	BiGRU		**MLP**	
	Mean	**Std**	**Mean**	**Std**
R^2	0.88	0.006	0.72	0.017
$RMSE$	0.73	0.019	1.10	0.033
$RRMSE$	0.35	0.009	0.52	0.016
MAE	0.48	0.012	0.74	0.021
$RMAE$	0.23	0.006	0.35	0.010

achieve the same desirable result through input regularization or data augmentation.

4.3.2 Multiple model comparison

The transformer encoder is compared with two other models, a MLP and a BiGRU. All three are trained and cross-validated on the same data. The nested cross-validation results of the former are reported in Table 4.2 and those of the MLP and BiGRU in Table 4.3.

As with the transformer encoder, the hyperparameters of both models are tuned empirically. The MLP consists of three dense layers with hidden sizes of 256, 128, and 64, respectively. As for the BiGRU model, it starts with embedding the inputs with a dense layer of size 64, followed by two BiGRU layers of size 128 to explore their temporal dimension. Finally, three dense layers with sizes of 64, 32, and 1 are used to predict the GAI for each time step. Both models were trained with the same number of epochs, patience, learning rate and dropout rate as the transformer encoder.

The poorer results of the MLP ($R^2 = 0.72$, $RMSE = 1.10$) can probably be explained, at least in part, by the ability of the other two models to better exploit the temporal relationships between GAI values along the crop growing season. This highlights how the model benefits from being able to explicitly take into account the influence of past values

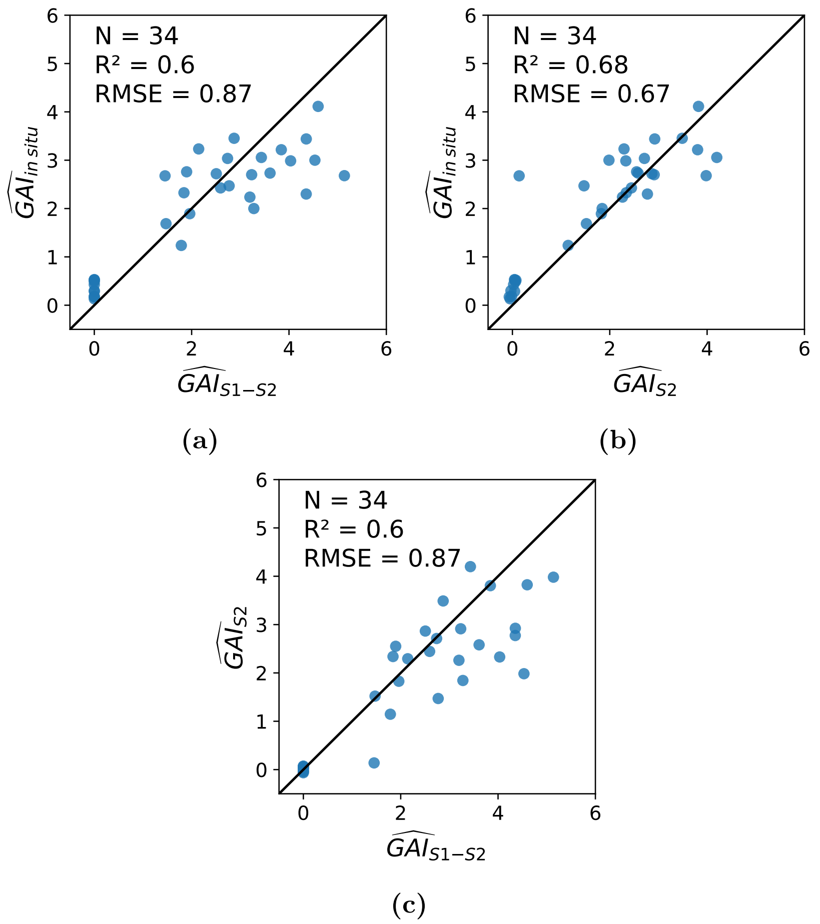

Figure 4.9: Results from the external validation with (**a**) the model estimates ($\widehat{\mathrm{GAI}}_{\text{S1-S2}}$) against the *in situ* data ($\widehat{\mathrm{GAI}}_{\text{in situ}}$), (**b**) the S2-derived GAI ($\widehat{\mathrm{GAI}}_{\text{S2}}$) against the *in situ* data, and (**c**) the model performance. The model is trained on data from 2019 to 2021, while the *in situ* data were collected in 2018. For clarity, the results displayed are produced using only one of the 10 models trained in the inner cross-validation loop.

Table 4.4: Results of the external validation with the transformer encoder models trained on data from 2019 to 2021 and tested on data from 2018. Error metrics are computed over 10 parcels, $N = 34$.

	$\widehat{\mathbf{GAI}}_{\mathbf{S1\text{-}S2}}$ vs $\widehat{\mathbf{GAI}}_{\mathbf{in\ situ}}$		$\widehat{\mathbf{GAI}}_{\mathbf{S1\text{-}S2}}$ vs $\widehat{\mathbf{GAI}}_{\mathbf{S2}}$		$\widehat{\mathbf{GAI}}_{\mathbf{S2}}$ vs $\widehat{\mathbf{GAI}}_{\mathbf{in\ situ}}$
	Mean	**Std**	**Mean**	**Std**	
R^2	0.43	0.114	0.50	0.117	0.68
$RMSE$	0.89	0.085	0.97	0.108	0.67
$RRMSE$	0.44	0.043	0.54	0.061	0.34
MAE	0.66	0.071	0.66	0.089	0.46
$RMAE$	0.33	0.035	0.37	0.050	0.23

of the GAI on its current value. As for the equivalence between the results of the transformer encoder ($R^2 = 0.87$, $RMSE = 0.75$) and the BiGRU ($R^2 = 0.88$, $RMSE = 0.73$), it can be due to the relatively small size of the time series considered (31 dates), for which the ability of the transformer encoder to account for long-term contextual dependencies is not particularly beneficial. This ability would be expected to make a difference in performance to the advantage of the transformer encoder, however, if the model were used to retrieve the GAI of a parcel across several growing seasons rather than one, and even more so in the presence of cover crops or annual crop rotation impacting subsequent crop growing conditions.

4.3.3 External validation

External validation of the model is carried out using the GAI estimates collected in the field, $\widehat{\text{GAI}}_{\text{in situ}}$. Comparative retrieval results are displayed in Figure 4.9 and reported in detail in Table 4.4.

The results of the transformer encoder for the retrieval of the S2-derived GAI on the 10 parcels in which GAI was collected by means of DHPs, and on those dates where it was, are significantly worse ($R^2 = 0.50$, $RMSE = 0.97$) than for the whole dataset ($R^2 = 0.87$, $RMSE = 0.75$). This discrepancy can be attributed to a sampling effect ($N = 34$) that potentially affects the subsequent analysis as well.

The GAI derived from S2, $\widehat{\text{GAI}}_{\text{S2}}$, are significantly closer to the values measured *in situ*, $\widehat{\text{GAI}}_{\text{in situ}}$ ($R^2 = 0.68$, $RMSE = 0.67$), than are the values predicted by the transform encoder, $\widehat{\text{GAI}}_{\text{S1-S2}}$ ($R^2 = 0.43$, $RMSE = 0.89$). However, the comparison drawn here between $\widehat{\text{GAI}}_{\text{S1-S2}}$ and $\widehat{\text{GAI}}_{\text{in situ}}$ must be interpreted with caution. Field measurement via DHPs is in fact only a third method of estimating the true value of the GAI, and the objective of the model presented in this chapter remains the retrieval of $\widehat{\text{GAI}}_{\text{S2}}$ for the gap-filling of time series derived from optical imagery, a task that the model fulfills with far greater success in general.

Still, the errors incurred by the transformer encoder between $\widehat{\text{GAI}}_{\text{S1-S2}}$ and $\widehat{\text{GAI}}_{\text{in situ}}$ are better than those obtained in Chapter 3 by inverting a semi-empirical model based on the WCM with the same S1 acquisitions ($RMSE = 0.98$), noting however that only 8 of the 10 parcels were considered in that study. The apparent equivalence between the results of the method presented in this study and those of the previous chapter must be qualified, however. For the semi-empirical model, only eight relatively similar parcels for which *in situ* data were available. Field measurements were all carried out during a single growing season and at similar times for all fields, i.e., at specific vegetation development stages and under similar soil moisture conditions. The semi-empirical model therefore benefited from being both calibrated and validated on a fairly homogeneous dataset. In contrast, the transformer encoder was calibrated on the 2019-2021 growing seasons and validated on the BELSAR fields in 2018, putting it at an obvious disadvantage in this comparison.

Finally, in the above-mentioned study, the use of L-band SAR data yielded results equivalent to those obtained with the transformer encoder ($RMSE = 0.77$). The better performance of L-band SAR is probably due to its greater ability to penetrate and therefore interact with dense vegetation in high-biomass crops such as maize. This suggests that the use of multi-frequency SAR data, in both C- and L-band, could greatly improve the performance of the transformer encoder for GAI retrieval.

4.4 Conclusion

A method was presented in this chapter to fill gaps in optically-derived GAI times series as they occur along the crop growing season, e.g., due to cloud cover, with current and past SAR data as well as past GAI values. The approach involves the use of a transformer encoder, a deep-learning architecture that exploits the sequential nature of the values of the target variable and its complex relationship with SAR backscatter. Promising results were obtained in maize, a high-biomass crop notoriously difficult to monitor in C-band, suggesting that the method could easily be extended to other major temporary crops. The comparison of these results with those obtained by the inversion of the semi-empirical model in Chapter 3 indicated that its accuracy could also soon be further improved through the use of multi-frequency SAR data, in C- and L-band, with the forthcoming launch of the NISAR and ROSE-L missions.

Ultimately, while most current global vegetation monitoring systems have resolutions ranging from 300 m to 1 km, e.g., to ensure a revisit period short enough to minimize the impact of clouds, the proposed method could allow to better capture, in near real-time, vegetation dynamics at high-resolution for finer crop monitoring and yield forecasting. The added value of such method, capable of producing usable data on crop condition regardless of cloud cover, would be all the more evident in regions of the world where optical remote sensing is seriously hindered by the very frequent presence of clouds, impacting food security early warning systems.

Chapter 5

Conclusions and perspectives

The primary objective of this thesis was to improve the retrieval of the green area index (GAI) in maize crops using synthetic aperture radar (SAR) remote sensing with a perspective towards near real-time, large scale crop monitoring at the parcel level. Emphasis was placed on the GAI for its importance in crop growth models and yield forecasting (Fang et al., 2019), but also in climate models (Mahowald et al., 2016; WMO et al., 2022), and on maize because it is a crop which is particularly challenging to monitor via SAR remote sensing due to its high biomass (Bériaux et al., 2015) and row structure. From this general objective were derived three research questions which were addressed in Chapters 2 to 4: (i) *How sensitive is multistatic SAR in L-band to maize biophysical variables?* (ii) *Is SAR remote sensing alone sufficient to ensure reliable, timely, and accurate GAI monitoring in maize?* (iii) *How can SAR be combined with optical remote sensing to increase the temporal resolution of crop monitoring systems?* The work carried out in response to these questions has made a number of contributions to the state of the art, and opened up perspectives for further improving crop monitoring systems.

5.1 Conclusions

The first investigation, reported in Chapter 2, aimed to assess the sensitivity of L-band multistatic full-pol SAR to a range of crop and soil biogeophysical parameters in vegetated maize fields and bare winter wheat fields. The intention behind this study was to address a research gap in the study of the potential of multistatic SAR and, to a lesser extent, L-band SAR, for agriculture and hydrology. The potential of the former had been highlighted by several theoretical studies, but until now little empirical data was available to confirm them. Thanks to data from BELSAR, a campaign of simultaneous acquisition of airborne SAR and field data, several effects have been highlighted. The vegetation row structure effect, studied through the effect of the orientation of the planting rows relative to the SAR beam, has been shown to have a significant effect on SAR measurements. Yet, this effect is seldom taken into account in empirical studies, which generally employ very small datasets. The analysis also highlighted the capability of L-band SAR for monitoring high-biomass crops, and suggested that the bistatic configuration could provide additional information for retrieving crop biophysical variables, although this advantage might prove to be relatively marginal. Two recommendations can be drawn from these findings. First, particular attention must be paid to the effect of the planting structure in row crops when designing both studies and field campaigns, and particularly when the sample of parcels involved is small. Second, a multistatic SAR system with a short baseline, typically used for interferometric SAR applications, is unlikely to provide an advantage for crop monitoring on par with the resources required to launch a receiver-only satellite companion to in-orbit SAR systems. If a mission were to be designed for this purpose, a more interesting bistatic configuration would probably be to have the receiver in the plane orthogonal to the incidence plane, rather than in the backward scattering region (Guerriero et al., 2013; Zhang and Wu, 2016).

The second investigation, in Chapter 3, consisted in assessing the suitability of SAR data alone, i.e., independently of ancillary data such as field or optical measurements, for monitoring the GAI in maize crops. The study focused on the inversion of a relaxed version of the Water Cloud model (WCM), a simplified radiative transfer (RT)-based model widely used to model vegetation and soil backscatter, for the independent and then simultaneous retrieval of GAI and underlying soil moisture from dual-pol SAR data. The comparison of the model's performance in estimating the GAI with or without field data on soil moisture and with C-band data from Sentinel-1 (S1) or L-band data from BELSAR led to a number of insights. The first is that using dual-pol SAR dispenses with the need for auxiliary data, and could replace optical systems when they are lacking. Secondly, the ability of dual-pol SAR in L-band—in this case outperforming that in C-band—to monitor the evolution of a dense canopy such as maize, a crop where the C-band signal saturates early in the growing season (Bériaux et al., 2015; El Hajj et al., 2018), underlines the complementary nature of C- and L-bands for crop monitoring. The forthcoming launches of NISAR and ROSE-L, two L-band SARs, potentially offering freely-accessible global and systematic coverage with high revisit, open up exciting prospects on this matter. There are, however, two caveats to this picture. While encouraging results have been obtained, they proved to be not quite as accurate as those obtained using optical methods. In addition, the calibration of both the WCM and its relaxed version are non-convex optimization problems for which convergence to a global optimum cannot be guaranteed, and its inversion is an ill-posed problem. This results in a high degree of dependency in the quality and size of the usually experimental calibration dataset, and therefore in a low potential for transferability of the method. Substituting the semi-empirical model for a physics-based model, in an approach similar to PROSAIL inversion in the optical domain (Bacour et al., 2006; Duveiller et al., 2011), could solve the latter issue by overcoming the dependence of the method on the calibration data.

The third investigation, presented in Chapter 4, aimed to develop a method combining SAR and optical data to improve the temporal resolution of current crop monitoring methods. The goal was to use dense time series of C-band SAR data from S1 to solve the main problem of optical-based GAI monitoring, namely the presence of gaps in its time series generally due to the presence of clouds during satellite observation (Defourny et al., 2019). The idea behind this approach was that an imperfect reconstruction of a whole time series is always preferable to a perfect but sparse one. The emphasis was on retrieving new missing data as they come in, which has proven to be much more challenging then gap-filling past data. To achieve this, a transformer encoder has been implemented for its ability to model the highly complex relationship between GAI and SAR backscatter and understand the sequential nature of the values to be regressed. The method proved to be able to accurately fill gaps in the time series of otherwise accurate optically-derived GAI as they appeared throughout the growing season. The proposed method also went beyond interpolation, as it has proved to rely on SAR measurements enough for reacting appropriately to unexpected events hidden from optical sensors by persistent cloud cover. Although this study would appear to have produced a narrow solution to a technical problem, its implications could potentially become global. Indeed, to minimize the impact of clouds, many global agricultural monitoring systems use optical sensors with very short revisits to the detriment of their resolution. The method developed in this study, because it compensates for missing acquisitions, could enable the use sensors with longer revisit periods but much better resolutions, such as Sentinel-2 (S2), in their place. This could be especially valuable in regions where optical remote sensing is challenged by persistent cloud cover during the crop growing season, and where such data can be crucial for crop specific monitoring to ensure local food security. For these reasons, it would be highly desirable if further efforts were made to improve the method, by extending it to other crops, incorporating other data sources such as L-band SAR, and fine-tuning it, with the aim of eventually putting it into production to provide stakeholders with much needed timely and valuable information on crops regardless of cloud cover.

In summary, the value of SAR, and in particular multi-frequency SAR, for crop monitoring is clear, and the results of the research reported in this manuscript only reinforce this assertion. They demonstrate the capability of SAR in both L- and C-band for crop monitoring, and have led to the development of original methods for employing it in this role, alone or in conjunction with approaches based on the exploitation of optical remote sensing data. As for multistatic SAR, the exploration of the dataset from the BELSAR-Campaign has served as a valuable reminder that the suitability of the multistatic configuration for the intended application is crucial if it is to add value commensurate with the investment it requires. The remote sensing community, however, has yet to give SAR greater prominence in crop monitoring systems. The upcoming launches of NISAR and then ROSE-L—which is intended to share the same orbit, swath, and acquisition geometry as S1, effectively making it the first dual-frequency spaceborne SAR system of its kind—has the potential to make its use even more appealing in the near future. The time has come to prepare for it to play a more important role in agricultural monitoring, and to rely on it to provide essential information that is still lacking concerning food security, resource management, environmental conservation, and climate change adaptation.

5.2 Perspectives for future work

The work carried out to meet the main objective of this thesis, namely the improvement of GAI retrieval through SAR remote sensing for crop monitoring, could be extended in three major directions: (i) reconstructing entire time series of multiple optically-derived biophysical variables for all major rainfed crops using multi-frequency SAR; (ii) bridging the gap between the low supply of *in situ* data and the high demand of deep learning algorithms using physics-based models; and (iii) moving from parcel-based to pixel-based methods to monitor heterogeneous parcels and fragmented cropland.

5.2.1 Biophysical variable time series reconstruction

The method developed in Chapter 4 for gap-filling S2-derived GAI time series with SAR data from S1 provided useful results for maize in the Hesbaye region of Belgium. However, while these findings are encouraging, they only concern one biophysical variable, for a specific crop in a homogeneous region. To realize the full potential of this approach would certainly entail (i) extending it to other biophysical variables, such as the fraction of absorbed photosynthetically active radiation (fAPAR), the fraction of vegetation cover (fCover), and the canopy chlorophyll content (CCC); (ii) applying it to other major crops, in different climatic zones, and under a variety of management practices; (iii) transferring it to regions of the world where optical remote sensing is almost completely ineffective during the growing season, i.e., in tropical or monsoon climates.

The method has produced useful results for GAI retrieval, and algorithms already exist for retrieving the other above-mentioned biophysical variables from S2 images (Weiss et al., 2020a). Given that, like the GAI, all of them are related—though for some, only indirectly—to both vegetation geometry and water content (Inoue et al., 2014), the two main drivers of radar scattering in natural targets, it should be possible to use the same approach to retrieve them from joint SAR-optical data.

Regarding the second path for improvement, a highly interesting and practical area for extending the algorithm to other crops would be Europe, given the wide variety of agricultural practices and climatic zones that exist across the continent. Moreover, a number of EU member states have an open-access policy to their (anonymized) land parcel identification systems (Schneider et al., 2023). Large quantities of high-quality data could therefore be extracted and aggregated to form a very rich dataset for training the algorithm, provided substantial computing capacities are available.

Achieving this extension to several biophysical variables and crops would require to account for the major differences in surface and vegetation properties between various crops in different climates. It would therefore certainly be beneficial to integrate other data sources into the model to improve the information content of its features in case the sensitivity of C-band SAR is insufficient. In that case, while both X- and L-band SAR would be prime candidates for the role, given their complementarity to C-band, only the latter would be able to overcome the problem of signal saturation affecting higher-frequency sensors in high-biomass crops which constitutes one of the main blind spots of crop monitoring systems.

Finally, the current method can deliver timely estimates of a biophysical variable, GAI, by exploiting the all-weather capability of SAR. This is already a considerable improvement for monitoring crops in areas where gaps are common in optical time series. In some parts of the world, such as tropical and monsoon regions, however, cloud cover is so persistent during the crop-growing season that the quantity of optical images available to train deep-learning models is generally insufficient. To overcome this limitation, the model should be transferred, i.e., trained on sites with similar crops and cultivation practices, and then applied in areas where optical data are lacking. The results could be validated in several ways: by using data collected *in situ*, by increasing the number of cloud-free optical acquisitions with systems such as Planet, or by testing the transferability of the model on a similar area for which data are available, e.g., the Northern vs. the Southern cropland of Mali.

5.2.2 Physics-based data augmentation for deep learning

In the era of machine, and especially deep learning, data are the models. However, high-quality *in situ* data, in particular, continue to be a scarce resource. Their collection in sufficient number remains one of the biggest challenge facing the remote sensing community, as field measurements are labor-intensive, costly, and time-consuming. Moreover, sharing is still not common practice, although efforts to tackle the problem are regularly renewed. From experience designing and participating in field campaigns, and particularly with researchers from different cultural and scientific backgrounds in China, it is clear that, even when they are shared, it is difficult to make good use of data collected by others. Indeed, there can be wide discrepancies between the field collection protocol, the *in situ* data collection itself, and finally their use in models. These can present the modeler with two conflicting issues: a lack of confidence in the data and an unwarranted belief in their quality. The former can lead the modeler to question the quality of the field data, rather than that of his model when analyzing its results. Overconfidence, on the other hand, leads to the belief that these data are a perfect reflection of reality, which is equally detrimental to the analysis for the opposite reason.

Despite these limitations, *in situ* measurements are still at the basis of many approaches to the retrieval of biophysical variables, such as their use in the calibration of empirical or semi-empirical models, like the WCM described in Chapter 3. In addition to the sometimes prohibitive cost of collecting the data required for their fitting, the limited representativeness of the datasets on which these models are trained often means that they cannot be transferred to new locations without recalibration. Physics-based RT models, in comparison, describe the interactions of electromagnetic waves within crops using physical laws, thereby eliminating the need to collect new *in situ* data for transferring them. As such, they can be used to bridge the gap between the lack of quality *in situ* data, which are still necessary for at least adjusting and validating RT models, and the need for big data in deep learning approaches.

Multiple RT models exist that simulate the interactions of microwaves in the vegetation, e.g., Toure et al. (1994), Quast and Wagner (2016), and Bracaglia et al. (1995). The proposed approach calls for the articulation of these traditional physics-based models to state-of-the-art deep learning techniques—a rapidly growing field of research (Willard et al., 2022)—in a manner similar to the inversion of the PROSAIL model in the optical domain, e.g., Duveiller et al. (2011) and Delloye et al. (2018). The method would then consist in using an RT model to generate a synthetic dataset of simulated radar backscatter and corresponding GAI. A deep learning-based regressor would then learn from the data points generated by simulations to provide fast and, hopefully, accurate estimates of the GAI from actual SAR measurements.

The so-called Tor Vergata model is one of these few RT models available for simulating the microwave backscatter of agricultural fields (Bracaglia et al., 1995). It has already been used to retrieve the soil moisture under crops (Stamenković et al., 2015) and in grassland (Stamenkovic et al., 2017) from SAR data. The model accounts for both vegetation and soil. To represent the former, the model requires precise characterization of crop morphological parameters, such as leaf thickness, number of leaves and stems, and stem height, to which it is highly sensitive. Efforts have been devoted to fitting this model to the maize measured during the BELSAR airborne and field campaign, described in Chapter 2, but they remained unsuccessful because the right morphological measurements needed for the fine-tuning of the model were not available. These precise morphological measurements, because they do not directly reveal useful vegetation properties, are classically not collected in the field. To exploit the Tor Vergata model for GAI retrieval in an operational perspective would therefore require relatively advanced knowledge of phytomorphology for two purposes. First, to build a detailed mechanistic model of plant growth that relates the GAI to the physical parameters of the RT model in a variety of situations, i.e., different cultivars, agricultural practices, and climatic conditions, which could not realistically be captured empirically. Second, *a priori* knowledge of plant morphology would help restricting the ranges of model parameters and avoid unrealistic parameter combinations, thereby limiting the effects of the ill-posedness of the inverse problem (Verrelst et al., 2019).

5.2.3 Moving to pixel-based methods in fragmented cropland

While the increased availability of SAR data accompanied with new data-driven approaches provides unprecedented opportunities for crop monitoring, many current techniques remain ill-suited to certain landscapes due to speckle effect. The speckle effect is a disturbance inherent to all active coherent imaging systems (Argenti et al., 2013), often modeled as a signal-dependent multiplicative noise which degrades the radiometric quality of the images (Lee, 1981).

Throughout this thesis, the approach used to limit the impact of statistical uncertainties due to speckle for biophysical variable retrieval has been to adopt a parcel-based approach, which consists in averaging all the pixels on a parcel rather than considering them individually. However, this solution is not applicable when parcel boundaries are unknown, or when they are too small (or narrow) compared to the resolution of the sensor, resulting in noisy averages. Fragmented agricultural landscapes, apart from being sub-optimal from the point of view of food production and resource management (Wang, 2024; Cui et al., 2018), are therefore also an obstacle to crop monitoring using SAR remote sensing. Finally, for some applications, it is considered desirable to preserve intra-parcel heterogeneity right through to the final product, and it is therefore necessary not to discount local variations of pixel values.

A solution in the above cases would be to move from parcel-based to pixel-based methods. However, applying them directly to pixels would lead to noisy estimates of biophysical variables. In the case of large, homogeneous areas spread over several adjoining parcels or within a large parcel, the prior detection of these areas by clustering would enable the methods to be applied unchanged. For small plots, or areas with high spatial heterogeneity, the standard, albeit non-trivial, approach is to filter out speckle (Dalsasso et al., 2021). Speckle filters fall into two categories, spatial filters, e.g., Lee et al. (2008), and (multi-)temporal filters, e.g., Quegan et al. (2000). The former, applied to each image in a time series, preserve vegetation dynamics in exchange for smoothing out spatial variability. The latter favors the opposite. The choice of filter is therefore decisive for the expected result. At the beginning of the season, vegetation growth dynamics are of major importance, and a spatial filter would enable us to track them more effectively. From the mid-season on, on the other hand, biophysical variables evolve less rapidly, and a multi-temporal filter would enable us to preserve the local spatial variations necessary, for example, for the targeted application of fertilizer.

5.3 Final thoughts

Climate change and the rapid growth of the world population are putting the agricultural sector under ever increasing pressure. In this context, agricultural monitoring systems, and notably food security early warning systems, can no longer afford to depend on clear skies to gather crucial information on the state of crops. As a result, SAR remote sensing comes forth as the most promising way of collecting such data in a reliable and timely manner and in almost all meteorological conditions.

The research presented in this thesis is part of a collective endeavor towards a wider adoption of SAR remote sensing for crop monitoring. It has shown that the use of SAR, in the present state, can already improve the temporal resolution and the timeliness of current systems relying on optical data, and that multi-frequency SAR should play an increasingly important role in the next few years. This perspective will materialize thanks to the launch of ROSE-L, which, combined with S1, will set up the first multi-frequency SAR system to offer global and systematic coverage. These promising developments suggest that it is time for a change in the way crop monitoring systems are designed, and that further efforts should be made to integrate SAR remote sensing, either as a complement or entirely on its own, into current operational systems.

Bibliography

Allies, Aubin, Antoine Roumiguié, Jean-François Dejoux, Rémy Fieuzal, Anne Jacquin, Amanda Veloso, Luc Champolivier, and Frédéric Baup (2021). "Evaluation of Multiorbital SAR and Multisensor Optical Data for Empirical Estimation of Rapeseed Biophysical Parameters". In: *IEEE Journal of Selected Topics in Applied Earth Observations and Remote Sensing* 14, pp. 7268–7283. DOI: 10.1109/JSTARS.2021.3095537.

Amin, Eatidal, Jochem Verrelst, JP Rivera-Caicedo, Nieves Pasqualotto, Jesús Delegido, A Ruiz Verdú, and J Moreno (2018). "The Sensagri Sentinel-2 Lai Green and Brown product: from algorithm development towards operational mapping". In: *IGARSS 2018-2018 IEEE International Geoscience and Remote Sensing Symposium*. IEEE, pp. 1822–1825. DOI: 10.1109/IGARSS.2018.8518938.

Amin, Eatidal, Jochem Verrelst, Juan Pablo Rivera-Caicedo, Luca Pipia, Antonio Ruiz-Verdú, and José Moreno (2021). "Prototyping Sentinel-2 green LAI and brown LAI products for cropland monitoring". In: *Remote Sensing of Environment* 255, p. 112168. DOI: 10.1016/j.rse.2020.112168.

Antoniadis, Anestis, Sophie Lambert-Lacroix, and Jean-Michel Poggi (2021). "Random forests for global sensitivity analysis: A selective review". In: *Reliability Engineering & System Safety* 206, p. 107312. DOI: 10.1016/j.ress.2020.107312.

Araujo Picoli, Michelle Cristina, Rubens Augusto Camargo Lamparelli, Edson Eyji Sano, Jefferson Rodrigo Batista de Mello, and Jansle Vieira Rocha (2013). "Effect of sugarcane-planting row directions on ALOS/PALSAR satellite images". In: *GIScience & Remote Sensing* 50.3, pp. 349–357. DOI: 10.1080/15481603.2013.808457.

Argenti, Fabrizio, Alessandro Lapini, Tiziano Bianchi, and Luciano Alparone (2013). "A tutorial on speckle reduction in synthetic aperture radar images". In: *IEEE Geoscience and remote sensing magazine* 1.3, pp. 6–35. DOI: 10.1109/MGRS.2013.2277512.

Attema, EPW and Fawwaz T Ulaby (1978). “Vegetation modeled as a water cloud”. In: *Radio science* 13.2, pp. 357–364. DOI: 10.1029/RS013i002p00357.

Babaeian, Ebrahim, Morteza Sadeghi, Trenton E Franz, Scott Jones, and Markus Tuller (2018). “Mapping soil moisture with the OPtical TRApezoid Model (OPTRAM) based on long-term MODIS observations”. In: *Remote sensing of environment* 211, pp. 425–440. DOI: 10.1016/j.rse.2018.04.029.

Bacour, C, F Baret, D Béal, M Weiss, and K Pavageau (2006). “Neural network estimation of LAI, fAPAR, fCover and LAI× Cab, from top of canopy MERIS reflectance data: Principles and validation”. In: *Remote sensing of environment* 105.4, pp. 313–325. DOI: 10.1016/j.rse.2006.07.014.

Baghdadi, Nicolas, Mohammad El Hajj, Mehrez Zribi, and Safa Bousbih (2017). “Calibration of the water cloud model at C-band for winter crop fields and grasslands”. In: *Remote Sensing* 9.9, p. 969. DOI: 10.3390/rs9090969.

Baghdadi, Nicolas N, Mohamad El Hajj, Mehrez Zribi, and Ibrahim Fayad (2015). “Coupling SAR C-band and optical data for soil moisture and leaf area index retrieval over irrigated grasslands”. In: *IEEE Journal of Selected Topics in Applied Earth Observations and Remote Sensing* 9.3, pp. 1229–1243. DOI: 10.1109/JSTARS.2015.2464698.

Balenzano, Anna, Francesco Mattia, Giuseppe Satalino, and Malcolm WJ Davidson (2010). “Dense temporal series of C-and L-band SAR data for soil moisture retrieval over agricultural crops”. In: *IEEE Journal of Selected Topics in Applied Earth Observations and Remote Sensing* 4.2, pp. 439–450. DOI: 10.1109/JSTARS.2010.2052916.

Becker-Reshef, Inbal, Christina Justice, Brian Barker, Michael Humber, Felix Rembold, Rogerio Bonifacio, Mario Zappacosta, Mike Budde, Tamuka Magadzire, Chris Shitote, et al. (2020). “Strengthening agricultural decisions in countries at risk of food insecurity: The GEOGLAM Crop Monitor for Early Warning”. In: *Remote Sensing of Environment* 237, p. 111553. DOI: 10.1016/j.rse.2019.111553.

BelSAR Data Acquisition Report (Jan. 2019). Tech. rep. RP-CSL-BEL-18006. Centre spatial de Liège.

Beriaux, Emilie, Cozmin Lucau-Danila, Eric Auquiere, and Pierre Defourny (2013). “Multiyear independent validation of the water cloud model for retrieving maize leaf area index from SAR time series". In: *International Journal of Remote Sensing* 34.12, pp. 4156–4181. DOI: 10.1080/01431161.2013.772676.

Bériaux, Emilie, Sébastien Lambot, and Pierre Defourny (2011). "Estimating surface-soil moisture for retrieving maize leaf-area index from SAR data". In: *Canadian Journal of Remote Sensing* 37.1, pp. 136–150. DOI: 10.5589/m11-021.

Bériaux, Emilie, François Waldner, François Collienne, Patrick Bogaert, and Pierre Defourny (2015). "Maize leaf area index retrieval from synthetic quad pol SAR time series using the water cloud model". In: *Remote Sensing* 7.12, pp. 16204–16225. DOI: 10.3390/rs71215818.

Bhogapurapu, Narayanarao, Subhadip Dey, Dipankar Mandal, Avik Bhattacharya, L Karthikeyan, Heather McNairn, and YS Rao (2022). "Soil moisture retrieval over croplands using dual-pol L-band GRD SAR data". In: *Remote Sensing of Environment* 271, p. 112900. DOI: 10.1016/j.rse.2022.112900.

Blaes, Xavier, Pierre Defourny, U Wegmuller, Andrea Della Vecchia, Leila Guerriero, and Paolo Ferrazzoli (2006). "C-band polarimetric indexes for maize monitoring based on a validated radiative transfer model". In: *IEEE transactions on geoscience and remote sensing* 44.4, pp. 791–800. DOI: 10.1109/TGRS.2005.860969.

Bouchat, Jean, Quentin Deffense, Thomas De Maet, and Pierre Defourny (in prep.). "Joint use of optical and SAR imagery for near real-time green area index retrieval in maize".

Bouchat, Jean, Emma Tronquo, Anne Orban, Karlus A C de Macedo, Malcolm Davidson, Niko EC Verhoest, and Pierre Defourny (2024). "The BELSAR dataset: Mono-and bistatic full-pol L-band SAR for agriculture and hydrology". In: *Scientific Data* 11.1, p. 513. DOI: 10.1038/s41597-024-03320-1.

Bouchat, Jean, Emma Tronquo, Anne Orban, Xavier Neyt, Niko EC Verhoest, and Pierre Defourny (2022a). "Green Area Index and Soil Moisture Retrieval in Maize Fields Using Multi-Polarized C-and L-Band SAR Data and the Water Cloud Model". In: *Remote Sensing* 14.10, p. 2496. DOI: 10.3390/rs14102496.

Bouchat, Jean, Emma Tronquo, Anne Orban, Niko EC Verhoest, and Pierre Defourny (2022b). "Assessing the Potential of Fully Polarimetric Mono-and Bistatic SAR Acquisitions in L-band for Crop and Soil

Monitoring". In: *IEEE Journal of Selected Topics in Applied Earth Observations and Remote Sensing* 15, pp. 3168–3178. DOI: 10.1109/JSTARS.2022.3162911.

Bracaglia, M, P Ferrazzoli, and L Guerriero (1995). "A fully polarimetric multiple scattering model for crops". In: *Remote Sensing of Environment* 54.3, pp. 170–179. DOI: 10.1016/0034-4257(95)00151-4.

Breiman, Leo (2001). "Random forests". In: *Machine learning* 45.1, pp. 5–32. DOI: 10.1023/A:1010933404324.

Brogioni, Marco, Simone Pettinato, Giovanni Macelloni, Simonetta Paloscia, Paolo Pampaloni, Nazzareno Pierdicca, and Francesca Ticconi (2010). "Sensitivity of bistatic scattering to soil moisture and surface roughness of bare soils". In: *International Journal of Remote Sensing* 31.15, pp. 4227–4255. DOI: 10.1080/01431160903232808.

Chauhan, Sugandh, Hari Shanker Srivastava, and Parul Patel (2018). "Wheat crop biophysical parameters retrieval using hybrid-polarized RISAT-1 SAR data". In: *Remote sensing of environment* 216, pp. 28–43. DOI: 10.1016/j.rse.2018.06.014.

Chen, Jing M and TA Black (1992). "Defining leaf area index for non-flat leaves". In: *Plant, Cell & Environment* 15.4, pp. 421–429. DOI: 10.1111/j.1365-3040.1992.tb00992.x.

Chen, Kun-Shan, Tzong-Dar Wu, Leung Tsang, Qin Li, Jiancheng Shi, and Adrian K Fung (2003). "Emission of rough surfaces calculated by the integral equation method with comparison to three-dimensional moment method simulations". In: *IEEE Transactions on Geoscience and Remote Sensing* 41.1, pp. 90–101. DOI: 10.1109/TGRS.2002.807587.

Cho, Kyunghyun, Bart Van Merriënboer, Caglar Gulcehre, Dzmitry Bahdanau, Fethi Bougares, Holger Schwenk, and Yoshua Bengio (2014). "Learning phrase representations using RNN encoder-decoder for statistical machine translation". In: *arXiv preprint arXiv:1406.1078*. DOI: 10.48550/arXiv.1406.1078.

Clevers, Jan GPW, Lammert Kooistra, and Marnix MM Van den Brande (2017). "Using Sentinel-2 data for retrieving LAI and leaf and canopy chlorophyll content of a potato crop". In: *Remote Sensing* 9.5, p. 405. DOI: 10.3390/rs9050405.

Copernicus Data Space Ecosystem (2024). URL: https://dataspace.copernicus.eu/ (visited on 03/13/2024).

Craswell, Eric (2021). "Fertilizers and nitrate pollution of surface and ground water: an increasingly pervasive global problem". In: *SN Applied Sciences* 3.4, p. 518. DOI: 10.1007/s42452-021-04521-8.

Cui, Zhenling, Hongyan Zhang, Xinping Chen, Chaochun Zhang, Wenqi Ma, Chengdong Huang, Weifeng Zhang, Guohua Mi, Yuxin Miao, Xiaolin Li, et al. (2018). "Pursuing sustainable productivity with millions of smallholder farmers". In: *Nature* 555.7696, pp. 363–366. DOI: 10.1038/nature25785.

Dalsasso, Emanuele, Loïc Denis, and Florence Tupin (2021). "How to handle spatial correlations in SAR despeckling? Resampling strategies and deep learning approaches". In: *EUSAR 2021; 13th European Conference on Synthetic Aperture Radar*. VDE, pp. 1–6.

Davidson, Eric A (2009). "The contribution of manure and fertilizer nitrogen to atmospheric nitrous oxide since 1860". In: *Nature Geoscience* 2.9, pp. 659–662. DOI: 10.1038/ngeo608.

Davidson, Malcolm WJ, Francesco Mattia, Giuseppe Satalino, Niko EC Verhoest, Thuy Le Toan, Maurice Borgeaud, Jérôme MB Louis, and Evert Attema (2003). "Joint statistical properties of RMS height and correlation length derived from multisite 1-m roughness measurements". In: *IEEE Transactions on Geoscience and Remote Sensing* 41.7, pp. 1651–1658. DOI: 10.1109/TGRS.2003.813361.

De Peppo, Margherita, Andrea Taramelli, Mirco Boschetti, Alberto Mantino, Iride Volpi, Federico Filipponi, Antonella Tornato, Emiliana Valentini, and Giorgio Ragaglini (2021). "Non-Parametric statistical approaches for leaf area index estimation from Sentinel-2 Data: A multicrop assessment". In: *Remote Sensing* 13.14, p. 2841. DOI: 10.3390/rs13142841.

Defourny, Pierre, Sophie Bontemps, Nicolas Bellemans, Cosmin Cara, Gérard Dedieu, Eric Guzzonato, Olivier Hagolle, Jordi Inglada, Laurentiu Nicola, Thierry Rabaute, et al. (2019). "Near real-time agriculture monitoring at national scale at parcel resolution: Performance assessment of the Sen2-Agri automated system in various cropping systems around the world". In: *Remote sensing of environment* 221, pp. 551–568. DOI: 10.1016/j.rse.2018.11.007.

Delegido, Jesús, Jochem Verrelst, Juan P Rivera, Antonio Ruiz-Verdú, and José Moreno (2015). "Brown and green LAI mapping through spectral indices". In: *International Journal of Applied Earth Obser-*

vation and Geoinformation 35, pp. 350–358. DOI: 10.1016/j.jag.2014.10.001.

Della Vecchia, A (2006). “Advances in modeling microwave interactions with vegetation for active and passive remote sensing”. PhD thesis. Ph. D. Thesis, Doctorate in Geoinformation, Tor Vergata University, Rome.

Della Vecchia, Andrea, Paolo Ferrazzoli, Leila Guerriero, Xavier Blaes, Pierre Defourny, Laura Dente, Francesco Mattia, Giuseppe Satalino, Tazio Strozzi, and U Wegmuller (2006a). “Influence of geometrical factors on crop backscattering at C-band”. In: *IEEE transactions on geoscience and remote sensing* 44.4, pp. 778–790. DOI: 10.1109/TGRS.2005.860489.

Della Vecchia, Andrea, Paolo Ferrazzoli, Leila Guerriero, I Cacucci, M Marzano, Nazzareno Pierdicca, and Francesca Ticconi (2006b). “Optimization of bistatic radar configurations for vegetation monitoring”. In: *2006 IEEE International Symposium on Geoscience and Remote Sensing*. IEEE, pp. 1220–1223. DOI: 10.1109/IGARSS.2006.315.

Delloye, Cindy, Marie Weiss, and Pierre Defourny (2018). “Retrieval of the canopy chlorophyll content from Sentinel-2 spectral bands to estimate nitrogen uptake in intensive winter wheat cropping systems”. In: *Remote Sensing of Environment* 216, pp. 245–261. DOI: 10.1016/j.rse.2018.06.037.

Duveiller, Grégory, Frédéric Baret, and Pierre Defourny (2012). “Remotely sensed green area index for winter wheat crop monitoring: 10-Year assessment at regional scale over a fragmented landscape”. In: *Agricultural and forest meteorology* 166, pp. 156–168. DOI: 10.1016/j.agrformet.2012.07.014.

Duveiller, Grégory, Marie Weiss, Frédéric Baret, and Pierre Defourny (2011). “Retrieving wheat Green Area Index during the growing season from optical time series measurements based on neural network radiative transfer inversion”. In: *Remote sensing of environment* 115.3, pp. 887–896. DOI: 10.1016/j.rse.2010.11.016.

EARSC, European Association of Remote Sensing Companies (2023). *EARSC Industry Survey 2023*. Brussels, Belgium. 28 pp. URL: https://earsc.org/3d-flip-book/earsc-industry-survey-2023/ (visited on 05/28/2024).

Efremova, Natalia, Mohamed El Amine Seddik, and Esra Erten (2022). "Soil moisture estimation using Sentinel-1/-2 imagery coupled with cycleGAN for time-series gap filing". In: *IEEE Transactions on Geoscience and Remote Sensing* 60, pp. 1–11. DOI: 10.1109/TGRS.2021.3134127.

Egido, Alejandro, Marco Caparrini, Giulio Ruffini, Simonetta Paloscia, Emanuele Santi, Leila Guerriero, Nazzareno Pierdicca, and Nicolas Floury (2012). "Global navigation satellite systems reflectometry as a remote sensing tool for agriculture". In: *Remote Sensing* 4.8, pp. 2356–2372. DOI: 10.3390/rs4082356.

El Hajj, Mohammad, Nicolas Baghdadi, Hassan Bazzi, and Mehrez Zribi (2018). "Penetration analysis of SAR signals in the C and L bands for wheat, maize, and grasslands". In: *Remote Sensing* 11.1, p. 31. DOI: 10.3390/rs11010031.

Eros, U (2015). "USGS EROS Archive—Digital Elevation—Shuttle Radar Topography Mission (SRTM) 1 Arc-Second Global". In: *US Geological Survey: Reston, VA, USA*. DOI: 10.5066/F7PR7TFT.

Fang, Hongliang, Frederic Baret, Stephen Plummer, and Gabriela Schaepman-Strub (2019). "An overview of global leaf area index (LAI): Methods, products, validation, and applications". In: *Reviews of Geophysics* 57.3, pp. 739–799. DOI: 10.1029/2018RG000608.

Ferrazzoli, Paolo, Leila Guerriero, Claudia Ingafú Del Monaco, and Domenico Solimini (2003). "A further insight into the potential of bistatic SAR in monitoring the earth surface". In: *IGARSS 2003. 2003 IEEE International Geoscience and Remote Sensing Symposium. Proceedings (IEEE Cat. No. 03CH37477)*. Vol. 2. IEEE, pp. 776–777. DOI: 10.1109/IGARSS.2003.1293914.

Ferrazzoli, Paolo, J-P Wigneron, Leila Guerriero, and André Chanzy (2000). "Multifrequency emission of wheat: Modeling and applications". In: *IEEE Transactions on Geoscience and Remote Sensing* 38.6, pp. 2598–2607. DOI: 10.1109/36.885206.

Fieuzal, R and F Baup (2016). "Estimation of leaf area index and crop height of sunflowers using multi-temporal optical and SAR satellite data". In: *International Journal of Remote Sensing* 37.12, pp. 2780–2809. DOI: 10.1080/01431161.2016.1176276.

Fore, Alexander G, Bruce D Chapman, Brian P Hawkins, Scott Hensley, Cathleen E Jones, Thierry R Michel, and Ronald J Muellerschoen

(2015). “UAVSAR polarimetric calibration”. In: *IEEE Transactions on Geoscience and Remote Sensing* 53.6, pp. 3481–3491. DOI: 10.1109/TGRS.2014.2377637.

Fritz, Steffen, Linda See, Juan Carlos Laso Bayas, François Waldner, Damien Jacques, Inbal Becker-Reshef, Alyssa Whitcraft, Bettina Baruth, Rogerio Bonifacio, Jim Crutchfield, et al. (2019). “A comparison of global agricultural monitoring systems and current gaps”. In: *Agricultural systems* 168, pp. 258–272. DOI: 10.1016/j.agsy.2018.05.010.

Fung, Adrian K (1994). *Microwave scattering and emission models and their applications*. Artech House.

Fung, Adrian K, Zongqian Li, and Kun-Shan Chen (1992). “Backscattering from a randomly rough dielectric surface”. In: *IEEE Transactions on Geoscience and remote sensing* 30.2, pp. 356–369. DOI: 10.1109/36.134085.

Garioud, Anatol, Silvia Valero, Sébastien Giordano, and Clément Mallet (2020). “On the joint exploitation of optical and SAR satellite imagery for grassland monitoring”. In: *The International Archives of the Photogrammetry, Remote Sensing and Spatial Information Sciences* 43, pp. 591–598. DOI: 10.5194/isprs-archives-XLIII-B3-2020-591-2020.

Gebert, Nicolas, Bernardo Carnicero Dominguez, Malcolm WJ Davidson, Marina Diaz Martin, and Pierluigi Silvestrin (2014). “SAOCOM-CS-A passive companion to SAOCOM for single-pass L-band SAR interferometry”. In: *EUSAR 2014; 10th European Conference on Synthetic Aperture Radar*. VDE, pp. 1–4.

Gherboudj, Imen, Ramata Magagi, Aaron A Berg, and Brenda Toth (2011). “Soil moisture retrieval over agricultural fields from multi-polarized and multi-angular RADARSAT-2 SAR data”. In: *Remote sensing of environment* 115.1, pp. 33–43. DOI: 10.1016/j.rse.2010.07.011.

Guerriero, Leila, Nazzareno Pierdicca, Luca Pulvirenti, and Paolo Ferrazzoli (2013). “Use of satellite radar bistatic measurements for crop monitoring: A simulation study on corn fields”. In: *Remote Sensing* 5.2, pp. 864–890. DOI: 10.3390/rs5020864.

Hochreiter, Sepp, Yoshua Bengio, Paolo Frasconi, Jürgen Schmidhuber, et al. (2001). “Gradient Flow in Recurrent Nets: The Difficulty of Learning LongTerm Dependencies”. In: *A Field Guide to Dynamical*

Recurrent Networks. IEEE Press In, pp. 237–243. DOI: 10.1109/9780470544037.ch14.

Hosseini, Mehdi and Heather McNairn (2017). "Using multi-polarization C-and L-band synthetic aperture radar to estimate biomass and soil moisture of wheat fields". In: *International journal of applied earth observation and geoinformation* 58, pp. 50–64. DOI: 10.1016/j.jag.2017.01.006.

Hosseini, Mehdi, Heather McNairn, Amine Merzouki, and Anna Pacheco (2015). "Estimation of Leaf Area Index (LAI) in corn and soybeans using multi-polarization C-and L-band radar data". In: *Remote Sensing of Environment* 170, pp. 77–89. DOI: 10.1016/j.rse.2015.09.002.

Hosseini, Mehdi, Heather McNairn, Scott Mitchell, Laura Dingle Robertson, Andrew Davidson, Nima Ahmadian, Avik Bhattacharya, Erik Borg, Christopher Conrad, Katarzyna Dabrowska-Zielinska, et al. (2021). "A comparison between support vector machine and water cloud model for estimating crop leaf area index". In: *Remote Sensing* 13.7, p. 1348. DOI: 10.3390/rs13071348.

Hosseini, Mehdi, Heather McNairn, Scott Mitchell, Laura Dingle Robertson, Andrew Davidson, and Saeid Homayouni (2019). "Synthetic aperture radar and optical satellite data for estimating the biomass of corn". In: *International Journal of Applied Earth Observation and Geoinformation* 83, p. 101933. DOI: 10.1016/j.jag.2019.101933.

Hosseini, Mehdi, Heather McNairn, Laura Dingle Robertson, Jiao Xianfeng, Amine Merzouki, Andrew Davidson, and Scott Mitchell (2018). *Soil Moisture and Vegetation Measurement Guideline*. Tech. rep. Joint Experiment for Crop Assessment and Monitoring (JECAM). URL: http://jecam.org/wp-content/uploads/2018/07/Ground_Measurement_Guideline_AAFC_2018.pdf (visited on 03/22/2024).

Inoue, Yoshio, Eiji Sakaiya, and Cuizhen Wang (2014). "Capability of C-band backscattering coefficients from high-resolution satellite SAR sensors to assess biophysical variables in paddy rice". In: *Remote Sensing of Environment* 140, pp. 257–266. DOI: 10.1016/j.rse.2013.09.001.

Jiao, Xianfeng, Heather McNairn, Jiali Shang, and Jiangui Liu (2010). "The sensitivity of multi-frequency (X, C and L-band) radar backscatter signatures to bio-physical variables (LAI) over corn and soybean fields". In: *ISPRS TC VII Symposium—100 Years ISPRS*, pp. 317–325.

Jiao, Xianfeng, Heather McNairn, Jiali Shang, Elizabeth Pattey, Jiangui Liu, and Catherine Champagne (2011). "The sensitivity of RADARSAT-2 polarimetric SAR data to corn and soybean leaf area index". In: *Canadian Journal of Remote Sensing* 37.1, pp. 69–81. DOI: 10.5589/m11-023.

Johnson, Joel T and Jeffrey D Ouellette (2013). "Polarization features in bistatic scattering from rough surfaces". In: *IEEE Transactions on Geoscience and Remote Sensing* 52.3, pp. 1616–1626. DOI: 10.1109/TGRS.2013.2252909.

Karam, Mostafa A, Adrian K Fung, Roger H Lang, and Narinder S Chauhan (1992). "A microwave scattering model for layered vegetation". In: *IEEE Transactions on Geoscience and Remote Sensing* 30.4, pp. 767–784. DOI: 10.1109/36.158872.

Karthikeyan, L, Ming Pan, Niko Wanders, D Nagesh Kumar, and Eric F Wood (2017). "Four decades of microwave satellite soil moisture observations: Part 1. A review of retrieval algorithms". In: *Advances in Water Resources* 109, pp. 106–120. DOI: j.advwatres.2017.09.006.

Kelley, Carl T (1999). *Iterative methods for optimization*. SIAM. DOI: 10.1137/1.9781611970920.

Khabbazan, Saeed, Paul Vermunt, Susan Steele-Dunne, Lexy Ratering Arntz, Caterina Marinetti, Dirk van der Valk, Lorenzo Iannini, Ramses Molijn, Kees Westerdijk, and Corné van der Sande (2019). "Crop monitoring using Sentinel-1 data: A case study from The Netherlands". In: *Remote Sensing* 11.16, p. 1887. DOI: 10.3390/rs11161887.

Kim, Yunjin and Jakob J Van Zyl (2009). "A time-series approach to estimate soil moisture using polarimetric radar data". In: *IEEE Transactions on Geoscience and Remote Sensing* 47.8, pp. 2519–2527. DOI: 10.1109/TGRS.2009.2014944.

King, Michael D, Steven Platnick, W Paul Menzel, Steven A Ackerman, and Paul A Hubanks (2013). "Spatial and temporal distribution of clouds observed by MODIS onboard the Terra and Aqua satellites". In: *IEEE transactions on geoscience and remote sensing* 51.7, pp. 3826–3852. DOI: 0.1109/TGRS.2012.2227333.

Konings, Alexandra G, Maria Piles, Narendra Das, and Dara Entekhabi (2017). "L-band vegetation optical depth and effective scattering albedo estimation from SMAP". In: *Remote Sensing of Environment* 198, pp. 460–470. DOI: 10.1016/j.rse.2017.06.037.

Kulkarni, Samadhan C and Priti P Rege (2020). "Pixel level fusion techniques for SAR and optical images: A review". In: *Information Fusion* 59, pp. 13–29. DOI: 10.1016/j.inffus.2020.01.003.

Lal, Rattan (2015). "Restoring soil quality to mitigate soil degradation". In: *Sustainability* 7.5, pp. 5875–5895. DOI: 10.3390/su7055875.

Lee, Jong-Sen (1981). "Speckle analysis and smoothing of synthetic aperture radar images". In: *Computer graphics and image processing* 17.1, pp. 24–32. DOI: 10.1016/S0146-664X(81)80005-6.

Lee, Jong-Sen, Jen-Hung Wen, Thomas L Ainsworth, Kun-Shan Chen, and Abel J Chen (2008). "Improved sigma filter for speckle filtering of SAR imagery". In: *IEEE Transactions on Geoscience and Remote Sensing* 47.1, pp. 202–213. DOI: 10.1109/TGRS.2008.2002881.

Leeuwen, Hans van (1996). "Methodology for combining optical and microwave remote sensing in agricultural crop monitoring: The sugar beet crop as special case". PhD thesis. Wageningen University and Research.

Li, Jingbo, Changchun Li, Weimeng Xu, Haikuan Feng, Fa Zhao, Huiling Long, Yang Meng, Weinan Chen, Hao Yang, and Guijun Yang (2022). "Fusion of optical and SAR images based on deep learning to reconstruct vegetation NDVI time series in cloud-prone regions". In: *International Journal of Applied Earth Observation and Geoinformation* 112, p. 102818. DOI: 10.1016/j.jag.2022.102818.

Lievens, Hans and Niko EC Verhoest (2011). "On the retrieval of soil moisture in wheat fields from L-band SAR based on water cloud modeling, the IEM, and effective roughness parameters". In: *IEEE Geoscience and remote sensing Letters* 8.4, pp. 740–744. DOI: 10.1109/LGRS.2011.2106109.

Liu, Chang-an, Zhong-Xin Chen, SHAO Yun, Jin-song Chen, Tuya Hasi, and Hai-zhu PAN (2019). "Research advances of SAR remote sensing for agriculture applications: A review". In: *Journal of integrative agriculture* 18.3, pp. 506–525. DOI: 10.1016/S2095-3119(18)62016-7.

Liu, Chenzhou and Jiancheng Shi (2016). "Estimation of vegetation parameters of water cloud model for global soil moisture retrieval using time-series L-band Aquarius observations". In: *IEEE Journal of Selected Topics in Applied Earth Observations and Remote Sensing* 9.12, pp. 5621–5633. DOI: 10.1109/JSTARS.2016.2596541.

Liu, Jiangui, Elizabeth Pattey, and Stuart Admiral (2013). "Assessment of in situ crop LAI measurement using unidirectional view digital photography". In: *Agricultural and Forest Meteorology* 169, pp. 25–34. DOI: 10.1016/j.agrformet.2012.10.009.

Liu, Ying, Jiaxin Qian, and Hui Yue (2020). "Combined Sentinel-1A with Sentinel-2A to estimate soil moisture in farmland". In: *IEEE Journal of Selected Topics in Applied Earth Observations and Remote Sensing* 14, pp. 1292–1310. DOI: 10.1109/JSTARS.2020.3043628.

Macedo, Karlus A Camara de, Simone Placidi, and Adriano Meta (2019). "Bistatic and Monostatic InSAR Results with the MetaSensing Airborne SAR System". In: *2019 6th Asia-Pacific Conference on Synthetic Aperture Radar (APSAR)*. IEEE, pp. 1–5. DOI: 10.1109/APSAR46974.2019.9048392.

Macelloni, Giovanni, Simonetta Paloscia, Paolo Pampaloni, Filippo Marliani, and Marco Gai (2001). "The relationship between the backscattering coefficient and the biomass of narrow and broad leaf crops". In: *IEEE Transactions on Geoscience and Remote Sensing* 39.4, pp. 873–884. DOI: 10.1109/36.917914.

Mahowald, Natalie, Fiona Lo, Yun Zheng, Laura Harrison, Chris Funk, Danica Lombardozzi, and Christine Goodale (2016). "Projections of leaf area index in earth system models". In: *Earth System Dynamics* 7.1, pp. 211–229. DOI: 10.5194/esd-7-211-2016.

MAJA – The Multi-Temporal Cloud Screening and Atmospheric Correction Software v4.5.4 (2022). Version 4.5.4. URL: https://www.cesbio.cnrs.fr/maja/ (visited on 03/24/2024).

Mandal, Dipankar, Mehdi Hosseini, Heather McNairn, Vineet Kumar, Avik Bhattacharya, YS Rao, Scott Mitchell, Laura Dingle Robertson, Andrew Davidson, and Katarzyna Dabrowska-Zielinska (2019). "An investigation of inversion methodologies to retrieve the leaf area index of corn from C-band SAR data". In: *International Journal of Applied Earth Observation and Geoinformation* 82, p. 101893. DOI: 10.1016/j.jag.2019.06.003.

Mastro, Pietro, Margherita De Peppo, Alberto Crema, Mirco Boschetti, and Antonio Pepe (2023). "Statistical characterization and exploitation of Synthetic Aperture radar vegetation indexes for the generation of Leaf area Index time series". In: *International Journal of Applied Earth Observation and Geoinformation* 124, p. 103498. DOI: 10.1016/j.jag.2023.103498.

McNairn, Heather and Jiali Shang (Nov. 2016). "A Review of Multitemporal Synthetic Aperture Radar (SAR) for Crop Monitoring". In: Cham: Springer International Publishing, pp. 317–340. ISBN: 978-3-319-47035-1. DOI: 10.1007/978-3-319-47037-5_15.

McNairn, Heather, Jiali Shang, Xianfeng Jiao, and Catherine Champagne (2009). "The contribution of ALOS PALSAR multipolarization and polarimetric data to crop classification". In: *IEEE Transactions on Geoscience and Remote Sensing* 47.12, pp. 3981–3992. DOI: 10.1109/TGRS.2009.2026052.

Meier, Uwe (1997). *Growth stages of mono-and dicotyledonous plants*. Blackwell Wissenschafts-Verlag.

MetaSAR-L NetCDF File Format Description (July 2019). Tech. rep. MS-CSL-BEL-FFD-002-13. MetaSensing BV.

Millard, Koreen and Murray Richardson (2018). "Quantifying the relative contributions of vegetation and soil moisture conditions to polarimetric C-Band SAR response in a temperate peatland". In: *Remote sensing of environment* 206, pp. 123–138. DOI: 10.1016/j.rse.2017.12.011.

Moré, Jorge J (1978). "The Levenberg-Marquardt algorithm: implementation and theory". In: *Numerical analysis*. Springer, pp. 105–116. DOI: 10.1007/BFb0067700.

Nash, Stephen G (1984). "Newton-type minimization via the Lanczos method". In: *SIAM Journal on Numerical Analysis* 21.4, pp. 770–788. DOI: 10.1137/0721052.

Nasirzadehdizaji, Rouhollah, Fusun Balik Sanli, Saygin Abdikan, Ziyadin Cakir, Aliihsan Sekertekin, and Mustafa Ustuner (2019). "Sensitivity analysis of multi-temporal Sentinel-1 SAR parameters to crop height and canopy coverage". In: *Applied Sciences* 9.4, p. 655. DOI: 10.3390/app9040655.

OECD and FAO (2023). *OECD-FAO Agricultural Outlook 2023-2032*. Organisation for Economic Co-operation and Development (OECD) and Food and Agriculture Organization of the United Nations (FAO), p. 359. DOI: 10.1787/08801ab7-en.

Oh, Yisok, Kamal Sarabandi, Fawwaz T Ulaby, et al. (1992). "An empirical model and an inversion technique for radar scattering from bare soil surfaces". In: *IEEE transactions on Geoscience and Remote Sensing* 30.2, pp. 370–381. DOI: 10.1109/36.134086.

Orban, Anne, Denis Defrere, and Christian Barbier (2021). "BelSAR: the first Belgian airborne campaign for L-band, full polarimetric bistatic and interferometric SAR acquisitions over an agricultural site in Belgium". In: *EUSAR 2021; 13th European Conference on Synthetic Aperture Radar*. VDE, pp. 1–4.

Pampaloni, Paolo and Simonetta Paloscia (1986). "Microwave emission and plant water content: A comparison between field measurements and theory". In: *IEEE Transactions on Geoscience and Remote Sensing* 6, pp. 900–905. DOI: 10.1109/TGRS.1986.289705.

Parag, Mikka, Romano Lottering, Kabir Peerbhay, Naeem Agjee, and Nitesh Poona (2023). "The use of synthetic aperture radar technology for crop biomass monitoring: a systematic review". In: *Remote Sensing Applications: Society and Environment*, p. 101107. DOI: 10.1016/j.rsase.2023.101107.

Park, Sang-Eun, Yoon Taek Jung, Jae-Hyoung Cho, Hyoi Moon, and Seung-hoon Han (2019). "Theoretical evaluation of water cloud model vegetation parameters". In: *Remote Sensing* 11.8, p. 894. DOI: 10.3390/rs11080894.

Peng, Xingshuo, Wenting Han, Jianyi Ao, and Yi Wang (2021). "Assimilation of LAI Derived from UAV Multispectral Data into the SAFY Model to Estimate Maize Yield". In: *Remote Sensing* 13.6, p. 1094. DOI: 10.3390/rs13061094.

Pierdicca, Nazzareno, Marco Brogioni, Fabio Fascetti, Jeffrey D Ouellette, and Leila Guerriero (2021). "Retrieval of Biogeophysical Parameters From Bistatic Observations of Land at L-Band: A Theoretical Study". In: *IEEE Transactions on Geoscience and Remote Sensing* 60, pp. 1–17. DOI: 10.1109/TGRS.2021.3076051.

Pierdicca, Nazzareno, Ludovico De Titta, Luca Pulvirenti, and Giuliano Della Pietra (2009). "Bistatic radar configuration for soil moisture retrieval: analysis of the spatial coverage". In: *Sensors* 9.9, pp. 7250–7265. DOI: 10.3390/s90907250.

Pierdicca, Nazzareno, Luca Pulvirenti, Francesca Ticconi, and Marco Brogioni (2008). "Radar bistatic configurations for soil moisture retrieval: A simulation study". In: *IEEE Transactions on Geoscience and Remote Sensing* 46.10, pp. 3252–3264. DOI: 10.1109/TGRS.2008.921495.

Pipia, Luca, Jordi Muñoz-Marí, Eatidal Amin, Santiago Belda, Gustau Camps-Valls, and Jochem Verrelst (2019). "Fusing optical and SAR time series for LAI gap filling with multioutput Gaussian processes". In: *Remote Sensing of Environment* 235, p. 111452. DOI: 10.1016/j.rse.2019.111452.

Prévot, Laurent, Isabelle Champion, and G Guyot (1993). "Estimating surface soil moisture and leaf area index of a wheat canopy using a dual-frequency (C and X bands) scatterometer". In: *Remote Sensing of Environment* 46.3, pp. 331–339. DOI: 10.1016/0034-4257(93)90053-Z.

Probst, Philipp, Marvin N Wright, and Anne-Laure Boulesteix (2019). "Hyperparameters and tuning strategies for random forest". In: *Wiley Interdisciplinary Reviews: data mining and knowledge discovery* 9.3, e1301. DOI: 10.1002/widm.1301.

Qin, Jun, Kun Yang, Ning Lu, Yingying Chen, Long Zhao, and Menglei Han (2013). "Spatial upscaling of in-situ soil moisture measurements based on MODIS-derived apparent thermal inertia". In: *Remote Sensing of Environment* 138, pp. 1–9. DOI: 10.1016/j.rse.2013.07.003.

Quast, Raphael and Wolfgang Wagner (2016). "Analytical solution for first-order scattering in bistatic radiative transfer interaction problems of layered media". In: *Applied Optics* 55.20, pp. 5379–5386. DOI: 10.1364/AO.55.005379.

Quegan, Shaun, Thuy Le Toan, Jiong Jiong Yu, Florence Ribbes, and Nicolas Floury (2000). "Multitemporal ERS SAR analysis applied to forest mapping". In: *IEEE Transactions on Geoscience and Remote Sensing* 38.2, pp. 741–753. DOI: 10.1109/36.842003.

Rahimzadeh-Bajgiran, Parinaz, Aaron A Berg, Catherine Champagne, and Kenji Omasa (2013). "Estimation of soil moisture using optical/thermal infrared remote sensing in the Canadian Prairies". In: *ISPRS journal of photogrammetry and remote sensing* 83, pp. 94–103. DOI: 10.1016/j.isprsjprs.2013.06.004.

Rains, Dominik, Hans Lievens, Gabriëlle JM De Lannoy, Matthew F McCabe, Richard AM de Jeu, and Diego G Miralles (2021). "Sentinel-1 Backscatter Assimilation Using Support Vector Regression or the

Water Cloud Model at European Soil Moisture Sites". In: *IEEE Geoscience and Remote Sensing Letters* 19, pp. 1–5. DOI: 10.1109/LGRS.2021.3073484.

Rakotoarivony, L, O Taconet, D Vidal-Madjar, P Bellemain, and M Benallegue (1996). "Radar backscattering over agricultural bare soils". In: *Journal of Electromagnetic Waves and Applications* 10.2, pp. 187–209. DOI: 10.1163/156939396X00964.

Reisi-Gahrouei, Omid, Saeid Homayouni, Heather McNairn, Mehdi Hosseini, and Abdolreza Safari (2019). "Crop biomass estimation using multi regression analysis and neural networks from multitemporal L-band polarimetric synthetic aperture radar data". In: *International journal of remote sensing* 40.17, pp. 6822–6840. DOI: 10.1080/01431161.2019.1594436.

Schmugge, T (1976). "Remote sensing of soil moisture". In: *Symp. C., Cospar Meeting.* NASA-TM-X-71127.

Schneider, Maja, Tobias Schelte, Felix Schmitz, and Marco Körner (2023). "Eurocrops: The largest harmonized open crop dataset across the european union". In: *Scientific Data* 10.1, p. 612. DOI: 10.1038/s41597-023-02517-0.

Service public de Wallonie (2021). *Parcellaire agricole anonyme.* URL: https://geoportail.wallonie.be/catalogue/22063ae5-10f8-4e50-9abb-7557b154d8f2.html (visited on 03/13/2024).

Shang, Jiali, Jiangui Liu, Zhongxin Chen, Heather McNairn, and Andrew Davidson (2022). "Recent Advancement of Synthetic Aperture Radar (SAR) Systems and Their Applications to Crop Growth Monitoring". In: *Recent Remote Sensing Sensor Applications-Satellites and Unmanned Aerial Vehicles (UAVs).* IntechOpen. DOI: 10.5772/intechopen.102917.

Sharma, Avinash, Roger H Lang, Mehmet Kurum, Peggy E O'neill, and Michael H Cosh (2020). "L-band radar experiment and modeling of a corn canopy over a full growing season". In: *IEEE Transactions on Geoscience and Remote Sensing* 58.8, pp. 5821–5835. DOI: 10.1109/TGRS.2020.2971539.

SNAP – ESA Sentinel Application Platform v8.0.0 (2020). Version 8.0.0. URL: https://step.esa.int/main/download/snap-download/previous-versions/ (visited on 03/13/2024).

SNAP – ESA Sentinel Application Platform v9.0.0 (2022). Version 9.0.0. URL: https://step.esa.int/main/download/snap-download/ (visited on 03/13/2024).

Stamenkovic, Jelena, Leila Guerriero, Paolo Ferrazzoli, Claudia Notarnicola, Felix Greifeneder, and Jean-Philippe Thiran (2017). "Soil moisture estimation by SAR in alpine fields using gaussian process regressor trained by model simulations". In: *IEEE Transactions on Geoscience and Remote Sensing* 55.9, pp. 4899–4912. DOI: 10.1109/TGRS.2017.2687421.

Stamenković, Jelena, Paolo Ferrazzoli, Leila Guerriero, Devis Tuia, and Jean-Philippe Thiran (2015). "Joining a discrete radiative transfer model and a kernel retrieval algorithm for soil moisture estimation from SAR data". In: *IEEE Journal of Selected Topics in Applied Earth Observations and Remote Sensing* 8.7, pp. 3463–3475. DOI: 10.1109/JSTARS.2015.2432854.

Stubenrauch, Claudia J, William B Rossow, Stefan Kinne, S Ackerman, G Cesana, H Chepfer, L Di Girolamo, B Getzewich, A Guignard, A Heidinger, et al. (2013). "Assessment of global cloud datasets from satellites: Project and database initiated by the GEWEX radiation panel". In: *Bulletin of the American Meteorological Society* 94.7, pp. 1031–1049. DOI: 10.1175/BAMS-D-12-00117.1.

Technical Assistance for the Deployment of a L-Band SAR system to perform bistatic and interferometric SAR measurements during the ESA BelSAR Campaign (2020). DOI: 10.5270/ESA-bccf2d9.

Totir, Felix, Gabriel Vasile, Lionel Bombrun, Stefan Constantinescu, Angela Ionita, Florin Serban, and Dan Raducanu (2011). "Recent Polarimetric SAR Models for Danube Delta Monitoring using PALSAR Images". In: *5th International Workshop on Science and Applications of SAR Polarimetry and Polarimetric Interferometry (POLinSAR 2011)*, 8–pages.

Toure, Alassane, Keith PB Thomson, Geoffrey Edwards, Ron J Brown, and Brian G Brisco (1994). "Adaptation of the MIMICS backscattering model to the agricultural context-wheat and canola at L and C bands". In: *IEEE Transactions on Geoscience and Remote Sensing* 32.1, pp. 47–61. DOI: 10.1109/36.285188.

Tronquo, Emma, Hans Lievens, Jean Bouchat, Pierre Defourny, Nicolas Baghdadi, and Niko EC Verhoest (2022). "Soil Moisture Retrieval

Using Multistatic L-Band SAR and Effective Roughness Modeling". In: *Remote Sensing* 14.7, p. 1650. DOI: 10.3390/rs14071650.

Trudel, Melanie, François Charbonneau, and Robert Leconte (2012). "Using RADARSAT-2 polarimetric and ENVISAT-ASAR dual-polarization data for estimating soil moisture over agricultural fields". In: *Canadian Journal of Remote Sensing* 38.4, pp. 514–527. DOI: 10.5589/m12-043.

Ulaby, Fawwaz T, Percy P Batlivala, and Myron C Dobson (1978). "Microwave backscatter dependence on surface roughness, soil moisture, and soil texture: Part I-bare soil". In: *IEEE Transactions on Geoscience Electronics* 16.4, pp. 286–295. DOI: 10.1109/TGE.1978.294586.

Ulaby, Fawwaz T, Richard K Moore, and Adrian K Fung (1986). *Microwave remote sensing: Active and passive. Volume 3-From theory to applications.* Artech house.

Ulaby, Fawwaz Tayssir (1982). *Microwave remote sensing active and passive.* Artech house.

UN DESA (2022). *World Population Prospects 2022: Summary of Results.* Tech. rep. UN DESA/POP/2022/TR/NO. 3. United Nations Department of Economic and Social Affairs, Population Division (UN DESA).

Ustin, Susan L, Dar A Roberts, John A Gamon, Gregory P Asner, and Robert O Green (2004). "Using imaging spectroscopy to study ecosystem processes and properties". In: *BioScience* 54.6, pp. 523–534. DOI: 10.1641/0006-3568(2004)054[0523:UISTSE]2.0.CO;2.

Van doninck, Jasper, Jan Peters, Bernard De Baets, Eva M. De Clercq, Els Ducheyne, and Niko E.C. Verhoest (2011). "The potential of multitemporal Aqua and Terra MODIS apparent thermal inertia as a soil moisture indicator". In: *International Journal of Applied Earth Observation and Geoinformation* 13.6, pp. 934–941. DOI: 10.1016/j.jag.2011.07.003.

Vaswani, Ashish, Noam Shazeer, Niki Parmar, Jakob Uszkoreit, Llion Jones, Aidan N Gomez, Łukasz Kaiser, and Illia Polosukhin (2017). "Attention is all you need". In: *Advances in neural information processing systems* 30.

Veloso, Amanda, Stéphane Mermoz, Alexandre Bouvet, Thuy Le Toan, Milena Planells, Jean-François Dejoux, and Eric Ceschia (2017). "Understanding the temporal behavior of crops using Sentinel-1 and Sentinel-2-like data for agricultural applications". In: *Remote sensing of environment* 199, pp. 415–426. DOI: 10.1016/j.rse.2017.07.015.

Verhoest, Niko EC, Hans Lievens, Wolfgang Wagner, Jesús Álvarez-Mozos, M Susan Moran, and Francesco Mattia (2008). "On the soil roughness parameterization problem in soil moisture retrieval of bare surfaces from synthetic aperture radar". In: *Sensors* 8.7, pp. 4213–4248. DOI: 10.3390/s8074213.

Verrelst, Jochem, Zbyněk Malenovskỳ, Christiaan Van der Tol, Gustau Camps-Valls, Jean-Philippe Gastellu-Etchegorry, Philip Lewis, Peter North, and Jose Moreno (2019). "Quantifying vegetation biophysical variables from imaging spectroscopy data: A review on retrieval methods". In: *Surveys in Geophysics* 40, pp. 589–629. DOI: 10.1007/s10712-018-9478-y.

Verrelst, Jochem, Juan Pablo Rivera, Frank Veroustraete, Jordi Muñoz-Marí, Jan GPW Clevers, Gustau Camps-Valls, and José Moreno (2015). "Experimental Sentinel-2 LAI estimation using parametric, non-parametric and physical retrieval methods–A comparison". In: *ISPRS Journal of Photogrammetry and Remote Sensing* 108, pp. 260–272. DOI: 10.1016/j.isprsjprs.2015.04.013.

Verstraeten, Willem W, Frank Veroustraete, Corné J van der Sande, Ief Grootaers, and Jan Feyen (2006). "Soil moisture retrieval using thermal inertia, determined with visible and thermal spaceborne data, validated for European forests". In: *Remote Sensing of Environment* 101.3, pp. 299–314. DOI: 10.1016/j.rse.2005.12.016.

Vreugdenhil, Mariette, Wolfgang Wagner, Bernhard Bauer-Marschallinger, Isabella Pfeil, Irene Teubner, Christoph Rüdiger, and Peter Strauss (2018). "Sensitivity of Sentinel-1 backscatter to vegetation dynamics: An Austrian case study". In: *Remote Sensing* 10.9, p. 1396. DOI: 10.3390/rs10091396.

Waldner, François, Heidi Horan, Yang Chen, and Zvi Hochman (2019). "High temporal resolution of leaf area data improves empirical estimation of grain yield". In: *Scientific reports* 9.1, p. 15714. DOI: 10.1038/s41598-019-51715-7.

Wales, David J and Jonathan PK Doye (1997). "Global optimization by basin-hopping and the lowest energy structures of Lennard-Jones clusters containing up to 110 atoms". In: *The Journal of Physical Chemistry A* 101.28, pp. 5111–5116. DOI: 10.1021/jp970984n.

Wang, Kai, Steven E Franklin, Xulin Guo, Yuhong He, and Gregory J McDermid (2009). "Problems in remote sensing of landscapes and habitats". In: *Progress in Physical Geography* 33.6, pp. 747–768. DOI: 10.1177/0309133309350121.

Wang, Xiaolong (2024). "Contribution of fragmented croplands". In: *Nature Food*, pp. 1–2. DOI: 10.1038/s43016-024-00937-8.

Wang, Zhen, Tianjie Zhao, Jianxiu Qiu, Xuesheng Zhao, Rui Li, and Shu Wang (2021). "Microwave-based vegetation descriptors in the parameterization of water cloud model at L-band for soil moisture retrieval over croplands". In: *GIScience & Remote Sensing* 58.1, pp. 48–67. DOI: 10.1080/15481603.2020.1857123.

WEF (2020). *Nature risk rising: Why the crisis engulfing nature matters for business and the economy.*

Wegmüller, U, M Santoro, F Mattia, A Balenzano, G Satalino, P Marzahn, G Fischer, R Ludwig, and N Floury (2011). "Progress in the understanding of narrow directional microwave scattering of agricultural fields". In: *Remote Sensing of Environment* 115.10, pp. 2423–2433. DOI: 10.1016/j.rse.2011.04.026.

Weiss, Marie, Fred Baret, and Sylvain Jay (2020a). *S2ToolBox Level 2 products: LAI, FAPAR, FCOVER.* V2.0. URL: http://step.esa.int/docs/extra/ATBD_S2ToolBox_V2.0.pdf.

Weiss, Marie and Frédéric Baret (2017). *CAN_EYE V6.4.91 user manual.* URL: https://hal.inrae.fr/hal-02788819.

Weiss, Marie, Frédéric Jacob, and Grgory Duveiller (2020b). "Remote sensing for agricultural applications: A meta-review". In: *Remote sensing of environment* 236, p. 111402. DOI: 10.1016/j.rse.2019.111402.

Welch, Bernard L (1947). "The generalization of 'Students's' problem when several different population variances are involved". In: *Biometrika* 34.1-2, pp. 28–35. DOI: 10.1093/biomet/34.1-2.28.

Whitcraft, Alyssa K, Eric F Vermote, Inbal Becker-Reshef, and Christopher O Justice (2015). "Cloud cover throughout the agricultural growing season: Impacts on passive optical earth observations". In: *Remote Sensing of Environment* 156, pp. 438–447. DOI: 10.1016/j.rse.2014.10.009.

Willard, Jared, Xiaowei Jia, Shaoming Xu, Michael Steinbach, and Vipin Kumar (2022). "Integrating scientific knowledge with machine learning for engineering and environmental systems". In: *ACM Computing Surveys* 55.4, pp. 1–37. DOI: 10.1145/3514228.

Wiseman, Grant, Heather McNairn, Saeid Homayouni, and Jiali Shang (2014). "RADARSAT-2 polarimetric SAR response to crop biomass for agricultural production monitoring". In: *IEEE Journal of Selected Topics in Applied Earth Observations and Remote Sensing* 7.11, pp. 4461–4471. DOI: 10.1109/JSTARS.2014.2322311.

WMO, World Meteorological Organization, United Nations Environment Programme (UNEP), International Science Council (ISC), and Intergovernmental Oceanographic Commission of the United Nations Educational, Scientific and Cultural Organization (IOC-UNESCO) (2022). *The 2022 GCOS ECVs Requirements (GCOS 245)*. Geneva, Switzerland. 244 pp. URL: https://library.wmo.int/idurl/4/58111.

Wu, Tzong-Dar and Kun-Shan Chen (2004). "A reappraisal of the validity of the IEM model for backscattering from rough surfaces". In: *IEEE Transactions on Geoscience and Remote Sensing* 42.4, pp. 743–753. DOI: 10.1109/TGRS.2003.815405.

Yang, Guijun, Yuechan Shi, Chunjiang Zhao, and Jihua Wang (2012). "Estimation of soil moisture from multi-polarized SAR data over wheat coverage areas". In: *2012 First International Conference on Agro-Geoinformatics (Agro-Geoinformatics)*. IEEE, pp. 1–5. DOI: 10.1109/Agro-Geoinformatics.2012.6311656.

Yu, Lihong, Jiali Shang, Zhiqiang Cheng, Zebin Gao, Zixin Wang, Luo Tian, Dantong Wang, Tao Che, Rui Jin, Jiangui Liu, et al. (2020). "Assessment of Cornfield LAI Retrieved from Multi-Source Satellite Data Using Continuous Field LAI Measurements Based on a Wireless Sensor Network". In: *Remote Sensing* 12.20, p. 3304. DOI: 10.3390/rs12203304.

Zeng, Jiangyuan and Kun-Shan Chen (2018). "Theoretical study of global sensitivity analysis of L-band radar bistatic scattering for soil moisture retrieval". In: *IEEE Geoscience and Remote Sensing Letters* 15.11, pp. 1710–1714. DOI: 10.1109/LGRS.2018.2858269.

Zeng, Jiangyuan, Kun-Shan Chen, Haiyun Bi, Quan Chen, and Xiaofeng Yang (2016). "Radar response of off-specular bistatic scattering to soil moisture and surface roughness at L-band". In: *IEEE Geoscience and Remote Sensing Letters* 13.12, pp. 1945–1949. DOI: 10.1109/LGRS.2016.2618884.

Zhang, Yuan-Yuan and Zhen-Sen Wu (2016). "Bistatic scattering characteristics of wheat and soybean by radiative transfer model in L band and C band". In: *Progress In Electromagnetics Research B* 67, pp. 121–136. DOI: 10.2528/PIERB16011502.

Zheng, Guang and L Monika Moskal (2009). "Retrieving leaf area index (LAI) using remote sensing: theories, methods and sensors". In: *Sensors* 9.4, pp. 2719–2745. DOI: 10.3390/s90402719.

Zribi, M, O Taconet, V Ciarletti, and D Vidal-Madjar (2002). "Effect of row structures on radar microwave measurements over soil surface". In: *International Journal of Remote Sensing* 23.24, pp. 5211–5224. DOI: 10.1080/01431160110115762.

Zribi, Mehrez, Erwan Motte, Nicolas Baghdadi, Frédéric Baup, Sylvia Dayau, Pascal Fanise, Dominique Guyon, Mireille Huc, and Jean Pierre Wigneron (2018). "Potential applications of GNSS-R observations over agricultural areas: Results from the GLORI airborne campaign". In: *Remote Sensing* 10.8, p. 1245. DOI: 10.3390/rs10081245.

Zribi, Mehrez, Sekhar Muddu, Safa Bousbih, Ahmad Al Bitar, Sat Kumar Tomer, Nicolas Baghdadi, and Soumya Bandyopadhyay (2019). "Analysis of L-band SAR data for soil moisture estimations over agricultural areas in the tropics". In: *Remote Sensing* 11.9, p. 1122. DOI: 10.3390/rs11091122.

Supporting publications

Journal articles

- **Jean Bouchat**, Quentin Deffense, Thomas De Maet, and Pierre Defourny (in prep.). "Joint use of optical and SAR imagery for near real-time green area index retrieval in maize"

- **Jean Bouchat**, Emma Tronquo, Anne Orban, Karlus A C de Macedo, Malcolm Davidson, Niko EC Verhoest, and Pierre Defourny (2024c). "The BELSAR dataset: Mono-and bistatic full-pol L-band SAR for agriculture and hydrology". In: *Scientific Data* 11.1, p. 513. DOI: `10.1038/s41597-024-03320-1`

- **Jean Bouchat**, Emma Tronquo, Anne Orban, Xavier Neyt, Niko EC Verhoest, and Pierre Defourny (2022a). "Green Area Index and Soil Moisture Retrieval in Maize Fields Using Multi-Polarized C-and L-Band SAR Data and the Water Cloud Model". In: *Remote Sensing* 14.10, p. 2496. DOI: `10.3390/rs14102496`

- **Jean Bouchat**, Emma Tronquo, Anne Orban, Niko EC Verhoest, and Pierre Defourny (2022b). "Assessing the Potential of Fully Polarimetric Mono-and Bistatic SAR Acquisitions in L-band for Crop and Soil Monitoring". In: *IEEE Journal of Selected Topics in Applied Earth Observations and Remote Sensing* 15, pp. 3168–3178. DOI: `10.1109/JSTARS.2022.3162911`

- Emma Tronquo, Hans Lievens, **Jean Bouchat**, Pierre Defourny, Nicolas Baghdadi, and Niko EC Verhoest (2022). "Soil Moisture Retrieval Using Multistatic L-Band SAR and Effective Roughness Modeling". In: *Remote Sensing* 14.7, p. 1650. DOI: `10.3390/rs14071650`

Conference proceedings

- Lorenzo G Papale, Fabio Del Frate, Leila Guerriero, Giovanni Schiavon, and **Jean Bouchat** (2023). "Physics-Based ML and Polarimetric SAR for Soil Moisture Retrieval”. In: *IGARSS 2023-2023 IEEE International Geoscience and Remote Sensing Symposium*. IEEE, pp. 1930–1933. DOI: 10.1109/IGARSS52108.2023.10283164

- **Jean Bouchat**, Emma Tronquo, Hans Lievens, Niko Verhoest, and Pierre Defourny (2021). “Assessing the Potential of Fully-Polarimetric Simultaneous Mono-and Bistatic Airborne SAR Acquisitions in L-Band for Applications in Agriculture and Hydrology”. In: *2021 IEEE International Geoscience and Remote Sensing Symposium IGARSS*. IEEE, pp. 2703–2706. DOI: 10.1109/IGARSS47720.2021.9554673

- **Jean Bouchat** and Pierre Defourny (2021). “Effect of Row Orientation on Maize Green Area Index Retrieval from L-Band Synthetic Aperture Radar Imagery”. In: *2021 IEEE International Geoscience and Remote Sensing Symposium IGARSS*. IEEE, pp. 6716–6719. DOI: 10.1109/IGARSS47720.2021.9554513

Posters

- **Jean Bouchat**, Quentin Deffense, Qiaomei Su, Jinlong Fan, and Pierre Defourny (2024b). “Using a transformer encoder for SAR-to-optical GAI regression with Sentinel-1 and -2 data”. In: *2024 Dragon 5 Symposium*. June 24-28, 2024. Lisbon, Portugal

- Sébastien Saelens, **Jean Bouchat**, Qiaomei Su, Jinlong Fan, and Pierre Defourny (2024). “Monitoring the plant water content in senescent maize using multifrequency SAR data in Shanxi province, China”. In: *2024 Dragon 5 Symposium*. June 24-28, 2024. Lisbon, Portugal

- **Jean Bouchat**, Quentin Deffense, and Pierre Defourny (2024a). “AI-based SAR-to-optical GAI regression for crop monitoring”. In: *EO for Agriculture under Pressure 2024 Workshop*. May 13-16, 2024. Frascati, Italy

- **Jean Bouchat**, Quentin Deffense, Yuejiao Liao, Ying Song, Sébastien Saelens, Qiaomei Su, Jinlong Fan, and Pierre Defourny (2023). “Leaf area index retrieval in Shanxi province of China using Sentinel-1 data”. In: *2023 Dragon 5 Symposium*. Sep. 11-15, 2023. Hohhot, Inner Mongolia, P.R. China

- Thibault Castin, **Jean Bouchat**, and Pierre Defourny (2022). "Monitoring of maize dry matter content using Sentinel-1 time series for harvest decision". In: *2022 Living Planet Symposium.* May 23-27, 2022. Bonn, Germany

- **Jean Bouchat**, Emma Tronquo, EC Niko Verhoest, and Pierre Defourny (2022c). "A Machine Learning Approach for Maize Green Area Index Retrieval from Multi-Polarization C-and L-band Synthetic Aperture Radar Data". In: *2022 Living Planet Symposium.* May 23-27, 2022. Bonn, Germany